Skin-Friction and Forced Convection from Rough and Smooth Plates

Citation: Thermo 3 (4): 711-775 (2023)

As Published: http://dx.doi.org/10.3390/thermo3040040

Publisher: Multidisciplinary Digital Publishing Institute

Persistent URL: https://hdl.handle.net/1721.1/153252

Version: Final published version: final published article, as it appeared in a journal, conference proceedings, or other formally published context

thermo

MDPI

Article

Skin-Friction and Forced Convection from Rough and Smooth Plates

Aubrey Jaffer

Independent Researcher, Waltham, MA 02452, USA; agj@alum.mit.edu

Abstract: Since the 1930s, theories of skin-friction drag from plates with rough surfaces have been based by analogy to turbulent flow in pipes with rough interiors. Failure of this analogy at small fluid velocities has frustrated attempts to create a comprehensive theory. Utilizing the concept of a self-similar roughness that disrupts the boundary layer at all scales, this investigation derives formulas for a rough or smooth plate's skin-friction coefficient and forced convection heat transfer given its characteristic length, root-mean-squared (RMS) height-of-roughness, isotropic spatial period, Reynolds number, and the fluid's Prandtl number. This novel theory was tested with 456 heat transfer and friction measurements in 32 data-sets from one book, six peer-reviewed studies, and the present apparatus. Compared with the present theory, the RMS relative error (RMSRE) values of the 32 data-sets span 0.75% through 8.2%, with only four data-sets exceeding 6%. Prior work formulas have smaller RMSRE on only four of the data-sets.

Keywords: skin-friction; forced-convection; height-of-roughness

Citation: Jaffer, A. Skin-Friction and Forced Convection from Rough and Smooth Plates. *Thermo* **2023**, *3*, 711–775. https://doi.org/10.3390/thermo3040040

Academic Editor: Johan Jacquemin

Received: 5 September 2023
Revised: 28 November 2023
Accepted: 3 December 2023
Published: 16 December 2023

1. Introduction

Fluid flowing along a wall (plate) experiences "skin-friction drag" (or "resistance") opposing its flow. Related to skin-friction, "forced convection heat transfer" is the heat transfer to or from a surface induced by fluid flow along that surface. Skin-friction and forced convection are fundamental processes with applications from engineering to geophysics.

This investigation seeks to develop formulas to predict the skin-friction coefficient and forced convection heat transfer from rough and smooth plates.

1.1. Pipe-Plate Analogy

Circa 1930, Prandtl [1] and von Kármán [2] developed theories for resistance along (smooth) plates from the results of research on flow through pipes; this is the "pipe-plate analogy".

In 1934, Prandtl and Schlichting [3] developed a theory of skin-friction resistance for rough plates based on their analysis of Nikuradse's [4] measurements of sand glued inside pipes ("sand-roughness"). The conclusion of the (translated) paper states:

> "The resistance law just derived for rough plates has chiefly validity for a very specific type of roughness, namely a smooth surface to which sand grains have been densely attached and where the Nikuradse pipe results have been taken as the basis…
>
> A single roughness parameter (the relative roughness) will in all likelihood no longer answer the purpose in continued investigations of the roughness problem".

In 1936, Schlichting [5] investigated the velocity profiles and resistance of water flowing through a closed rectangular channel having one wall replaced in turn by a series of plates, each having an array of identical protrusions attached: spheres, spherical caps (bumps), or cones. The protrusions were positioned on the plates in a hexagonal array that was elongated 15% in the direction of flow.

With a significant pressure drop between inflow and outflow of the channel, it was not an instance of the isobaric (uniform pressure) flow that can occur along external plates. The similarity of channel and pipe flows is well known, but neither supports nor refutes treating rough pipe interiors and plates analogously.

In 1954, Hama [6] described three challenges of the pipe-plate analogy:

> "Now there is no obvious reason why pipe flow and boundary-layer flow should be identical or even similar. First, a pressure gradient is essential for flow through a pipe but not along a plate. Second, pipe flow is confined and perforce uniform, while flow along a plate develops semi-freely and bears no such a priori guarantee of displaying similar velocity profiles at successive sections. Finally, the diameter and roughness size are the only geometrical dimensions of established flow in pipes, whereas at least three linear quantities are necessary to characterize the boundary-layer".

1.2. Boundary Layer

Schlichting [7] describes the boundary layer: "In that thin layer the velocity of the fluid increases from zero at the wall (no slip) to its full value which corresponds to external frictionless flow".

Hama attempted to confirm the rough pipe-plate analogy with measurements of wire screens affixed to smooth plates, but concluded that it was confirmed only in the fully rough regime (defined below).

1.3. Sand-Roughness

Prior works [3–11] specify sand-roughness k_S, the height of "coarse and tightly placed roughness elements such as, for example, coarse sand grains glued on the surface" (Schlichting [7]).

Testing a machined analogue of sand-roughness circa 1975, Pimenta, Moffat, and Kays [8] stated that, while agreement with the Prandtl–Schlichting model was "rather good" in the fully rough regime, the apparatus's behavior differed from "Nikuradse's sand-grain pipe flows in the transition region".

Modeling the wake component of the velocity profile, in 1985 Mills and Hang [9] presented a formula improving the match with data from Pimenta et al. in the rough regime; however, it did not address other flow regimes.

1.4. Flow Regimes

Along with laminar flow, the theory for flow within pipes (and channels) distinguishes three turbulent flow regimes: smooth, (fully) rough, and transitional. Smooth-regime pipe flow encounters viscous resistance varying inversely with the fluid velocity per viscosity ratio. Rough pipe flow encounters resistance varying with the height-of-roughness, while being largely insensitive to viscosity. The transitional regime describes the range of fluid velocities where both viscosity and roughness affect the resistance (Colebrook [12]).

1.5. Reynolds Number

The Reynolds number (Re) represents the bulk fluid velocity (far from the plate); Re with a subscript represents other fluid velocities. The local Reynolds number $Re_x = x\,Re/L$, where x is the distance from the leading edge of the plate in the direction of flow, and characteristic length L is the length scale for the physical system. Local measurements are made at distance x from the leading edge. Unless stated otherwise, L is the plate length in the direction of flow.

1.6. Skin-Friction Coefficient

Skin-friction in prior works is represented by the (dimensionless) local drag coefficient c_f or C_f, a function of the relative sand-roughness x/k_S and Re or a subscripted Re.

Prandtl and Schlichting [3] specified the boundaries between flow regimes using the "sand-roughness Reynolds number" Re_k. For plates, it assigned the boundaries between smooth, transitional, and rough regimes at $Re_k = 7.08$ and 70.8. Pimenta et al. [8] gave $Re_k = 65$ as the transitional-to-rough boundary.

Figure 1a presents local skin-friction coefficient curves, Re_k regime boundaries, and measurements from the Pimenta et al. [8] plate having $k_S = 0.794\,\text{mm}$ at $x = 0.965\,\text{m}$. Figure 1b presents the (whole-plate) average skin-friction coefficients with $L = 2.18$ m.

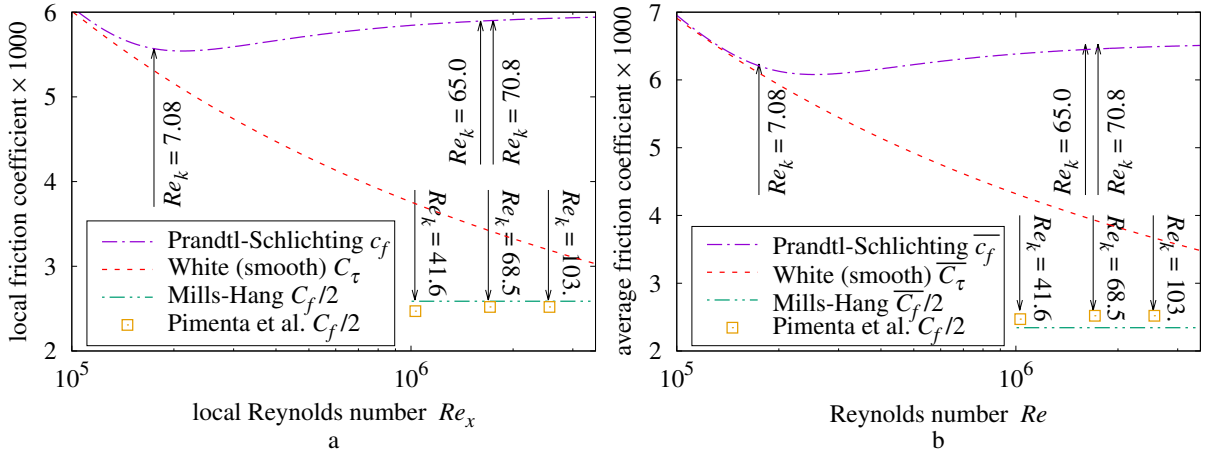

Figure 1. (**a**) Local c_f versus Re_x [8], (**b**) Average $\overline{c_f}$ versus Re.

1.7. Plate Flow versus Pipe Flow

Schlichting [7] states: "The resistance to flow offered by rough walls [of pipes] is larger than that . . . for smooth pipes".

The rough pipe-plate analogy holds that this rule also applies to rough, external plates. For example, the "Prandtl-Schlichting c_f" curve is never less than the "White (smooth) C_τ" curve in Figure 1a.

The Pimenta et al. measurements are much closer to $c_f/2$ than they are to c_f. (The Bergstrom, Akinlade, and Tachie [13] local friction coefficient (C_f) measurements of woven wire meshes and perforated sheets (present work Section 14) are also much closer to $c_f/2$ than c_f.) Pimenta et al. [8] and Mills and Hang [9] both designated $c_f/2$ as the friction coefficient. All three measurements in Figure 1 are less than the smooth regime coefficient C_τ. If rough friction is never less than smooth friction, then these measurements must not be in any turbulent flow regime; the remaining alternative is laminar flow. Laminar flow coefficients have a steeper slope than C_τ; yet these measurements are near the constant level predicted by Mills–Hang $C_f/2$ for the rough regime.

- The pipe-plate analogy fails for roughness because rough skin-friction coefficients can be less than the smooth regime coefficients for external plates, but not inside pipes.

1.8. More Recent Work

With the rough pipe-plate analogy's failure obscured by the factor of 2, research based on the pipe-plate analogy continued. The 2004 survey article Jiménez [14] did not question the rough pipe-plate analogy, writing: "The theoretical arguments are sound, but the experimental evidence is inconclusive".

Circa 2005, Bergstrom, Akinlade, and Tachie [13], performed experiments with sandpapers, woven wire meshes, and perforated sheets attached onto a flat plate, reporting that: $\sqrt{C_f} = [0.360 \pm 0.025]\,\delta^*/\delta$, where δ^* is the displacement thickness and δ is the 99% velocity boundary layer thickness. As a function of a roughness metric, this formula has no predictive value because both δ^* and δ must be inferred from velocity measurements along the surface under test. Fortunately, Bergstrom et al. included free-stream velocity in their tables, allowing comparisons of their skin-friction data with the present theory.

The 2021 survey article Chung, Hutchins, Schultz, and Flack [15] summarizes studies for predicting the drag, (boundary layer) velocity profiles, or convection from rough walls or pipes in terms of turbulence theory. Several roughness metrics were introduced, however none convert to the "isotropic spatial period" introduced in Section 8 of the present work.

The studies cited by [15] generally rely on turbulence theory, sand-roughness, Prandtl and Schlichting [3], and the pipe-plate analogy. The present theory relies on none of these.

- Sand-roughness's lack of generality and the failure of the pipe-plate analogy for roughness motivate a fresh theoretical analysis of isobaric flow along a rough plate, an analysis derived from traceable roughness metrics.
- Prior works analyze turbulence in the boundary layer. The central premise of this investigation is that plate roughness disrupts its boundary layer. The present theory does not utilize turbulence theory.
- The present theory is about plates; it has no implications for smooth or rough pipe flow.

1.9. Approach

Flow along flat, smooth plates can be laminar or turbulent with a continuous boundary layer. This investigation uses the term "rough flow" for disrupted boundary layer flow from a rough plate.

Figure 1a,b shows that the skin-friction from smooth and rough plates are substantially different. Roughness disrupts what would otherwise be a viscous sub-layer adjacent to the plate. Lienhard and Lienhard [16] teaches: "Even a small wall roughness can disrupt this thin sublayer, causing a large decrease in the thermal resistance (but also a large increase in the wall shear stress)".

With a sufficiently large roughness, the nascent boundary layers forming after each disruption will be smaller than the roughness. The momentum can thus transfer directly between the fluid flow and the plate's roughness. In order for these transfers to constitute most of the skin-friction, there must be no significant pressure gradients acting on the plate. Thus, this approach works only with a thin plate parallel to an isobaric fluid flow. It is not applicable to pipes, for example, because the pressure decreases as fluid flows through a cylindrical pipe.

Shearing stress can be determined from the free-stream velocity, ignoring turbulent velocity perturbations. Thus, the skin-friction can be derived without turbulence theory.

- While understanding the nature of the flow shed by roughness is of theoretical interest, it is not needed for determining the skin-friction coefficient from a very rough surface in an isobaric flow.

1.10. Not Empirical

Empirical theories derive their coefficients from measurements, inheriting the uncertainties from those measurements. Theories developed from first principles derive their coefficients mathematically. For example, Incropera, DeWitt, Bergman, and Lavine [17] gives the thermal conductance of one face of a diameter D disk into a stationary, uniform medium having thermal conductivity k ($\mathrm{W}/(\mathrm{m}\cdot\mathrm{K})$) as $8\,k/[\pi\,D]$ $\mathrm{W}/(\mathrm{m}^2\cdot\mathrm{K})$. The present theory derives from first principles; it is not empirical. Each formula is tied to aspects of the plate geometry, fluid, and flow.

1.11. Mathematics

Familiarity with calculus is assumed. Computational geometry, probability, self-similar recurrences, the Lambert W function, vector-space norms, and Fourier transforms are also employed; each is briefly introduced or illustrated graphically. Differential equations are not explicitly used.

1.12. Overview

After a comparison of roughness metrics in Section 3, a thought experiment about flow along self-similar roughness is solved using computational geometry in Section 5. The resulting skin-friction coefficient formula's range of validity does not extend to 0 height-of-roughness. However, analyzing the case of a roughness which induces skin-friction midway between that of a self-similar rough surface and that of a smooth surface in Section 6 produces a formula with unprecedented accuracy for smooth plates.

The self-similar roughness was designed to produce the most boundary layer disruption possible within a given RMS height-of-roughness. A self-similar roughness could be fabricated, but measuring its skin-friction could confirm predictions only for self-similar roughness. Instead, Sections 7 and 8 turn to isotropic, periodic roughness, which applies in many practical use cases. Fourier analysis and computational geometry result in a quantitative test for periodic isotropy which computes the isotropic period L_P from a sufficiently large height map of roughness. Section 8 computationally tests arrays of posts and wells to find the upper/lower area ratio spans which qualify as isotropic, periodic roughness.

Section 9 presents formulas for converting between local and average friction coefficients, and tests them on measurements from Pimenta et al. [8], Churchill [11], and Žukauskas and Šlančiauskas [18].

Section 10 derives formulas for forced convection heat transfer from rough and smooth plates.

Periodicity enables the derivation of formulas for the onset of rough flow from an isotropic, periodic rough surface in Section 11.

Section 12 finds that the skin-friction coefficient of isotropic, periodic roughness is the same as for self-similar roughness, except when the periodic roughness peaks are all co-planar (at the same elevation) plateaus. Plateau roughness is an isotropic, periodic roughness with most of its area at its peak elevation. Section 12 derives a quantitative test for plateau roughness from a height map of roughness. It also develops formulas for the Re_x thresholds separating rough flow and turbulent flow along the plate. These thresholds are tested in Sections 14 and 15.

Section 13 derives formulas for skin-friction coefficients and convection heat transfer from a plateau roughness shedding rough and turbulent flow from regions of the plate separated at the Re_x thresholds developed in Section 12.

Section 14 tests the present theory on measurements from Bergstrom et al. [13].

Section 15 tests the present theory on measurements from the present apparatus.

Section 16 analyzes fluid flow along isotropic, periodic roughness at Re smaller than the rough flow thresholds found in Section 11. This flow strongly resembles the "oscillations [...] discovered in the laminar boundary layer along a flat plate" by Schubauer and Skramstad [19]. The present work treats them identically. Although measurements of flows over such small roughnesses are lacking, smooth plate skin-friction measurements from Gebers [20,21] and uniform-wall-temperature convection measurements by Žukauskas and Šlančiauskas [18] support the present theory.

2. Data-Sets and Evaluation

Tables 1 and 2 list the data-sets to be compared with the present theory.

Rough surface convection measurements were obtained from an apparatus built for this investigation, which measured (whole-plate) average convection heat transfer in air at $2300 < Re < 93{,}000$. Appendix A describes this apparatus and its measurement methodology. Section 15 presents its measurements.

The Gebers [20,21] skin-friction measurements were captured from a graph in Schlichting [7] by measuring the distance from each point to the graph's axes, then scaling to the graph's units using the "Engauge" software (version 12.1). The remaining measurement data-sets were manually entered from tables in the cited works. Several obvious single-digit typographical errors were corrected.

Two non-obvious single digit errors in the text of a prior work are detailed in Section 14.

Table 1. Sources of friction measurements.

Source	Measuring	Pr_∞	$Re \geq$	$Re \leq$	$\pm$	Count
[11,22,23] Churchill [1]	turbulent average, air	0.71	1.0×10^5	1.0×10^9		9
[11,22,23] Churchill [1]	turbulent local, air	0.71	1.0×10^5	1.0×10^{10}		11
[18] Žukauskas and Šlančiauskas	turbulent local, oil	55.2	3.6×10^5	1.1×10^7		5
[18] Žukauskas and Šlančiauskas	turbulent local, water	5.42	3.6×10^5	2.4×10^6		8
[18] Žukauskas and Šlančiauskas	turbulent local, water	2.78	7.2×10^5	4.4×10^6		8
[18] Žukauskas and Šlančiauskas	turbulent local, air	0.71	7.6×10^5	3.2×10^6		9
[20,21] Gebers	transition average		7.4×10^5	3.3×10^7		33
[8] Pimenta et al.	packed sphere rough local, air	0.71	3.8×10^5	5.8×10^6	10%	19
[13] Bergstrom et al.	turbulent local, air	0.71	1.6×10^6	4.6×10^6	5%	4
[13] Bergstrom et al.	wire mesh rough local, air	0.71	1.6×10^6	4.7×10^6	9%	12
[13] Bergstrom et al.	perforated sheet local, air	0.71	1.6×10^6	4.6×10^6	9%	12

[1] Churchill [11] extracted its measurements from Smith and Walker [22] and Spalding and Chi [23].

Table 2. Sources of convection measurements.

Source	Measuring	Pr_∞	$Re \geq$	$Re \leq$	$\pm$	Count
[24] Kestin et al.	UWT [1] transition local, air	0.7	3.8×10^4	3.5×10^5		13
[24] Kestin et al.	UWT transition local, air	0.7	4.3×10^4	2.9×10^5		7
[25] Reynolds et al.	UWT transition local, air	0.71	8.2×10^4	1.1×10^6	4%	22
[18] Žukauskas and Šlančiauskas	UHF [1] transition local, air	0.71	1.1×10^4	8.2×10^5	5%	10
[18] Žukauskas and Šlančiauskas	UHF transition local, air	0.71	1.1×10^4	8.2×10^5	5%	10
[18] Žukauskas and Šlančiauskas	UHF transition local, air	0.71	1.1×10^4	8.2×10^5	5%	10
[18] Žukauskas and Šlančiauskas	UHF transition local, water	6.57	4.0×10^3	2.2×10^5	10%	19
[18] Žukauskas and Šlančiauskas	UHF transition local, water	6.57	5.0×10^3	2.2×10^5	10%	15
[18] Žukauskas and Šlančiauskas	UHF transition local, oil	108	3.0×10^4	3.0×10^5	5%	17
[18] Žukauskas and Šlančiauskas	UHF transition local, oil	257	1.2×10^4	1.1×10^5	5%	17
[18] Žukauskas and Šlančiauskas	UWT average, air	0.71	1.1×10^5	6.3×10^5	5%	16
[18] Žukauskas and Šlančiauskas	UWT average, air	0.71	1.7×10^5	7.5×10^5	5%	19
[18] Žukauskas and Šlančiauskas	UWT average, water	5.8–7.1	1.4×10^6	2.3×10^6	10%	5
[18] Žukauskas and Šlančiauskas	UWT average, water	2.9–7.2	2.1×10^5	6.4×10^6	10%	21
[18] Žukauskas and Šlančiauskas	UWT average, water	2.0–5.8	1.8×10^5	1.4×10^6	10%	40
[18] Žukauskas and Šlančiauskas	UWT average, oil	75–246	5.0×10^4	7.0×10^5	5%	40
[18] Žukauskas and Šlančiauskas	UWT average, oil	80–205	1.1×10^5	3.6×10^5	5%	11
[18] Žukauskas and Šlančiauskas	UWT average, oil	92–317	2.7×10^4	7.5×10^5	5%	29
present apparatus $\varepsilon = 3.00$ mm	UWT rough average, air	0.71	2.3×10^3	9.3×10^4	3-7%	13
present apparatus $\varepsilon = 1.04$ mm	UWT plateau average, air	0.71	2.0×10^3	6.8×10^4	2-6%	14

[1] UHF is uniform heat flux; UWT is uniform wall temperature.

The transcribed data-sets are available from Supplementary Materials.

RMS Relative Error

The "$\pm$" column of Tables 1 and 2 lists the estimated measurement uncertainties stated by the cited studies. While essential to empirical theories, these estimates are only indicative for non-empirical theories.

Root-mean-squared relative error (RMSRE) provides an objective, quantitative evaluation. It gauges the fit of measurements $g(Re_j)$ to function $f(Re_j)$, giving each of the n samples equal weight in Formula (1).

$$\text{RMSRE} = \sqrt{\frac{1}{n}\sum_{j=1}^{n}\left|\frac{g(Re_j)}{f(Re_j)} - 1\right|^2} \tag{1}$$

$$\text{bias} = \frac{1}{n}\sum_{j=1}^{n}\left\{\frac{g(Re_j)}{f(Re_j)} - 1\right\} \qquad \text{scatter} = \sqrt{\frac{1}{n}\sum_{j=1}^{n}\left|\frac{g(Re_j)}{f(Re_j)} - 1 - \text{bias}\right|^2} \tag{2}$$

Along with presenting RMSRE, charts in the present work split RMSRE into the bias and scatter components defined in Formula (2). The root-sum-squared (RSS) of bias and scatter is RMSRE.

3. Roughness Metrics

Two established, traceable roughness metrics are the root-mean-squared (RMS) height-of-roughness and the arithmetic-mean height-of-roughness. For an elevation function $z(x, y)$ defined on area A having a convex perimeter, its mean elevation $\bar{z}$ and RMS height-of-roughness ε are:

$$\bar{z} = \int_A z\,\mathrm{d}A \Big/ \int_A \mathrm{d}A \tag{3}$$

$$\varepsilon = \sqrt{\int_A |z - \bar{z}|^2\,\mathrm{d}A \Big/ \int_A \mathrm{d}A} \tag{4}$$

The arithmetic-mean height-of-roughness is defined in terms of the same mean elevation $\bar{z}$ Formula (3):

$$\int_A |z - \bar{z}|\,\mathrm{d}A \Big/ \int_A \mathrm{d}A \tag{5}$$

3.1. Sand-Roughness

Modeling sand-roughness grains as diameter k_S spheres sitting in a pool of depth g glue, the mean elevation $\bar{z}$ of a cell of area A containing one sphere is:

$$\bar{z} = g + \frac{5\,\pi\,k_S^3}{24\,A} - \frac{\pi\,k_S^2\,g}{4\,A} \tag{6}$$

With the cell's RMS height-of-roughness ε computed from Formula (4), Figure 2 shows k_S/ε versus the ratio of cell area to the sphere's shadow area, at six glue-levels between 0% and 50% of k_S. Table 3 lists k_S, grain densities, and k_S/ε conversion factors for Nikuradse's [4] sand coatings, assuming $g = 0.5\,k_S$.

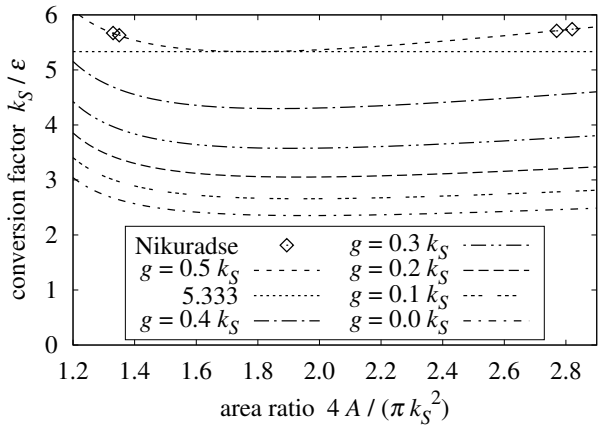

Figure 2. k_S/ε versus cell area of sand-roughness [4].

Table 3. Nikuradse's sand coatings at $g = 0.5\,k_S$.

k_S	Grains /cm^2	k_S/ε
0.08 cm	150	5.67
0.04 cm	590	5.63
0.02 cm	1130	5.74
0.01 cm	4600	5.71

3.2. Conversions

Afzal, Seena, and Bushra [26] fitted 5.333 as the RMS to sand-roughness conversion factor k_S/ε, and 6.45 as the arithmetic-mean to sand-roughness conversion factor (both in pipes). $k_S/\varepsilon = 5.333$ is a broad minimum of the $g = 0.5\,k_S$ curve in Figure 2.

The "k_S/ε" column values in Table 3 ("Nikuradse" in Figure 2) match each other within 2%. The tightest spread on Table 3 data with the arithmetic-mean height-of-roughness exceeds 20%. Thus, sand-roughness correlates an order of magnitude more strongly with RMS than arithmetic-mean height-of-roughness.

Flack, Schultz, Barros, and Kim [27] measured skin-friction from grit-blasted surfaces in a duct, writing "The root-mean-square roughness height is shown to be most strongly correlated with the equivalent sand-roughness height (k_S) for the grit-blasted surfaces".

- Arithmetic-mean height-of-roughness will not be considered further by this investigation.

3.3. Packed Spheres Roughness

The Pimenta et al. [8] plate was composed of 11 layers of closely packed 1.27 mm diameter metal spheres "arranged such that the surface has a regular array of hemispherical roughness elements". Joined by brazing, there was no pool of glue surrounding the spheres. Shrinking the cell to the sphere's shadow, $\pi\,k_S^2/4$, the RMS height-of-roughness of the top half of the 1.27 mm sphere is 0.150 mm. Pimenta et al. gave $k_S = 0.794$ mm; $k_S/5.333 \approx 0.149$ mm, which matches 0.150 mm within 1%.

- This investigation will use $k_S/\varepsilon = 5.333$ as the RMS to sand-roughness conversion factor.

4. Formulas From Prior Works

Several prior works gave formulas for skin-friction coefficient in the fully rough regime.

4.1. Prandtl and Schlichting

In boundary layer theory [7], Prandtl and Schlichting gave formulas for fully rough local (c_f) and plate average ($\overline{c_f}$) skin-friction coefficient for a rough plate as a function of x/k_S and L/k_S, respectively:

$$c_f = \left[2.87 + 1.58\,\log_{10}\frac{x}{k_S}\right]^{-2.5} \qquad x \le L \tag{7}$$

$$\overline{c_f} = \left[1.89 + 1.62\,\log_{10}\frac{L}{k_S}\right]^{-2.5} \qquad 10^2 < \frac{L}{k_S} < 10^6 \tag{8}$$

4.2. Mills and Hang

Mills and Hang [9] gave a Formula (9) which is more accurate than Formula (7) on the local skin-friction measurements from Pimenta et al. [8]. Their local (C_f) and average ($\overline{C_f}$) coefficient formulas were:

$$C_f = \left[3.476 + 0.707 \ln \frac{x}{k_S}\right]^{-2.46} \qquad 750 < \frac{x}{k_S} < 2750 \tag{9}$$

$$\overline{C_f} = \left[2.635 + 0.618 \ln \frac{L}{k_S}\right]^{-2.57} \tag{10}$$

4.3. White

White [10] gave Formula (11) for fully rough local skin-friction coefficient:

$$C_f = \left[1.4 + 3.7 \log_{10} \frac{x}{k_S}\right]^{-2} \qquad \frac{x}{k_S} > \frac{Re_x}{1000} \tag{11}$$

White is also the source of widely used formulas for turbulent skin-friction coefficients of a smooth plate:

$$C_\tau(Re_x) = \frac{0.455}{\ln^2(0.06\, Re_x)} \qquad \overline{C_\tau}(Re_x) = \frac{0.523}{\ln^2(0.06\, Re_x)} \tag{12}$$

4.4. Average Coefficient

Mills and Hang [9] derived the average Formula (10) from the local Formula (9) by fitting a curve to the result of a numerical integration such as Formula (13):

$$\overline{C_f}\left(\frac{L}{k_S}\right) = \frac{k_S}{L - L_0} \int_{L_0/k_S}^{L/k_S} C_f(x)\, \mathrm{d}x \tag{13}$$

The local Formulas (7), (9), and (11) each have a singularity where the expression containing the logarithm is 0. The lower limit of integration (L_0/k_S) must be large enough to avoid this; but the lower limit is not revealed in the prior works. The averaging Formula (13) is quite sensitive to the lower limit because the largest value of the local formula occurs there.

For the Mills–Hang Formula (9), with lower bound $L_0/k_S = 1.6$ and initial $\mathrm{d}x/k_S = 0.01$, integration of the local C_f is within ±0.5% of the average $\overline{C_f}$ in Formula (10) over the range $200 < x/k_S < 2 \times 10^5$.

For the Prandtl–Schlichting Formula (7), with lower bound $L_0/k_S = 0.5$ and initial $\mathrm{d}x/k_S = 0.5$, integration of the local c_f is within ±0.5% of the average $\overline{c_f}$ in Formula (8) over the range $200 < x/k_S < 2 \times 10^5$.

4.5. Churchill

Churchill [11] compared eight formulas from diverse sources versus the data from Pimenta et al. [8], finding none significantly closer to the measurements than the Mills–Hang local Formula (9).

Section 9 compares the local fully rough regime formulas with measurements from Pimenta et al. [8].

5. Flow over Obstacles

Jiménez [14] wrote "In flows with $\delta/k < 50$, the effect of the roughness extends across the boundary layer, and is also variable. There is little left of the original wall-flow dynamics in these flows, which can perhaps be better described as flows over obstacles".

This investigation focuses first on a case where flow over obstacles dominates the dynamics. It models the shearing stress of flow along a roughness which disrupts that

flow at a succession of scales: L, $L/2$, $L/2^2$, $L/2^3$, ... While simpler surfaces may produce rough flow, a roughness which disrupts at all these scales surely will.

- This approach departs from prior works because their continuous boundary layer assumption is incompatible with a roughness which repeatedly disrupts boundary layers.

5.1. Profile Roughness

Simpler than surface roughness, profile roughness is nonetheless informative.

Let a "profile roughness" be a function $z(x)$ with $0 \leq x \leq L$; its mean elevation $\overline{z}$ and RMS height-of-roughness ϵ are computed similarly to surface roughness ε:

$$\overline{z} = \frac{1}{L} \int_0^L z(x)\,\mathrm{d}x \tag{14}$$

$$\epsilon = \sqrt{\frac{1}{L} \int_0^L |z(x) - \overline{z}|^2\,\mathrm{d}x} \tag{15}$$

5.2. Self-Similar Profile Roughness

Let a "self-similar profile roughness" be a profile roughness function $z(x)$ such that the RMS height-of-roughness of $z(x)$ over an open interval is twice the RMS height-of-roughness of $z(x)$ over each half of that interval (leaving out the midpoint).

These x intervals are open (not containing the endpoints); the $z(x)$ value for each endpoint contributes to the height-of-roughness of its parent interval, but not to any sub-interval. This definition is designed so that $z(x)$ will have the following property:

- The RMS height-of-roughness of $z(x)$ over an open interval, divided by the length of that interval will be invariant through its succession of scales.

5.3. Ramp Permutation

An additional constraint is needed to reduce the uncountable variety of possible $z(x)$ functions to a manageable number. Experience with self-similar curves suggests a restriction to profile roughnesses, which are permutations of the linear ramp $z(x) = \varsigma\, x/L$ with $0 \leq x \leq L$. Each elevation from 0 to peak height ς occurs exactly once.

The only occurrence of x in Formulas (14) and (15) is $z(x)$; hence, the RMS height-of-roughness calculation depends only on the z values, not on their relation to x. Thus, the height-of-roughness of any ramp-permutation is identical to the height-of-roughness of the linear ramp:

$$\epsilon = \sqrt{\frac{1}{L} \int_0^L \left| \frac{\varsigma\, x}{L} - \frac{\varsigma}{2} \right|^2 \mathrm{d}x} = \frac{\varsigma}{\sqrt{12}} \tag{16}$$

5.4. Self-Similar Ramp Permutation

A self-similar integer sequence $Y(t, w)$ from integers $0 \leq t < w = 2^q$ allows self-similar behavior to be explored with a finite approximation. Letting $t = \lfloor w\, x/L \rfloor \equiv \mathrm{floor}(w\, x/L)$ constructs a profile roughness from a sequence by $z(x) = \varsigma\, Y(\lfloor w\, x/L \rfloor, w)/w$.

The following three examples are self-similar ramp-permutation sequences. Each element of the sequence is generated by calling its recurrence function with a sequence index $0 \leq t \leq w$ and w, an integer power of 2. Each recursive call divides w by 2, terminating (and returning) when w reaches 1.

Self-similar recurrence (17) defines the integer Gray-code sequence $G(t, w)$ shown in Figure 3a.

$$G(t, w) = \begin{cases} t & w = 1 \\ w + G(w - 1 - (t \bmod w), w/2) & \lfloor t/w \rfloor = 1 \\ G(t \bmod w, w/2) & \text{otherwise} \end{cases} \tag{17}$$

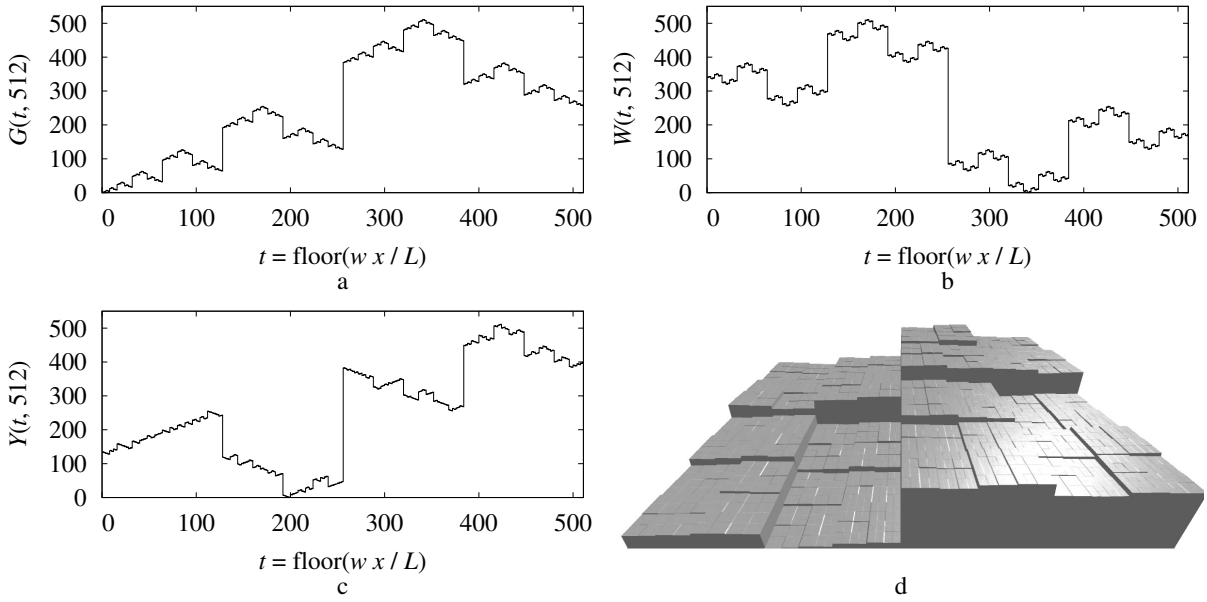

Figure 3. (**a**) Gray -code profile roughness; (**b**) wiggliest self-similar roughness; (**c**) random reversal profile roughness; (**d**) random reversal ramp surface.

Recurrence (18) defines the integer sequence $W(t, w)$ shown in Figure 3b; it reverses direction at each bifurcation, yielding a wiggliest-possible self-similar ramp-permutation sequence.

$$W(t,w) = \begin{cases} t & w = 1 \\ \lfloor t/w \rfloor w + W(w - 1 - (t \bmod w), w/2) & \text{otherwise} \end{cases} \tag{18}$$

Figure 3c shows a sequence generated by randomly reversing or not at each bifurcation in recurrence (19). Figure 3d shows a random reversal, self-similar, ramp-permutation surface roughness.

$$Y(t,w) = \begin{cases} t & w = 1 \\ w + Y(w - 1 - (t \bmod w), w/2) & \text{with 50\% probability} \\ Y(t \bmod w, w/2) & \text{otherwise} \end{cases} \tag{19}$$

5.5. Cardinality

The goal is to characterize self-similar roughnesses in general. The theory should work for the vast majority of self-similar roughness functions, with few outliers. For a given number of points $w = 2^q \geq 8$, there are $2^{w-1} \geq 128$ distinct self-similar ramp-permutation sequences, of which there are only two distinct ramps and two distinct wiggliest sequences.

5.6. Friction Travel and Velocity

When the fluid flow encounters roughness, some particles of fluid must move in directions not parallel to the bulk flow. Such movement results from deflections of flow by roughness peaks, pits, ridges, and valleys; the extent of deflections should grow with the RMS height-of-roughness.

Let "run" be the horizontal axis and "friction" be the vertical axis of a profile roughness such as in Figure 3c. For an integer ramp-permutation sequence $Y(t, w)$, the sum of the

(dimensionless) lengths of all its run segments is simply $w - 1 = 2^q - 1$. The sum of its friction segment lengths is:

$$\sum_{t=0}^{2^q-2} \left| Y(t, 2^q) - Y(t+1, 2^q) \right| \tag{20}$$

If a particle of fluid traces the ramp-permutation sequence $Y(t, w)$ between $t = 0$ and $t = w - 1$, then $w - 1$ is the run travel, while Formula (20) is the friction travel.

Figure 4 shows the friction per run travel ratio versus $q = \log_2(w)$. The linear ramp trace has slope 0; the Gray-code trace has slope 1/2; the random reversal cases have slope of approximately 1/2; and the wiggliest roughness trace has slope 2/3.

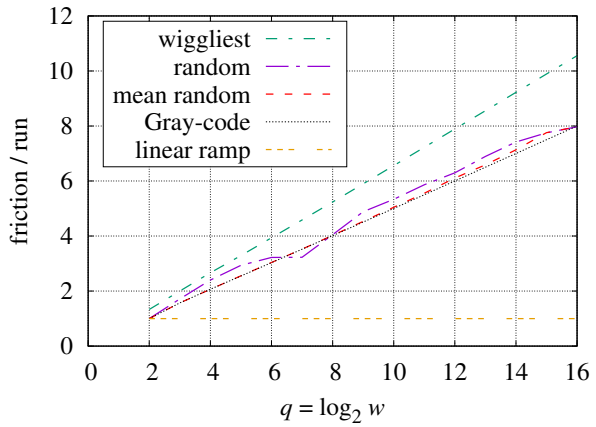

Figure 4. Travel along profile roughness.

5.7. Roughness Sequence Outliers

A wiggliest roughness sequence $W(t, w)$ is an extreme case; it reverses friction direction at each increment of run (t). For each wiggliest roughness sequence with $w \geq 8$ there are $2^{w-1} - 2$ other random reversal roughness sequences. In contrast, the linear ramp never reverses direction. For each linear ramp sequence there are $2^{w-1} - 2$ other random reversal sequences.

- Being outliers, $W(t, w)$ and linear ramps are excluded from further consideration as roughness.

5.8. Dimensional Analysis

Excluding the outliers, Figure 4's friction per run ratios are about:

$$\frac{q}{2} \equiv \frac{\log_2 w}{2} \tag{21}$$

$Y(t, w)$, t, and w are dimensionless. The friction per run ratio (21) needs to be reformulated in terms of ϵ and L, which have length units. Turning to dimensional analysis, the argument to $\log_2$ must be dimensionless, involve ϵ, and be greater than 1, so that the logarithm will be positive. This friction per run ratio must increase with increasing ϵ. Thus, ϵ and the logarithm will be in denominators, yielding:

$$\frac{2}{\log_2(L/\epsilon)} \tag{22}$$

Scaling Formula (22) by $1/\sqrt{12}$ from Formula (16) converts it into the RMS friction per run travel ratio:

$$\frac{1}{\sqrt{12}} \frac{2}{\log_2(L/\epsilon)} = \frac{1}{\sqrt{3}\,\log_2(L/\epsilon)} \tag{23}$$

- Considering the run travel and friction travel with respect to time lets Formula (23) also serve as the friction velocity per bulk fluid velocity ratio: u_ρ / u.

5.9. Isotropy

Fluid particles stay within the vertical plane of profile roughness. Surface roughness deflects particles in all directions. Therefore, this investigation will use ε instead of ϵ and restrict its attention to "isotropic" roughness, where rotating the flow azimuth (direction) in the plane of the rough surface does not substantially affect its behavior. Section 8 develops a decision procedure for roughness isotropy.

The friction-to-run-length ratio should not be tied only to ramp-permutations based on successive halving. Instead, use the expected value of a continuous random variable $Z > 1$ having a Pareto distribution whose probability density function is $1/Z^2$:

$$\int_1^{L/\varepsilon} \frac{Z}{Z^2}\,\mathrm{d}Z = \ln(L/\varepsilon) \qquad \frac{u_\rho}{u} = \frac{1}{\sqrt{3}\,\ln(L/\varepsilon)} \tag{24}$$

5.10. Shearing Stress

The skin-friction coefficient $\overline{f_c}$ is the ratio of the shearing stress τ_2 per the fluid flow's dynamic pressure (kinetic energy density) $\rho\, u^2/2$, where ρ is the fluid's density:

$$\overline{f_c} = \frac{\tau_2}{\rho\, u^2/2} \tag{25}$$

Both $\tau_2 = \rho\, {u_\rho}^2/2$ and $\rho\, u^2/2$ have units of pressure, $\mathrm{kg}/(\mathrm{m}\cdot\mathrm{s}^2)$. From Formula (24):

$$u_\rho = \frac{u}{\sqrt{3}\,\ln(L/\varepsilon)} \qquad \tau_2 = \frac{\rho\, {u_\rho}^2}{2} = \frac{\rho\, u^2}{6\,\ln^2(L/\varepsilon)} \tag{26}$$

- Eliminating τ_2 from Formulas (25) and (26) yields the average skin-friction coefficient of an isotropic, self-similar roughness:

$$\overline{f_\rho} = \frac{1}{3\,\ln^2(L/\varepsilon)} \qquad \frac{L}{\varepsilon} \gg 1 \qquad \varepsilon > 0 \tag{27}$$

Figure 5 plots $\overline{f_\rho}$ Formula (27). Sections 9 and 14 compare Formula (27) with friction measurements from rough surfaces.

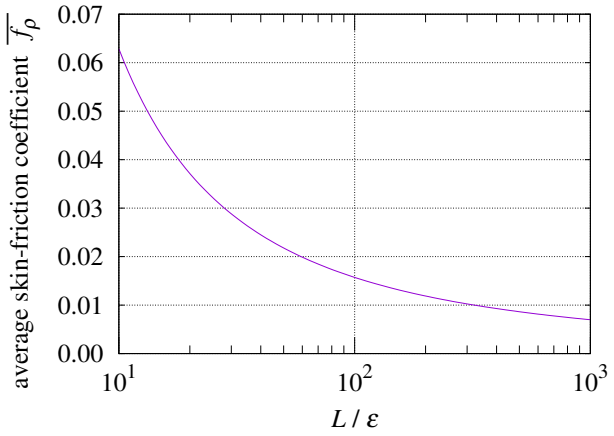

Figure 5. Average $\overline{f_\rho}$ versus L/ε of rough plate.

Note that Prandtl and Schlichting [3] calculated $\tau = \rho\, {u_\rho}^2$, not $\tau_2 = \rho\, {u_\rho}^2/2$. As a result, $\overline{c_f} \geq 2\,\overline{f_\rho}$ and $c_f \geq 2\, f_\rho$. Pimenta et al. [8] and Mills and Hang [9] designated $c_f/2$ as the friction coefficient.

6. Turbulent Friction

Formula (27) is not defined for $\varepsilon = 0$, a smooth plate.

Given $Re \gg 1$ there must be an L/ε ratio so large that a length L plate with a self-similar roughness of RMS height ε induces skin-friction midway between that of a rough surface and that of a smooth surface.

6.1. Roughness Reynolds Number

Let the "roughness Reynolds number" Re_ε derive from friction velocity u_ρ at scale ε:

$$Re_\varepsilon = \frac{u_\rho\,\varepsilon}{\nu} = \frac{Re}{\sqrt{3}\,[L/\varepsilon]\,\ln(L/\varepsilon)} \tag{28}$$

where ν is the fluid's kinematic viscosity (with units m^2/s) and $Re = L\,u/\nu$. The Re strength at which rough plate friction transitions to smooth plate friction should have the same Re_ε value at all $L/\varepsilon \gg 1$. $Re_\varepsilon = 1$ when $\varepsilon = u_\rho/\nu$. Combining $Re_\varepsilon = 1$ with Formula (28) relates Re and L/ε at transition:

$$Re = \sqrt{3}\,\frac{L}{\varepsilon}\,\ln\frac{L}{\varepsilon} \tag{29}$$

This link between Re and L/ε suggests that the turbulent friction coefficient $\overline{f_\tau}$ can be inferred by combining Formulas (27) and (29). However, there being no roughness on a smooth plate, the coefficients must be different from $\overline{f_\rho}$ Formula (27). Scaling $\overline{f_\rho}(L/\varepsilon)$ by $\sqrt[3]{2}$, and its argument by $1/\mathrm{e}$:

$$\overline{f_\tau} = \sqrt[3]{2}\,\overline{f_\rho}\left(\frac{L}{\mathrm{e}\,\varepsilon}\right) = \sqrt[3]{2}\left[\frac{1}{3}\,\ln^{-2}\frac{L}{\mathrm{e}\,\varepsilon}\right] \qquad \frac{\sqrt[3]{2}}{3} \approx 0.4200 \tag{30}$$

Euler's number $\mathrm{e} = \exp(1)$ is a fixed point of $\varphi\,\ln\varphi$,which appears in Formula (32). The etiology of $\sqrt[3]{2}$ is unclear, but the present work's tiny $+0.13\%$ bias in Section 6.3 makes mere coincidence unlikely.

6.2. Lambert W *Function*

The (natural) logarithm function ln is the inverse of $\exp(x)$. Similarly, the Lambert W function is the inverse of $x\,\exp(x)$. L/ε can be eliminated from Formulas (29) and (30) using the Lambert W function's principal branch W_0, which is defined by equivalence (31) and plotted in Figure 6.

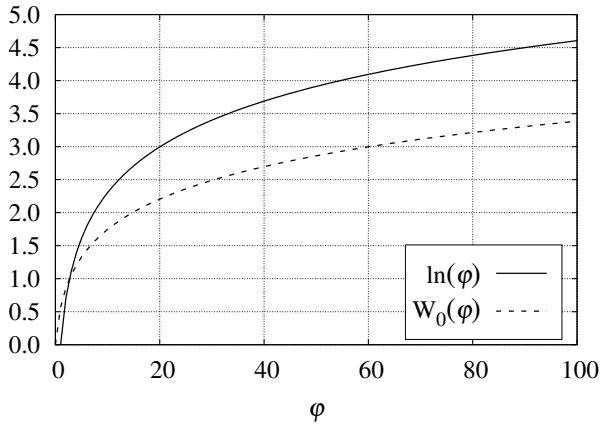

Figure 6. Lambert function W_0.

$$\vartheta = \varphi \exp \varphi \quad \Leftrightarrow \quad \varphi = \mathrm{W}_0(\vartheta) \tag{31}$$

$$\vartheta = \varphi \ln \varphi \quad \Leftrightarrow \quad \varphi = \exp \mathrm{W}_0(\vartheta) \tag{32}$$

The related equivalence (32) acting on Formula (29) lets $\exp(\mathrm{W}_0(Re/\sqrt{3}))$ replace L/ε in Formula (30) when $Re \gg \sqrt{3}\,\mathrm{e} \approx 4.71$.

$$\overline{f_\tau} = \frac{\sqrt[3]{2}}{3} \ln^{-2}\left(\frac{\exp\left(\mathrm{W}_0\left(Re/\sqrt{3}\right)\right)}{\mathrm{e}}\right) = \frac{\sqrt[3]{2}/3}{\left[\mathrm{W}_0\left(Re/\sqrt{3}\right) - 1\right]^2} \tag{33}$$

6.3. Comparison with Measurements

Churchill [11] compared turbulent friction formulas from multiple studies with measurements from Smith and Walker [22], and Spalding and Chi [23]. Figure 7 plots them and $\overline{f_\tau}$ Formula (33); the key gives the RMS error of the measurements relative to each formula (RMSRE was introduced in Section 2).

- With 0.75% RMSRE, $\overline{f_\tau}$ Formula (33) has less error than any formula evaluated by Churchill.

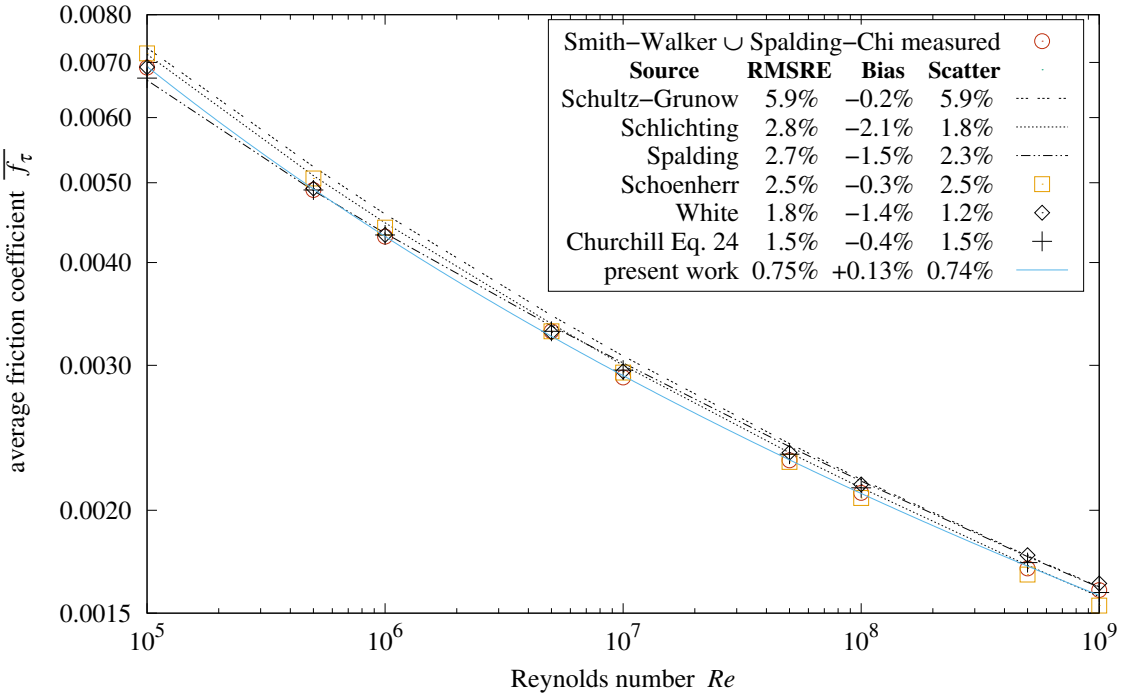

Figure 7. Average $\overline{f_\tau}$ versus Re of smooth plate, [11].

7. Spectral Roughness

- Self-similar roughness served to establish the skin-friction coefficient upper bound for roughness $\varepsilon > 0$, and the coefficient for $\varepsilon = 0$. Attention now turns to existing conventional types of roughness.

Several prior works [4–6,9,12] use the term "uniform roughness" to describe sand-roughness, implying that its height-of-roughness is the same at all scales. This concept of uniform roughness is incompatible with self-similarity; the RMS height-of-roughness of a portion of a self-similar surface must shrink with its succession of scales.

Sand-roughness can be described as "repeated roughness". However, a roughness composed of parallel rows of 1000 sand grains spanning its length can also be described as

having 500 sand grain pairs spanning its length. An unambiguous method for determining the spatial period is needed.

7.1. Discrete Fourier Transform

The discrete Fourier transform (34) converts a series of equally spaced samples of a function into a complex-number coefficient X_j for each of its harmonic sinusoidal components:

$$X_j = \sum_{t=0}^{w-1} Y(t,w)\ \exp\left(\frac{-2\,\pi\,\mathrm{i}\,j\,t}{w}\right) \tag{34}$$

A complex number consists of two real numbers as $a + b\,\mathrm{i}$, where $\mathrm{i} = \sqrt{-1}$; b is called the imaginary part. The amplitude of $a + b\,\mathrm{i}$, written $|a + b\,\mathrm{i}| = \sqrt{a^2 + b^2}$.

There is a profound connection between X_j and the RMS height-of-roughness ϵ:

$$\epsilon = \sqrt{\frac{1}{w}\sum_{j=1}^{w-1} |X_j|^2} \tag{35}$$

$|X_{w-j}| = |X_j|$ because all the $Y(t,w)$ elevations have imaginary parts $= 0$; hence there are $w/2 + 1$ distinct $|X_j|$; only $0 \le j \le w/2$ needs to be considered in the developments which follow.

7.2. Dominant Component of Roughness

The $X_0 = \bar{z}$ term, the mean value of Y, is the only X_j term not included in the Formula (35) sum for ϵ. Hence, the dominant component of roughness will be the X_j ($0 < j \le w/2$) having the largest amplitude.

- Let the "period index" j_P be the nonzero index j of the X_j having the largest amplitude $|X_j|$.
- When one $|X_j|$ is dominant, j_P is well-defined and the profile roughness's spatial period is $L_P = L/j_P$.

Figure 8a shows the $|X_j|/w$ amplitude spectrum of the Gray-code profile roughness from Figure 3a, as well as the mean Fourier spectrum amplitudes from 187 instances of 128-point random reversal profiles ($w = 128$). For both spectra, X_1 has the largest amplitude; thus $j_P = 1$, indicating that neither spectrum is from repeated roughness.

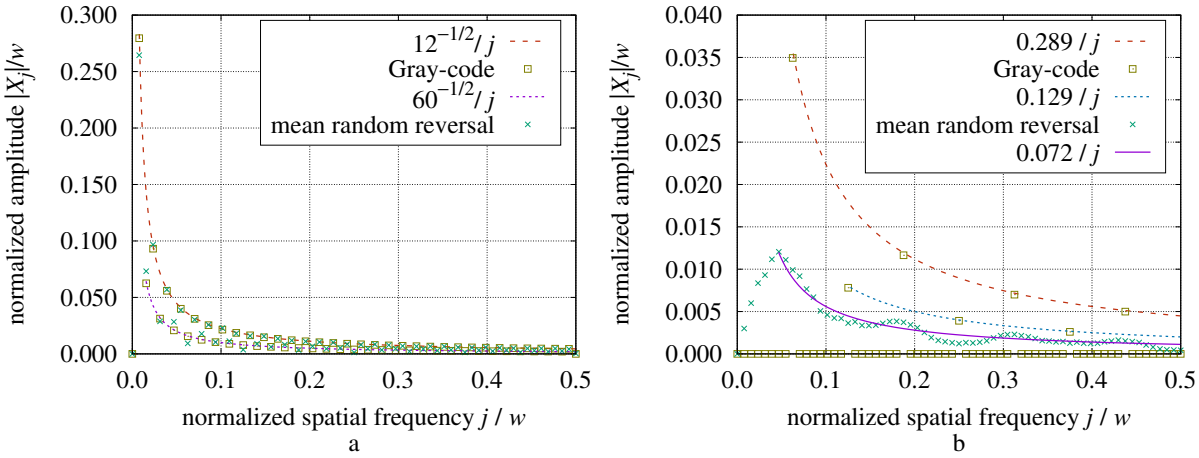

Figure 8. (**a**) Gray and random spectra; (**b**) Gray and random eighths.

Figure 8b shows the spectrum of eight concatenated repetitions of a Gray-code sequence, as well as the mean Fourier spectrum amplitudes from 187 instances of eight concatenated random reversal sequences. The period index j_P of the Gray-code eighths

is 8, as expected; but the random reversal sequences have $j_P = 6$ because their amplitudes are not correlated between the random eighths.

- This use of the discrete Fourier transform was able to determine the spatial period of profile roughness. Section 8 generalizes this spatial period metric to isotropic surface roughness.

8. Periodic Roughness

- Let a "periodic roughness" be a flat surface tiled with many isotropic, uniformly sized patches, all sharing the same mean elevation $\bar{z}$ and RMS height-of-roughness ε.
- The mean elevation and RMS height-of-roughness of the entire surface will therefore be $\bar{z}$ and ε.

8.1. Discrete Spatial Fourier Transform

Let $S_{s,t}$ be a $w \times w$ matrix of mean elevations from a $w \times w$ square grid of an $L_w \times L_w$ region of a rough surface. Its two-dimensional discrete spatial Fourier transform is:

$$X_{j,k} = \sum_{t=0}^{w-1} \sum_{s=0}^{w-1} S_{s,t} \exp\left(-2\,\pi\,\mathrm{i}\,\frac{j\,t + k\,s}{w}\right) \tag{36}$$

- Let the two-dimensional period index $j_P = \sqrt{j^2 + k^2} > 0$, where $0 \le j \le w/2$ and $0 \le k \le w/2$ are the indexes of the coefficient $X_{j,k}$ having the largest amplitude, excluding $X_{0,0}$.
- The two-dimensional spatial period $L_P = L_w / j_P$.

Figure 9a shows the j_P values of a square equal-area bi-level surface (regular array of square posts on a flat plate) computing $X_{j,k}$ from a 64×64 interpolated sampling of that surface with azimuth from 0° through 45°, and which is scaled between 9 and 13 cells per side. At each scale, j_P varies within a ± 1 range as the azimuth is rotated. Figure 9b shows j_P values of a 25% high, 75% low, bi-level surface; some of its j_P traces have peaks outside of the ± 1 range. This suggests a quantitative criterion for surface roughness isotropy:

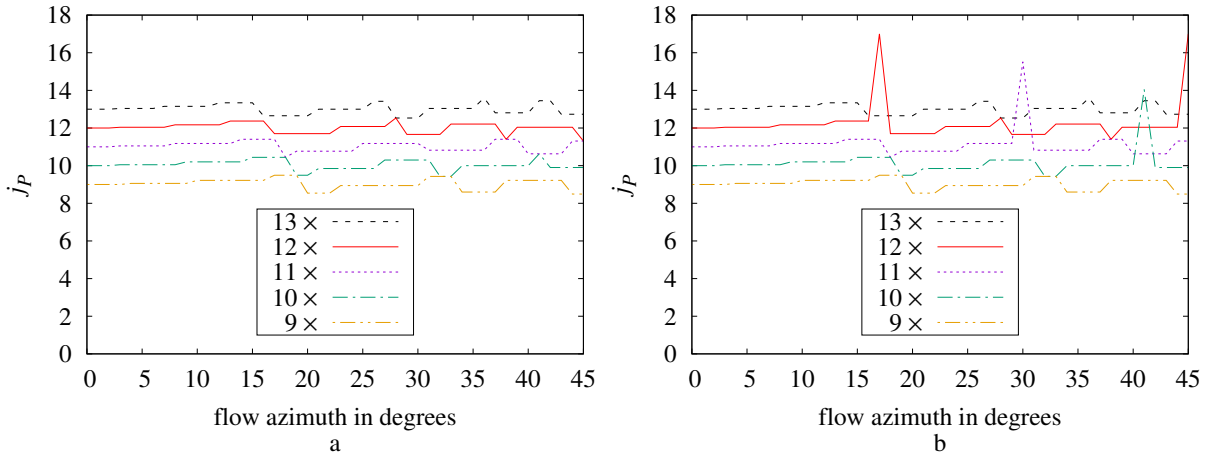

Figure 9. (**a**) Bi-level plate 50%; (**b**) Bi-level plate 25%.

- A surface roughness is isotropic if $j_P \gg 1$ varies no more than ± 2 through its full flow azimuth rotation.
- More specifically, using $w \times w$ ($w \ge 64$) samplings of roughness at nine scales over a 2:1 range such that most of the calculated j_P values satisfy $8 \le j_P \le 16$ at each scale, we carry out 56 sampling trials with randomized offset and randomized azimuth rotation per scale. A roughness is considered isotropic if no more than 5 of the $504 (= 56 \times 9)$ trials have j_P varying more than $\pm w/32$ from its scale.

8.2. Exploring Isotropy

Tests of this criterion applied to 128×128 interpolated samplings found the following roughnesses to be isotropic:

- Square arrays of aligned square posts having an upper area fraction between 27% and 76%;
- Square arrays of circular columns having an upper area fraction between 24% and 78%;
- Hexagonal arrays of circular columns having an upper area fraction between 6% and 75%;
- Hexagonal arrays of circular wells (depressions) having an upper area fraction between 25% and 94%;
- Hexagonal arrays of aligned square posts having an upper area fraction between 4% and 49%;
- Hexagonal arrays of aligned square wells having an upper area fraction between 51% and 96%;
- 15% elongated hexagonal arrays of cone or bump protrusions described in Schlichting [5].

8.3. Visual Isotropy

This isotropy test is not equivalent to the visual appearance of isotropy. Square post arrays having upper area fractions of 20% fail the isotropy test, while those with 30% pass. Plates from Schlichting [5] having elongated hexagonal arrays of cones are not visually isotropic, yet pass the test.

9. Local Skin-Friction Coefficients

Conversions between local and average skin-friction are needed in order to compare prior work with the present work.

9.1. Continuous Local to Average Skin-Friction

The ratio of average to local skin-friction $\overline{f_c}/f_c > 1$ of a continuous boundary layer is calculated from f_c by Formula (37). Using $Re_0 > 0$ as the integration lower-bound avoids the division-by-zero singularity at the leading edge of the plate.

$$\frac{\overline{f_c}(Re)}{f_c(Re)} = \frac{1}{Re - Re_0} \int_{Re_0}^{Re} \frac{f_c(Re_x)}{f_c(Re)} \, \mathrm{d}Re_x \tag{37}$$

The Blasius laminar model in Schlichting [7] derives the local drag coefficient:

$$f_\lambda = \frac{0.664}{\sqrt{Re_x}} \tag{38}$$

Applying transform (37) to Formula (38) and factoring the denominator produces a novel formula for the average laminar friction coefficient that lacks the leading-edge singularity:

$$\overline{f_\lambda}(Re) = 1.328 \, \frac{\sqrt{Re} - \sqrt{Re_0}}{Re - Re_0} = \frac{1.328}{\sqrt{Re} + \sqrt{Re_0}} \tag{39}$$

Lienhard and Lienhard [16] estimates $Re_0 = 600$, leading to $\overline{f_\lambda}(0) \approx 0.0542$.

9.2. Disrupted Local to Average Skin-Friction

The local skin-friction coefficient is not well-defined for self-similar roughness because of its constant L/ε. Periodic roughness has varying L/ε; conveniently, it also provides L_P/ε as the lower-bound of integration.

A crucial distinction between periodic roughness and smooth surfaces is that periodic roughness disrupts the boundary layer repeatedly. Thus, the local skin-friction coefficients

being averaged are independent. Instead of $\overline{f_\rho}/f_\rho$ scaling linearly, it should scale as the square:

$$\frac{\overline{f_\rho}(L/\varepsilon)}{f_\rho(L/\varepsilon)} = \left[\frac{\varepsilon}{L - L_P}\int_{L_P/\varepsilon}^{L/\varepsilon}\frac{f_\rho(r)}{f_\rho(L/\varepsilon)}\,\mathrm{d}r\right]^2 \tag{40}$$

Applying Formula (40) to the Mills–Hang local Formula (9) yields the average skin-friction coefficient:

$$\overline{C_f}^{\,2}\Big/C_f \tag{41}$$

where C_f and $\overline{C_f}$ are from Equations (9) and (10), respectively.

9.3. Average Formulas from Prior Work

Figure 10 compares fully rough regime average skin-friction formulas with $\overline{f_\rho}$ Formula (27). To the right of each "$\in \pm$" is the maximum discrepancy from $\overline{f_\rho}$ over the Mills–Hang range $750 < L/k_S < 2750$, which is $4000 < L/\varepsilon < 14{,}666$. The Mills–Hang range boundaries are marked by red arrows in Figure 10.

Note that Section 12 establishes that $\overline{f_\rho}$ Formula (27) applies to sand-roughness.

- "$0.5\,\overline{C_f}^{\,2}/C_f \in \pm$ 2.4%" is 1/2 of Formula (41), the disrupted boundary layer averaging Formula (40) applied to the Mills–Hang local Formula (9); it matches $\overline{f_\rho}$ within ±2.4%.
- "$0.5\,\overline{c_f} \in \pm$ 9.3%" is 1/2 of the Prandtl–Schlichting average Formula (8).
- "$0.5\,\overline{C_f} \in \pm$23.1%" is 1/2 of the Mills–Hang average Formula (10).

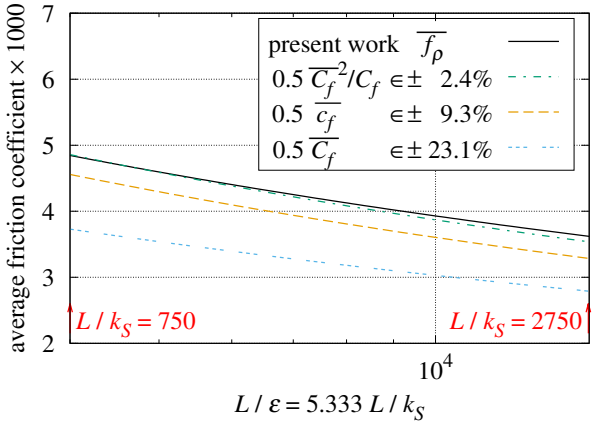

Figure 10. Average friction coefficient of sand-roughness.

9.4. Disrupted Average to Local Skin-Friction

For disrupted boundary layers, the transform for local friction f_ρ given average friction $\overline{f_\rho}$ is:

$$\frac{f_\rho(L/\varepsilon)}{\overline{f_\rho}(L/\varepsilon)} = \left[\frac{\mathrm{d}\Big([L - L_P]\,\overline{f_\rho}(L/\varepsilon)\Big)}{\mathrm{d}L}\Big/\overline{f_\rho}(L/\varepsilon)\right]^2 \tag{42}$$

Applying Formula (42) to $\overline{f_\rho}$ Formula (27) with $L \geq x > L_P \geq \varepsilon$ yields the local friction coefficient:

$$f_\rho(x/\varepsilon) = \frac{1}{3}\left[\frac{\ln(x/\varepsilon) + 2\,[L_P/x - 1]}{\ln^2(x/\varepsilon)}\right]^2 \tag{43}$$

9.5. Local Formulas From Prior Work

Figure 11a plots the local friction coefficients from White (11), Prandtl–Schlichting (7), Mills–Hang (9), and the present work's f_ρ Formula (43).

- Mills–Hang matches f_ρ Formula (43) within 3.1% over $750 < x/k_S < 2750$.

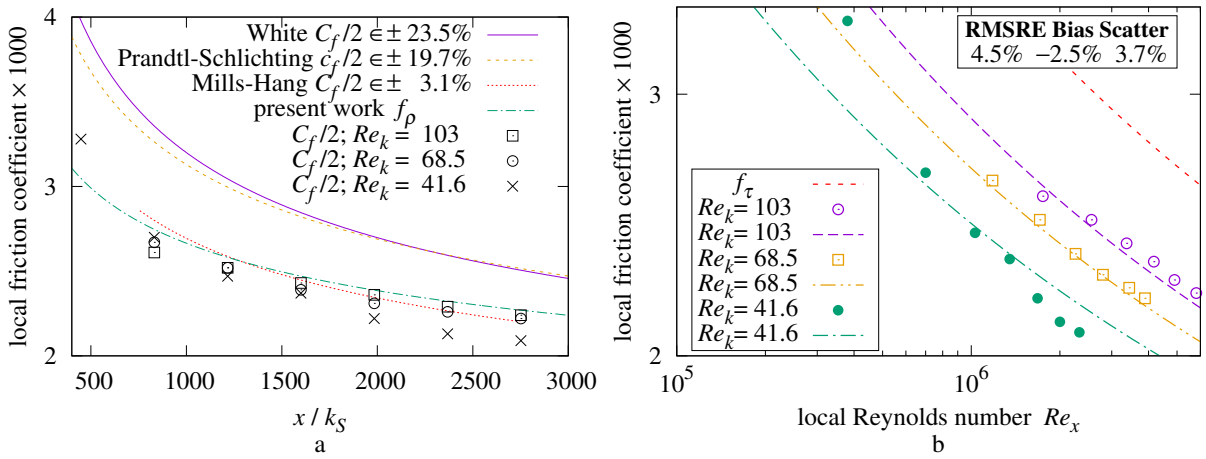

Figure 11. (**a**) Pimenta et al. [8] versus x/k_S; (**b**) Pimenta et al. [8] versus Re_x.

9.6. Comparison with Local Drag Measurements

The points labeled "$C_f/2; Re_k =$" in Figure 11a show the local drag coefficient measurements versus x/k_S for the sphere-roughened plate at three rates of flow. Table 4 presents RMSRE of this set of 19 measurements to each of the rough regime formulas.

Table 4. Local friction coefficient of sphere-roughened plate.

Source	Formula	RMSRE	Bias	Scatter	Used
Prandtl and Schlichting [3]	(7) $c_f/2$	15.6%	−15.4%	2.6%	19/19
Mills and Hang [9]	(9) $C_f/2$	3.7%	−2.4%	2.8%	19/19
White [10]	(11) $C_f/2$	16.6%	−16.3%	3.3%	19/19
Present work	(43) f_ρ	4.5%	−3.0%	3.3%	19/19

Formula (62) calculates x/ε from the Re_x and $Re_\varepsilon = Re_k/5.333$ values supplied by Pimenta et al. [8]. Figure 11b plots local $f_\rho(x/\varepsilon)$ versus Re_x for the sphere-roughened plate.

- These measurements have an RMSRE of 4.5% from f_ρ Formula (43).

9.7. Continuous Average to Local Skin-Friction

For continuous boundary layers, the transform for local friction f_c given average friction $\overline{f_c}$ is:

$$\frac{f_c(Re_x)}{\overline{f_c}(Re)} = \frac{1}{\overline{f_c}(Re)} \frac{\mathrm{d}\Big([Re_x - Re_0]\,\overline{f_c}(Re_x)\Big)}{\mathrm{d}Re_x} \tag{44}$$

The local skin-friction coefficient for turbulent flow f_τ can be derived from $\overline{f_\tau}$ Equation (33), Formula (44), and W_0 identity (45), provided that $Re_x \geq Re_0 \geq \sqrt{3}\,\mathrm{e}$ and $Re_x \gg \sqrt{3}\,\mathrm{e}$:

$$\frac{\mathrm{d}\mathrm{W}_0(\vartheta)}{\mathrm{d}\vartheta} \equiv \frac{\mathrm{W}_0(\vartheta)}{\vartheta\,[\mathrm{W}_0(\vartheta)+1]} \tag{45}$$

$$f_\tau(Re_x) = \frac{W_0^2\left(Re_x/\sqrt{3}\right) - 2\left[1 - Re_0/Re_x\right] W_0\left(Re_x/\sqrt{3}\right) - 1}{\left[W_0\left(Re_x/\sqrt{3}\right) - 1\right]^3 \left[W_0\left(Re_x/\sqrt{3}\right) + 1\right]} \tag{46}$$

9.8. Comparison with Local Measurements

Table 5 compares measurements at $10^5 \leq Re_x \leq 10^{10}$ made by Smith and Walker [22] and Spalding and Chi [23] with "present work" Formula (46) and formulas collected by Churchill [11].

Table 5. Local turbulent performance.

Source	RMSRE	Bias	Scatter
Schultz–Grunow	8.5%	+5.5%	6.6%
White	4.2%	−2.9%	3.0%
Von Karman	3.7%	+0.7%	3.6%
Schlichting	3.6%	−2.4%	2.7%
Spalding	3.4%	−2.5%	2.3%
Churchill Equation (16)	3.0%	−2.3%	2.0%
present work	1.9%	+1.2%	1.4%
Churchill Equation (18)	1.3%	+0.6%	1.2%

When calculating RMSRE, the error due to the variation in a single sample tends to be larger than the error when that variation is distributed among multiple samples. Thus, local measurements tend to have a larger RMSRE than average measurements do. Other than "Churchill Equation (18)", this is the case when comparing Table 5 with Figure 7.

- The Churchill local data-set has 1.9% RMSRE versus "present work" Formula (46).

9.9. Skin-Friction in Liquids

Figure 12 compares f_τ Formula (46) with skin-friction measurements in several fluids from Žukauskas and Šlančiauskas [18].

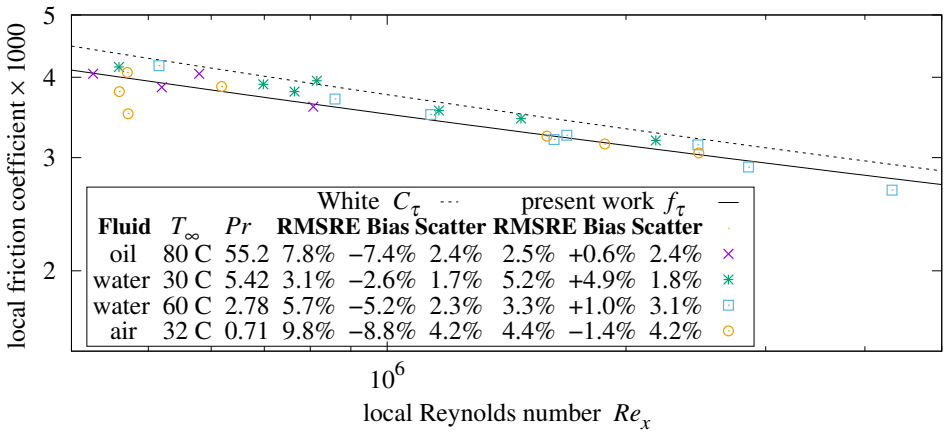

Figure 12. Local f_τ versus Re_x of smooth plate [18].

A fluid's Prandtl number (Pr) is its kinetic viscosity per thermal diffusivity ratio. Fluids with $Pr \gg 1$ transport heat primarily via fluid flow; conduction dominates heat transfer in fluids with $Pr \ll 1$.

- These data-sets have 2.5–5.2% RMSRE versus "present work" Formula (46).
- No significant dependence on Pr is manifested.

10. Forced Convection

Forced convective heat transfer is expressed as the (dimensionless) average Nusselt number $\overline{Nu} \equiv \overline{h}\, L/k$, where k is the fluid's thermal conductivity ($\mathrm{W}/(\mathrm{m}\cdot\mathrm{K})$) and $\overline{h}$ is the plate's average convective surface conductance in that fluid ($\mathrm{W}/(\mathrm{m}^2\cdot\mathrm{K})$). The local version, $Nu \equiv h\, x/k$, has the same units.

10.1. Rough Plate

The disruption which transfers momentum can also transfer heat. Hence, heat transfer will grow with $Re\, \overline{f_\rho}$.

Jaffer [28] finds that the natural convection boundary layer of an upward-facing plate is disrupted by collision of the flows and their detachment from the plate's center; the other plate orientations have continuous boundary layers. Boundary layer disruption being the essence of rough flow, this investigation proposes that heat transfer grows with the same $\sqrt[3]{Pr}$ dependence as upward-facing natural convection.

Fluid heating by the leading part of the plate reduces heat transfer from the trailing part; hence, heat transfer is scaled by $1/2$. Expanding $\overline{f_\rho}$ from Equation (27) yields Formula (47) for rough average forced convection heat transfer, provided that $L/\varepsilon \gg 1$ and $Pr \geq 0$:

$$\overline{Nu_\rho} = \frac{Re\, \overline{f_\rho}\, Pr^{1/3}}{2} = \frac{Re\, Pr^{1/3}}{6\, \ln^2(L/\varepsilon)} \tag{47}$$

The present analysis for self-similar $\overline{f_\rho}$ did not involve continuous boundary layers; hence, it avoids the $Pr \geq 0.6$ restriction affecting Formula (48). Formula (47) is compared with measurements in Section 15.

10.2. Smooth Plate

For turbulent convection, Lienhard [29] recommends composing the Gnielinski Formula (48) with the White C_τ Formula (12), subject to $Pr \geq 0.6$:

$$Nu = \frac{Re_x\, Pr\, C_\tau/2}{1 + 12.7\,[Pr^{2/3} - 1]\,\sqrt{C_\tau/2}} \tag{48}$$

Lienhard states that Nu Formula (49) has similar accuracy for gases with $0.6 \leq Pr < 2$:

$$Nu = 0.0296\, {Re_x}^{4/5}\, Pr^{0.6} \tag{49}$$

$$\overline{Nu} = 0.037\, Re^{4/5}\, Pr^{0.6} \tag{50}$$

Smooth plate forced convection is similar to natural convection from a vertical plate; in both, fluid flows parallel to the plate's characteristic length axis, and is uniform across the plate's other axis. Jaffer [28] finds that stationary fluid conducts heat from the vertical plate with an effective Nusselt number $Nu_0 = 2^4/[\pi^2\, \sqrt[4]{2}] \approx 1.363$; Nu_0 is a coefficient factor of both the static and flow-induced heat transfer terms.

Flow-induced heat transfer grows with $Nu_0\, Re\, \overline{f_\tau}$. Because this heat traverses boundary layers, the Pr dependence is more complex than $Pr^{1/3}$. In Jaffer [28], the vertical-plate natural convection dependence is $\sqrt[3]{Pr/\Xi(Pr)}$, where $\Xi(Pr)$ is defined using ℓ^p-norm (discussed in Section 13) Formula (51) with $p = \sqrt{1/3}$:

$$\|\varphi, \vartheta\|_p \equiv [\,|\varphi|^p + |\vartheta|^p]^{1/p} \tag{51}$$

$$\Xi(Pr) = \left\| 1,\ \frac{0.5}{Pr} \right\|_{\sqrt{1/3}} \tag{52}$$

In Figure 13, $\sqrt[3]{Pr/\Xi(Pr)}$ is asymptotically $Pr^{1/3}$ at large Pr, and $\sqrt[3]{2}\, Pr^{2/3}$ at small Pr. At small Pr, conduction does not amplify forced convection as it does for natural convection;

the Pr exponent should be 1. An additional factor using the ℓ^3-norm accomplishes this. Formula (53) is asymptotically $\sqrt[3]{2}\,Pr$ when $Pr \ll 0.5$. The "$0.7\,Pr^{0.6}$" trace shows that Formula (53) has a slope close to Formulas (49) and (50) for gases.

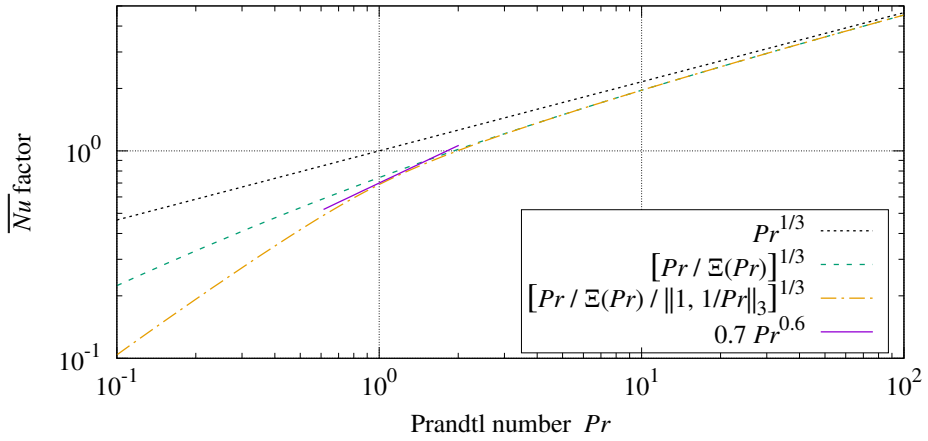

Figure 13. Smooth plate $\overline{Nu_\tau}$ dependence on Pr.

$$\sqrt[3]{\frac{Pr}{\Xi(Pr)}}\,\sqrt[3]{\frac{1}{\|1,1/Pr\|_3}} \tag{53}$$

The slope of Formula (48) $Nu(C_\tau)$ decreases with increasing Pr; at large Pr,Nu is proportional to $\sqrt{C_\tau}$ ($Nu \propto \sqrt{C_\tau}$). Recall from Equations (25) and (26) that $\overline{f_c} \propto u_\rho^2$; hence $\sqrt{\overline{f_c}} \propto u_\rho$. This indicates that transport through the boundary layer restricts heat transfer at large Pr. In order to reduce the asymptotic dependence from $\overline{f_\tau}$ to $\sqrt{\overline{f_\tau}}$, the convection formula will include a factor which takes the square-root of an expression gating $\overline{f_\tau}$ by Pr:

$$\sqrt{\frac{Pr/\sqrt{162}+1}{\sqrt{162}\,Pr\,\overline{f_\tau}+1}} \qquad \sqrt{162} \equiv 9\sqrt{2} \approx 12.7 \tag{54}$$

Note that 12.7 is a coefficient in the Gnielinski Formula (48).

The scaling for upstream heating was 1/2 in $\overline{Nu_\rho}$ Formula (47) for disruptive roughness; the turbulent boundary layer reduces this interaction; $\sqrt{1/3} \approx 0.577$ appears correct in the smooth case.

- Formula (55) is proposed for turbulent convection for all $Pr \geq 0$ and $Re \gg \sqrt{3}$ e:

$$\overline{Nu_\tau} = \frac{Nu_0\,Re\,\overline{f_\tau}}{\sqrt{3}}\sqrt{\frac{Pr/\sqrt{162}+1}{\sqrt{162}\,Pr\,\overline{f_\tau}+1}}\,\sqrt[3]{\frac{Pr/\Xi(Pr)}{\|1,1/Pr\|_3}} \tag{55}$$

10.3. Performance

Section 16 compares $\overline{Nu_\tau}$ Formula (55) with measurements over a wide range of Pr.

Lienhard [29] compares the Gnielinski–White convection formula with local measurements from studies of fluids with $0.7 \leq Pr \leq 257$ spanning $4000 < Re_x < 4.3 \times 10^6$. The smallest turbulent Re_x was $\approx 10^5$. Gas Formula (49) is more accurate than Gnielinski–White for turbulent air ($Pr \approx 0.71$) at $Re_x < 10^5$.

Figures 14 and 15 show $\overline{Nu_\tau}$ versus Pr and Re, respectively. The "present work" traces are Formula (55). The "averaged" traces use Formula (56) to numerically average the composition of the Gnielinski Formula (48) with the White Formula (12).

$$\overline{Nu}(Re) = \int_{Re_0}^{Re} \frac{Nu(Re_x)}{Re_x}\,\mathrm{d}Re_x \tag{56}$$

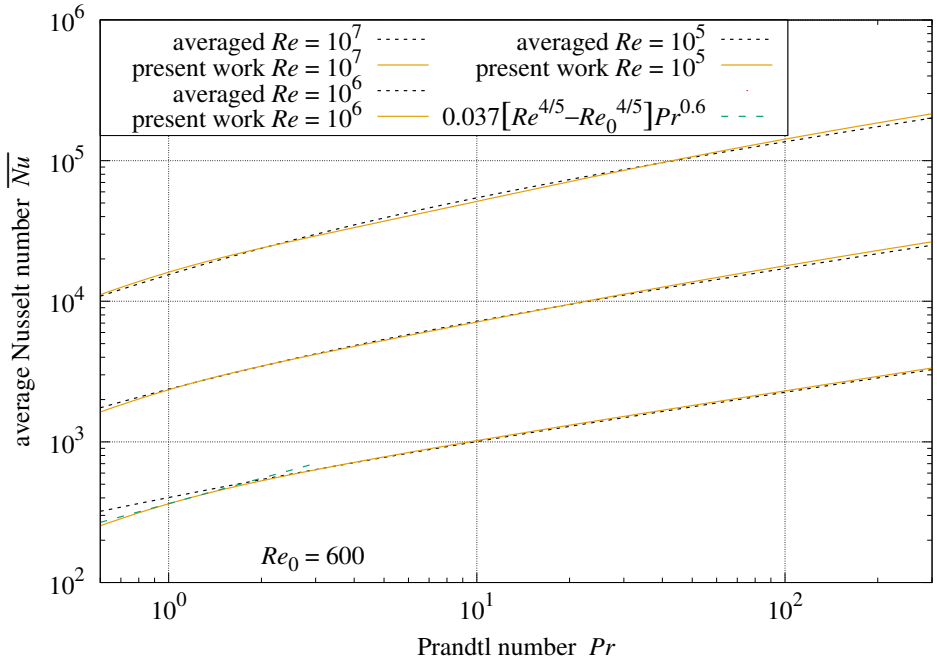

Figure 14. Smooth plate average turbulent convection versus *Pr* by *Re*.

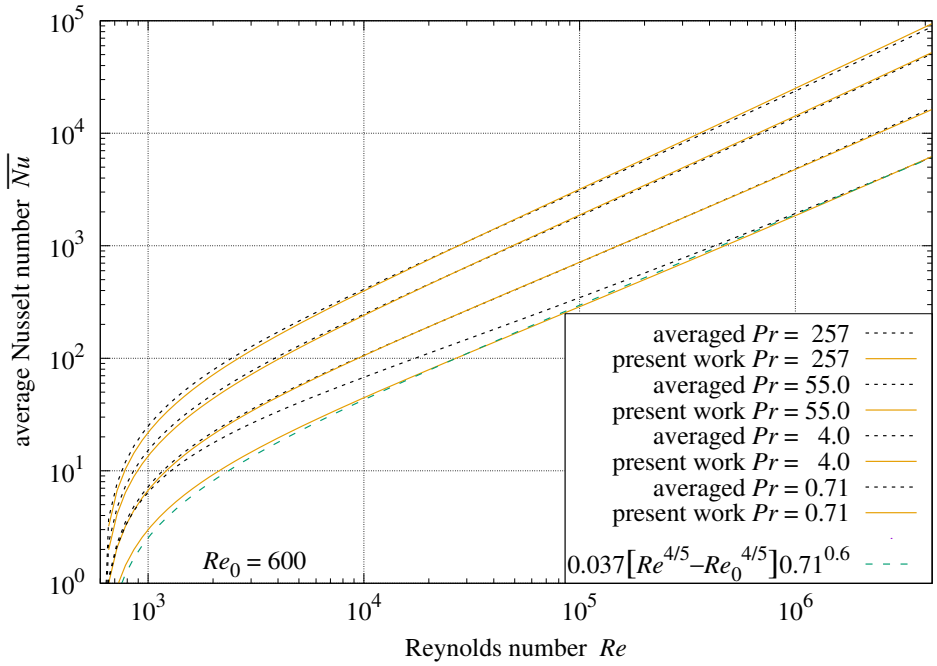

Figure 15. Smooth plate average turbulent convection versus *Re* by *Pr*.

Figure 16 shows the Gnielinski Formula (48) and local convection Nu_τ Formula (57) versus Re_x.

$$Nu_\tau(Re_x) = Re_x \frac{\mathrm{d}\overline{Nu_\tau}(Re_x)}{\mathrm{d}Re_x} \tag{57}$$

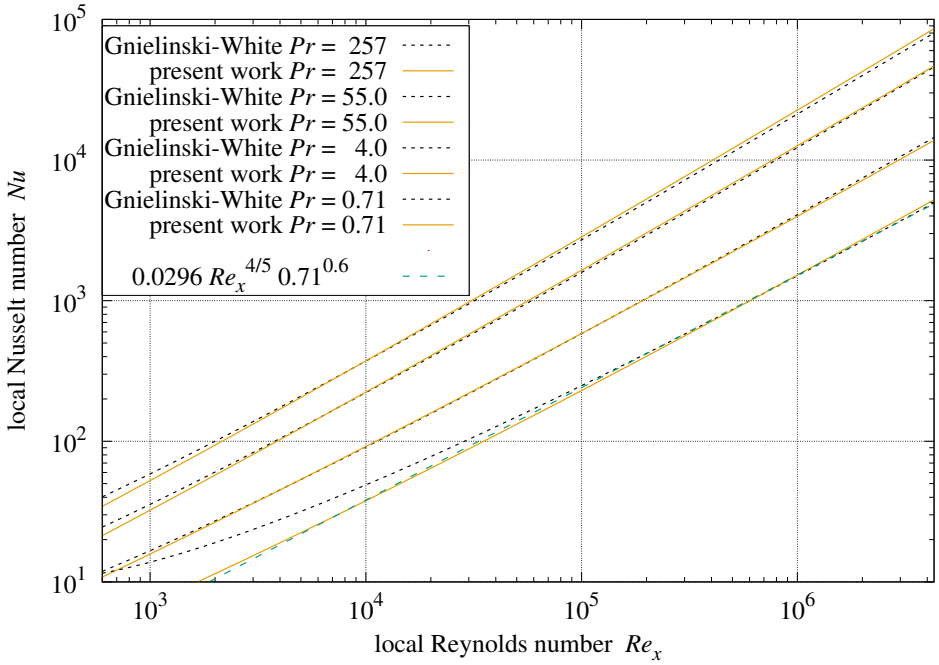

Figure 16. Smooth plate local turbulent convection.

- $\overline{Nu_\tau}$ Formula (55) matches the numerically averaged Gnielinski–White formula within $\pm 6.6\%$ over the range $10^5 < Re < 4.3 \times 10^6$ with $4.0 \leq Pr \leq 257$.
- At $Pr = 0.71$, $\overline{Nu_\tau}$ matches gases Formula (50) within $\pm 4\%$ over the range $10^4 < Re < 4.3 \times 10^6$.
- Over the same ranges, local convection Nu_τ Formula (57) matches Formulas (48) and (49) within $\pm 7.1\%$.

10.4. Laminar Forced Convection

Formula (58) is the Reynolds–Colburn [30] analogy relating laminar friction to forced convective heat transfer. Applying it to $\overline{f_\lambda}$ Formula (39), and scaling by the reduction in characteristic length due to an unheated starting band $x_u/L \equiv Re_u/Re$, yields the laminar forced convection Formula (59) given $Re \geq 0$, $Pr \geq 0$, and $0 \leq x_u \ll L$.

$$\overline{Nu}(Re) = \overline{f_c}(Re)\, Re\, Pr^{1/3}/2 \tag{58}$$

$$\overline{Nu_\lambda}(Re) = \frac{0.664\, Re\, Pr^{1/3}}{\sqrt{Re} + \sqrt{Re_0}} \left\{ 1 - \left\| 1, \frac{x_u}{L} \right\|_{-2} \right\} \tag{59}$$

- Section 16 tests $\overline{Nu_\tau}$ Formula (55) and $\overline{Nu_\lambda}$ Formula (59) extensively.

11. Onset of Rough Flow

- Periodicity organizes roughness such that the approximate onset Re of rough flow can be found from ε, L, and L_P.

For an isotropic, periodic roughness with $0 < \varepsilon < L_P \ll L$, there must be some value $Re_\lambda > 0$ such that when $0 < Re < Re_\lambda$, there is only laminar or turbulent fluid flow along the plate.

The boundary layer is thinnest at the leading edge. For isotropic, periodic roughness, any disruption will start within the leading band ($0 < x < L_P$) of roughness. This investigation considers a boundary layer disrupted when $\varepsilon > \delta_2(L_P)$, where $\delta_2(x)$ is the boundary layer momentum thickness at x.

11.1. Momentum Thickness

$\delta_2(x)$ is the thickness of bulk flow having the same momentum flow rate as the plate's boundary layer at x. δ_2 is not directly measurable. Schlichting [7] gives the momentum thickness of laminar and turbulent boundary layers as Formulas (60) and (61), respectively:

$$\delta_{2\lambda}(x) = \frac{0.664\,x}{{Re_x}^{1/2}} = 0.664\,\sqrt{Re_x}\,\frac{L}{Re} \tag{60}$$

$$\delta_{2\tau}(x) = \frac{0.036\,x}{{Re_x}^{1/5}} = 0.036\,{Re_x}^{4/5}\,\frac{L}{Re} \tag{61}$$

Laminar $\delta_{2\lambda}$ derives from the Blasius boundary layer model. Turbulent $\delta_{2\tau}$ is less certain.

Momentum thickness $\delta_2(x)$ is a local property of the fluid flow. In order to work locally with Re_ε Formula (28), change $L \to x$ and $Re \to Re_x$; then solve $Re_\varepsilon = 1$ for x/ε:

$$\frac{Re_x}{\sqrt{3}} = \frac{x}{\varepsilon}\ln\frac{x}{\varepsilon} \qquad \frac{x}{\varepsilon} = \exp\left(\mathrm{W}_0\left(\frac{Re_x}{\sqrt{3}}\right)\right) \tag{62}$$

Re_x is proportional to x ($Re_x \propto x$); hence, the turbulent momentum thickness $\delta_2(x)$ should be proportional to the product of x and u_ρ/u Formula (24). Eliminating x/ε using Formula (62):

$$\delta_2(x) \propto \frac{x}{\sqrt{3}\,\ln(x/\varepsilon)} = \frac{x}{\sqrt{3}\,\mathrm{W}_0\left(Re_x/\sqrt{3}\right)} \tag{63}$$

The proposed Formula (64) coefficient is $1/3^3 \approx 0.0370$, which may relate to $\varphi^\varphi \equiv \exp(\varphi\,\ln\varphi)$.

$$\delta_2(x) = \frac{x}{3^3\,\mathrm{W}_0\left(Re_x/\sqrt{3}\right)} \tag{64}$$

Figure 17a demonstrates that "turbulent δ_2" Formula (64) and "Schlichting $\delta_{2\tau}$" Formula (61) nearly match between the origin and the intersection of the laminar and turbulent curves at:

$$Re_x = \left[\frac{0.664}{0.036}\right]^{10/3} \approx 16579 \tag{65}$$

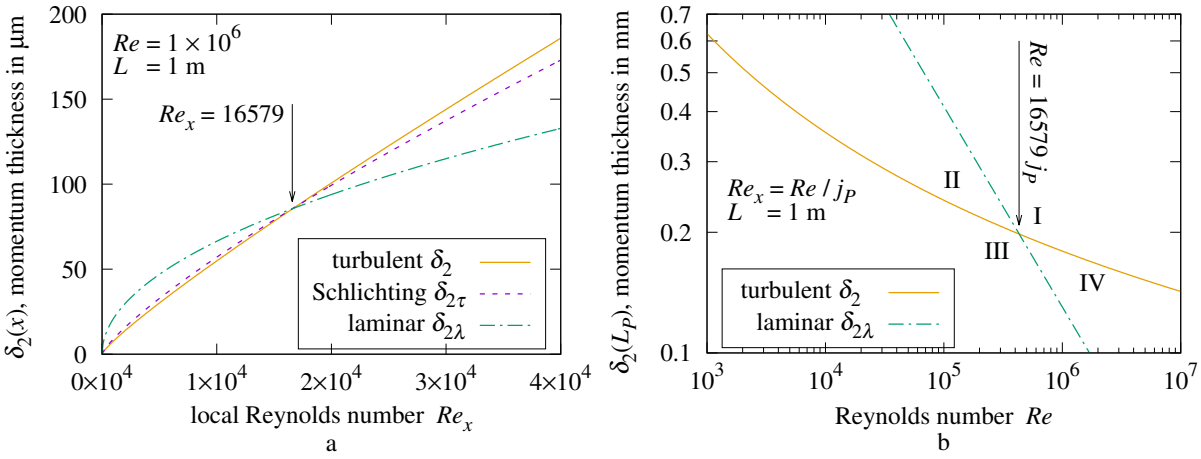

Figure 17. (**a**) smooth plate $\delta_2(x)$ versus Re_x; (**b**) Smooth plate $\delta_2(L_P)$ versus Re.

- Thus, $\delta_{2\tau}(L_P)$ is a reasonable approximation for $\delta_2(L_P)$ in the leading band of roughness.

11.2. Flow Mode Re Bounds

Figure 17b shows the leading band momentum thickness of laminar and turbulent flows along a 1 m long plate versus Re. The intersecting laminar $\delta_{2\lambda}$ and turbulent δ_2 curves partition the graph into four regions labeled I, II, III, and IV.

- When the point at coordinates $[Re, \varepsilon]$ is in region I, the roughness is sufficient to disrupt both laminar and turbulent flow; hence, the leading band fluid flow will be rough.
- When $[Re, \varepsilon]$ is in regions II or III, the roughness is not large enough to significantly disrupt laminar flow; hence, the leading band fluid flow will be laminar, possibly transitioning to turbulent.
- When $[Re, \varepsilon]$ is in region IV, the roughness would be sufficient to disrupt laminar flow, but not large enough to disrupt turbulent flow; hence, the leading band fluid flow would be turbulent.

With $\delta_{2\lambda} = \varepsilon$ and $x = L_P$, solve Formula (60) for the laminar upper-bound Re_λ:

$$Re_\lambda = \left[\frac{0.664}{\varepsilon}\right]^2 L_P\, L \tag{66}$$

With $x = L_P$ and $\delta_2(x) = \varepsilon$ in Formula (64) with $Re \gg \sqrt{3}\,\mathrm{e}\, L/L_P$:

$$\mathrm{W}_0\left(\frac{Re\, L_P}{\sqrt{3}\, L}\right) = \frac{L_P}{3^3\, \varepsilon} \tag{67}$$

The inverse of $\varphi = \mathrm{W}_0(\vartheta)$ is $\vartheta = \varphi \exp \varphi$. Solving for the turbulent upper-bound $Re_\tau = Re$:

$$Re_\tau = \frac{\sqrt{3}\, L}{3^3\, \varepsilon} \exp \frac{L_P}{3^3\, \varepsilon} \tag{68}$$

Equating Re_λ and Re_τ yields their intercept (found numerically) at $L_P/\varepsilon \approx 194.3$.

The combination of $L_P/\varepsilon > 194.3$ and $L \gg L_P$ required by region IV operation will be rare; $Re_\tau < Re_\lambda$ will hold for nearly all isotropic, periodic roughnesses.

12. Plateau Roughness

Self-similar roughness disrupts a boundary layer at all scales. At a minimum, isotropic, periodic roughness disrupts a boundary layer only every period $L_P \ll L$. Between these disruptions the RMS height-of-roughness must be smaller than ε because L_P is the dominant period. If this inter-roughness region is flat, parallel to the flow, and that flat is the tallest feature of each roughness cell, then a boundary layer can grow along it.

- If an isotropic, periodic roughness lacks flats parallel to the flow, then its shearing stress comes from the same flow–roughness interaction as a self-similar roughness induces, and the skin-friction coefficient will be $\overline{f_\rho}$ Formula (27).

Distinct flow mode regions can form along plates whose roughness peaks are all co-planar (at the same elevation) plateaus. With $Re > \max(Re_\tau, Re_\lambda)$ producing rough flow in the leading band of the plate, turbulent flow occurs downstream from where $\delta_2(x)$ is large enough to bridge the gaps. Theskin-friction drag from the downstream portion of the surface will be proportional to $\overline{f_\tau}$, not the constant $\overline{f_\rho}$ associated with rough flow. The combined skin-friction drag formula is developed in Section 13.

Informally, a "plateau roughness" is an isotropic, periodic roughness with most of its area at its peak elevation. Of particular interest are plateau roughnesses where each cell contains a single continuous plateau area whose boundary has a convex perimeter within the cell. This will either be an array of "islands" whose tops are all co-planar, or an array of "wells" dropping below an otherwise flat plane.

12.1. Plateau Islands

Consider a smooth flat plate etched with a square grid of grooves subjected to a $Re > \max(Re_\tau, Re_\lambda)$ flow. When the boundary layer is disrupted by a groove perpendicular to the flow, the turbulent boundary layer restarts at the leading edge of the next island. At the scale of the roughness period L_P, the momentum thickness of the boundary layer grows from 0 to nearly the L-scale $\delta_2(x)$ value (depending on the size of the island). If δ_2 grows to exceed ε, then the rest of the plate (to its trailing edge) will have a turbulent friction coefficient proportional to $\overline{f_\tau}$, but with characteristic length L_P.

Along isotropic roughness, the growth of δ_2 depends on plateau size, but not on orientation. An isotropic size metric is needed. In natural convection from an upward-facing horizontal plate [31,32], the (isotropic) characteristic length metric $L^* = A^*/p^*$, where A^* is the convex region's area and p^* is its perimeter length. For a regular polygon or circle, $L^* = r/2$, where r is the minimum radius of the regular polygon or circle.

In order to find the island Re_x threshold Re_I, multiply both sides of Equation (64) by $3^3 Re/[\sqrt{3}\,L]$. This allows Re_x to be isolated using the Lambert W_0 function identity $\varphi/\mathrm{W}_0(\varphi) = \exp \mathrm{W}_0(\varphi)$:

$$\frac{3^3 Re}{\sqrt{3}\,L}\,\delta_2 = \exp \mathrm{W}_0\left(\frac{Re_x}{\sqrt{3}}\right) \tag{69}$$

The boundary layer thickness needed to bridge the gap grows with ε and shrinks with increasing L^*/ε, suggesting $\delta_2 = \varepsilon^2/L^*$. The Re strength needed to reach δ_2 thickness at $x = L_P$ grows strongly with L/L_P. Letting $Re = [L/L_P]^3$ in Equation (69), then taking the logarithm of both sides:

$$\ln \frac{3^3\,\varepsilon^2\,L^2}{\sqrt{3}\,L^*\,L_P^3} = \mathrm{W}_0\left(\frac{Re_x}{\sqrt{3}}\right) \tag{70}$$

The inverse of $\varphi = \mathrm{W}_0(\vartheta)$ is $\vartheta = \varphi \exp \varphi$. Solving Formula (70) for $Re_I = Re_x$:

$$Re_I = \frac{3^3\,\varepsilon^2\,L^2}{L^*\,L_P^3} \ln \frac{3^3\,\varepsilon^2\,L^2}{\sqrt{3}\,L^*\,L_P^3} \qquad \frac{[4\,L^*]^2}{L_P^2} > \frac{1}{2} \tag{71}$$

With wide enough gaps, the islands are too narrow to support turbulent flow bridging the gaps, leading to the inequality in Formula (71). Formula (71) is tested against two square-grooved plates in Section 15.

12.2. Plateau Wells

Laying a perforated sheet on a flat plate turns its holes into wells. $L^* = A^*/p^*$. Fluid is forced up after diving into a well; instead of $Re = [L/L_P]^3$ in Formula (70), let $Re = L^3/[2\,L_P]^3$, leading to the wells Re_x threshold Re_W:

$$Re_W = \frac{3^3\,\varepsilon^2\,L^2}{2^3\,L^*\,L_P^3} \ln \frac{3^3\,\varepsilon^2\,L^2}{2^3\,\sqrt{3}\,L^*\,L_P^3} \qquad \frac{[4\,L^*]^2}{L_P^2} < \frac{1}{2} \tag{72}$$

With sufficiently wide wells, the flats between them are too narrow to support turbulent flow bridging the wells, leading to the inequality in Formula (72). Formula (72) is tested with perforated sheets in Section 14.

12.3. Openness

Let "openness" $0 < \Omega < 1$ be the non-plateau area per cell area ratio; $1 - \Omega$ is thus the "upper area fraction" of Section 8. Let $S_{s,t}$ be a $w \times w$ matrix of elevations. The span of elevations accepted as plateau must be a length smaller than ε and decrease with increasingL_P/ε, which suggests ε^2/L_P:

$$\Omega \approx \frac{1}{w^2} \sum_{t=0}^{w-1} \sum_{s=0}^{w-1} \begin{cases} 1, & S_{s,t} < \max(S) - \varepsilon^2/L_P \\ 0, & \text{otherwise} \end{cases} \tag{73}$$

This allows a quantitative definition of plateau roughness:

- "Plateau roughness" is an isotropic, periodic roughness with $\Omega < 1/2$.

An isotropic, periodic roughness which is not plateau roughness disrupts nascent boundary layers every L_P, but lacks the flat peaks necessary for turbulent layer growth. Thus, this investigation proposes:

- When $\Omega > 1/2$ and $Re > \max(Re_\tau, Re_\lambda)$, flow along the entire surface will be rough.

Note that $\Omega < 1/2$ does not replace inequalities (71) and (72); it is an additional constraint. However, they are related by "circularity".

12.4. Circularity

For island area A^* with perimeter p^*, circularity $o^* = 4\,\pi\,A^*/p^{*2}$ takes its maximum value, 1, in disks; it is $\pi\sqrt{3}/6 \approx 0.907$ in hexagons, $\pi/4 \approx 0.785$ in squares, and $\pi\sqrt{3}/9 \approx 0.605$ in equilateral triangles. Similarly, for square cell area A with perimeter p, circularity $o = 4\,\pi\,A/p^2$. Scaling by the circularity ratio derives $[4\,L^*]^2/L_P^2$ from $[1-\Omega]$.

$$[1-\Omega]\,\frac{o^*}{o} = \frac{A^{*2}}{p^{*2}}\,\frac{p^2}{A_P^2} = \frac{[4\,L^*]^2}{L_P^2} \tag{74}$$

Formula (74) is the same within a hexagonal cell, $A = \sqrt{3}/2\,L_P^2$ and perimeter $p = 2\,\sqrt{3}\,L_P$.

The plateau wells roughness formula replaces $[1-\Omega]$ with Ω:

$$\Omega\,\frac{o^*}{o} = \frac{A^{*2}}{p^{*2}}\,\frac{p^2}{A_P^2} = \frac{[4\,L^*]^2}{L_P^2} \tag{75}$$

The slope of each trace in Figure 18 is its o^*/o ratio. The "square/square" trace for a square array of square posts has slope 1. The "disk/hexagon" trace for a hexagonal array of circular wells has slope $\sqrt{12}/\pi \approx 1.1$. The "square/hexagon" trace for a hexagonal array of square posts has slope $\sqrt{3}/2 \approx 0.87$. Each trace spans the bounds for that bi-level configuration discovered in Section 8.

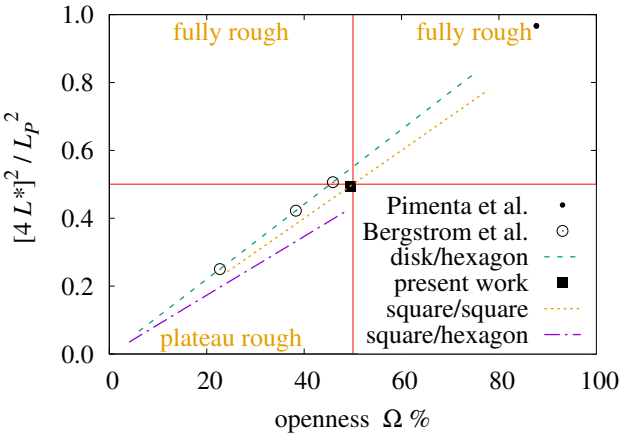

Figure 18. $[4\,L^*]^2/L_P^2$ versus Ω.

Also plotted are the Ω values of experiments by Pimenta et al. [8], Bergstrom et al. [13], and this investigation. The experiments of Sections 9, 14, and 15 find friction and heat transfer consistent with the type of flow named in three of the quadrants. The lower right quadrant would be reached when the convex region circularity is less than the cell circularity. But Section 8 found that such bi-level surfaces did not qualify as isotropic, periodic roughness when $\Omega > 1/2$. The Pimenta et al. plate did not have bi-level roughness.

- This experimental data locate the $[4\,L^*]^2/L_P^2$ threshold as being between 0.495 and 0.506.

13. Combining Transfer Processes

This unnamed form appears frequently in heat transfer formulas:

$$F^p(\xi) = F_0^p(\xi) + F_\infty^p(\xi) \tag{76}$$

Churchill and Usagi [33] stated that such formulas are "remarkably successful in correlating rates of transfer for processes which vary uniformly between these limiting cases". Convection and skin-friction are transfer processes. Convection transfers heat; skin-friction drag ($\propto Re\,f_c$) transfers momentum.

13.1. The ℓ^p-Norm

Requiring $F_0(\xi) \geq 0$ and $F_\infty(\xi) \geq 0$, and taking the pth root of both sides of Equation (76) yields a vector-space functional form known as the ℓ^p-norm, which is notated $\|F_0\ ,\ F_\infty\|_p$:

$$\|F_0\ ,\ F_\infty\|_p = [\ |F_0|^p + |F_\infty|^p]^{1/p} \tag{77}$$

Norms generalize the notion of distance. Formally, a vector-space norm obeys the triangle inequality: $\|y\ ,\ z\|_p \leq |y| + |z|$, which holds only for $p \geq 1$. The present work finds $p < 1$ useful as well.

Let $y \geq 0$ and $z \geq 0$. When $p > 1$, the processes compete and $\|y, z\|_p \geq \max(y, z)$; the most competitive is $\|y, z\|_{+\infty} \equiv \max(y, z)$. The ℓ^2-norm is equivalent to root-sum-squared; it models perpendicular competitive processes such as forced and natural convection from the present apparatus plate sides in Formula (A8).

The ℓ^1-norm models independent processes; $\|y, z\|_1 \equiv y + z$. It appears in Formulas (85), (86) and (87).

When $0 < p < 1$, the processes cooperate and $\|y, z\|_p \geq y + z$. Cooperation between conduction and flow-induced heat transfer uses the $\ell^{1/2}$-norm in natural convection [28]. Formula (52) uses the $\ell^{\sqrt{1/3}}$-norm from natural convection in forced convection.

When $p < 0$, $\|y, z\|_p \leq \min(y, z)$, with the transition sharpness controlled by p; the extreme is $\|y, z\|_{-\infty} \equiv \min(y, z)$. Negative p can model a single flow through serial processes; the most restrictive process limits the flow. The ℓ^{-2}-norm appears in the unheated starting length term of Formula (59), and in fan-speed Formula (A4). The ℓ^{-4}-norm appears in laminar-turbulent transition Formulas (80), (81), (84), (86) and (87).

13.2. Flow Modes

Isotropic, periodic surfaces with $Re_\tau < Re_\lambda$ and $\Omega > 1/2$ shed the rough flow of Formulas (27), (43), and (47) when $Re > Re_\lambda$. Plateau roughness ($\Omega < 1/2$) sheds either smooth or rough flow, or a combination. Table 6 proposes the behaviors of plateau islands and plateau wells roughnesses. If the $[4\,L^*]^2/L_P^2$ condition is not satisfied, then the Re_x conditions split the plate at distance x from the leading edge into regions operating in different modes. Formula (71) is the islands threshold Re_I; Formula (72) is the wells threshold Re_W.

Table 6. Flow modes for plateau roughness.

Islands Condition	Plateau Islands	Wells Condition	Plateau Wells
$[4\,L^*]^2/L_P^2 < 1/2$	rough Formulas (27), (43), (47)	$[4\,L^*]^2/L_P^2 > 1/2$	rough Formulas (27), (43), (47)
$Re_x < Re_I$	rough Formulas (27), (43), (47)	$Re_x < Re_W$	blend Formula (82)
$Re_x > Re_I$	smooth Formulas (78), (79)	$Re_x > Re_W$	smooth Formula (83)

13.3. Plateau Islands

The "$Re_x > Re_I$" flow mode is turbulent with characteristic length L_P. The island's plateau area is augmented by 1/2 of the non-plateau area and an area which grows with ε, combined using the ℓ^2-norm because ε and L_P are perpendicular:

$$\overline{f_I} = \left\{ 1 - \Omega + \left\| \frac{\Omega}{2}, \frac{2\,\varepsilon\,[4\,L^*]}{L_P^2} \right\|_2 \right\} \frac{L}{L_P}\,\overline{f_\tau}\left(\frac{Re\,L_P}{L}\right) \tag{78}$$

$$\overline{Nu_I} = \left\{ 1 - \Omega + \left\| \frac{\Omega}{2}, \frac{2\,\varepsilon\,[4\,L^*]}{L_P^2} \right\|_2 \right\} \frac{L}{L_P}\,\overline{Nu_\tau}\left(\frac{Re\,L_P}{L}\right) \tag{79}$$

$\overline{f_\rho}$ and $\overline{Nu_\rho}$ are active at $Re_x < Re_I$; $\overline{f_I}$ and $\overline{Nu_I}$ are active at $Re_x > Re_I$. The $\|Re, Re_I\|_{-4}$ term transitions between these parts gradually in Formulas (80) and (81). The $\left[\|Re, Re_I\|_{-4}/Re\right]$ factor normalizes the characteristic length in Formula (80).

$$\overline{f_\iota} = \overline{f_I}(Re) + \left[\|Re, Re_I\|_{-4}/Re\right]\left\{\overline{f_\rho} - \overline{f_I}(\|Re, Re_I\|_{-4})\right\} \tag{80}$$

$$\overline{Nu_\iota} = \overline{Nu_I}(Re) + \overline{Nu_\rho}(\|Re, Re_I\|_{-4}) - \overline{Nu_I}(\|Re, Re_I\|_{-4}) \tag{81}$$

Figure 19a shows that $\overline{Nu}$ and $\overline{f_c}$ are closely related in gases. Section 15 compares convection measurements from two bi-level plates with $\overline{Nu_\iota}$ Formula (81).

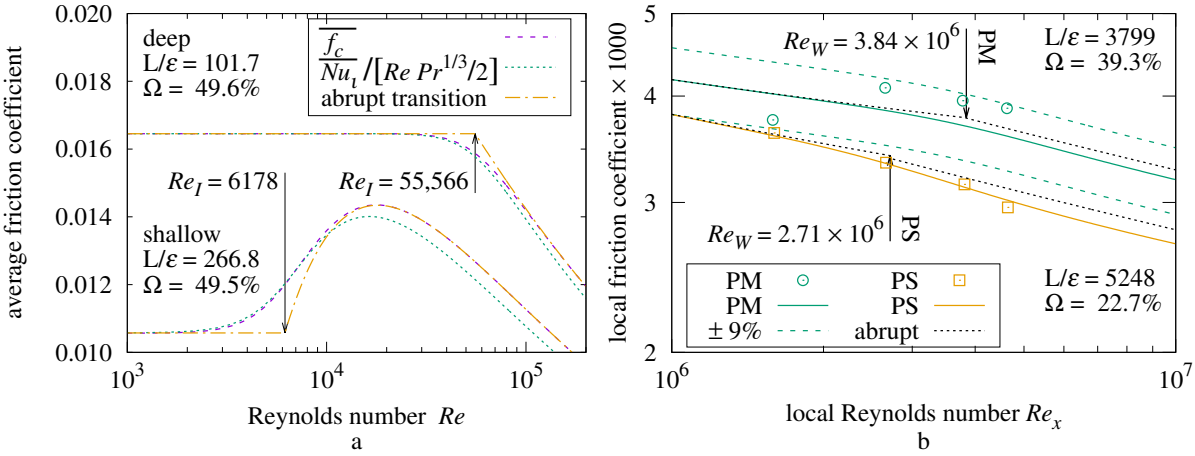

Figure 19. (**a**) Plateau islands friction; (**b**) plateau wells friction [13].

13.4. Plateau Wells

In "blend" mode, the plateau sheds turbulent flow while its wells shed rough flow. The effective friction coefficient is the area-proportional blend:

$$f_\beta = \Omega\,\overline{f_\rho}(L/\varepsilon) + [1 - \Omega]\,f_\tau(Re) \tag{82}$$

where $Re_x > Re_W$, the friction is turbulent, but with additional area $2\,\pi\,\varepsilon\,[4\,L^*]$. The well walls are perpendicular to the plateau, but only a portion of each well wall is parallel to the flow, which must divert to brush by both. A strength between $\ell^{\sqrt{2}}$ and ℓ^2 is needed; their geometric mean is $p = \sqrt[4]{8} \approx 1.682$:

$$f_W = \left\| 1, 2\,\pi\,\varepsilon\,[4\,L^*]/L_P^2 \right\|_{\sqrt[4]{8}} f_\tau(Re) \tag{83}$$

f_β is active at $Re_x < Re_W$; f_W is active at $Re_x > Re_W$:

$$f_\omega = f_W(Re) + \left[\|Re, Re_W\|_{-4}/Re\right]\left\{f_\beta(\|Re, Re_W\|_{-4}) - f_W(\|Re, Re_W\|_{-4})\right\} \tag{84}$$

The $Re_x = Re_W$ plane can split wells; thus the transition between f_β and f_W flows must be gradual in Formula (84). With the ℓ^{-4}-norm, the PM±9% (expected uncertainty) curves in Figure 19b bound the PM measurements from Bergstrom et al. [13]; the ℓ^{-2}-norm does not. Section 14 compares local friction measurements of perforated sheets with Formulas (83) and (84).

13.5. Staged-Transition

When laminar and turbulent flow occupy distinct plate regions separated at Re_c, their transfers combine using the ℓ^1-norm (addition). An abrupt transition at Re_c would behave as Formula (85). In practice, staged-transitions are not abrupt, behaving as the ℓ^{-4}-norm in Formulas (86) and (87). The subscript 4 is used to identify staged-transition formulas.

$$\left\| \frac{Re'}{Re}\,\overline{f_\lambda}(Re'),\ \overline{f_\tau}(Re) - \frac{Re'}{Re}\,\overline{f_\tau}(Re') \right\|_1 \qquad Re' = \min(Re,\ Re_c) \tag{85}$$

$$\overline{f_4} = \left\| \frac{Re'}{Re}\,\overline{f_\lambda}(Re'),\ \overline{f_\tau}(Re) - \frac{Re'}{Re}\,\overline{f_\tau}(Re') \right\|_1 \qquad Re' = \|Re,\ Re_c\|_{-4} \tag{86}$$

$$\overline{Nu_4} = \left\| \overline{Nu_\lambda}(Re_4),\ \overline{Nu_\tau}(Re) - \overline{Nu_\tau}(Re_4) \right\|_1 \qquad Re_4 = \|Re, \sqrt{2}\,Re_c\|_{-4} \tag{87}$$

Formula (87) models staged-transition convection. Convection's positive slope versus friction's negative slope requires scaling Re_c by $\sqrt{2}$ so that the lower edge of the transition is at Re_c. Formula (87) is tested in Section 16.

14. Rough Skin-Friction Measurements

Bergstrom et al. [13] has skin-friction coefficient measurements of sandpapers, woven wire meshes, and perforated sheets attached to a smooth plate, and also the 1.67 m × 1.16 m smooth plate alone. Skin-friction measurements were derived from Pitot probe measurements of air velocity at locations which were 1.3 m downwind from the leading edge of the plate. Bergstrom et al. [13] estimated 5% as the combined measurement uncertainty of the smooth surface friction coefficient, and 9% for the rough surfaces.

The measurement tables in [13] include a column for free-stream velocity, U_e. In order to compute the Reynolds number $Re = U_e\,L/\nu$, the kinematic viscosity $\nu = 16 \times 10^{-6}$ m^2/s was calculated for air at 20 °C, 25% RH, and 95 kPa, the mean atmospheric pressure at the University of Saskatchewan.

14.1. Smooth Plate

Three of the four measurements labeled "SM smooth" are within 5% of "present work f_τ" in Figure 20. The RMSRE versus f_τ Formula (46) is 4.8%; RMSRE versus White's C_τ Formula (12) is 9.6%.

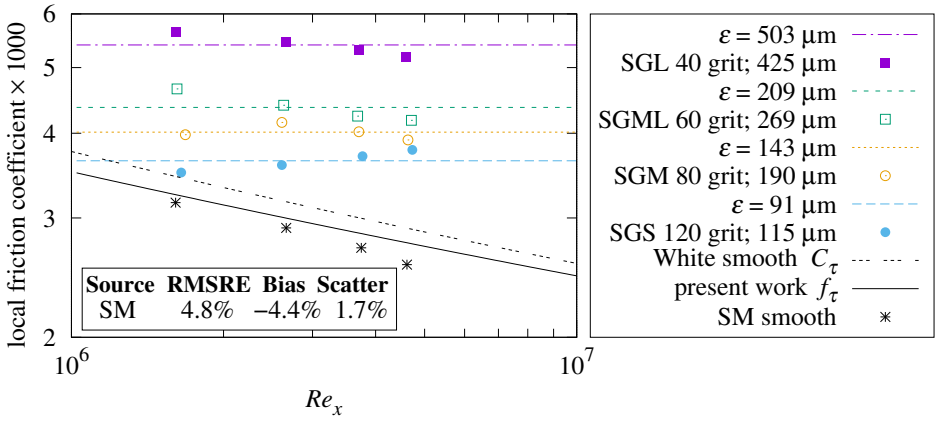

Figure 20. Local f_ρ versus Re_x of sandpaper [13].

14.2. Sandpaper

Microscopic examination of coarse grades of sandpaper reveals glued mounds of grits separated by canyons having depths that are several times the mean grit diameter. Sandpaper grit mean diameter is standardized, but not the height-of-roughness of the mounds; it can vary by manufacturer and lot. The horizontal traces in Figure 20 show that skin-friction coefficients which are independent of Re_x, as in the present theory, can be within the 9% estimated measurement uncertainty of the data.

14.3. Comparison with Sand-Roughness

The RMS height-of-roughness ε of sandpaper is much larger than ε of sand-roughness with the same mean grit diameter. For example, 40 grit sandpaper has a skin-friction coefficient consistent with $\varepsilon \approx 503\,\mu$m, while $k_S = 425\,\mu$m sand-roughness would have $\varepsilon = k_S/5.333 \approx 80\,\mu$m.

14.4. Woven Wire Mesh

Bergstrom et al. [13] has local skin-friction coefficient measurements of woven wire meshes attached to a smooth plate.

14.5. Mesh Openness

Woven wire meshes are specified by wire diameter d and wire center spacing s. Bergstrom et al. [13] calculate mesh openness as $[s - \sqrt{2}\,d]^2/s^2$ instead of the $[s-d]^2/s^2$ formula used by manufacturers (neither metric is plateau openness Ω). Table 7 lists the dimensions and openness from [13] along with openness calculated both ways. The WML and WMM meshes have $[s - \sqrt{2}\,d]^2/s^2$ values close to [13]. The WMS mesh has $[s - \sqrt{2}\,d]^2/s^2 \approx 49\%$, versus 44% from [13]. If the 1.68 mm spacing was instead 1.48 mm, WMS would have $[s - \sqrt{2}\,d]^2/s^2 \approx 44\%$, but significantly less friction coefficient than the WMS measurements in Figure 21. A 0.36 mm wire diameter has conventional openness $[s-d]^2/s^2 \approx 44\%$ and matches the WMS data and the WMM trace and data.

Table 7. Wire mesh dimensions.

Wire Diameter d	**Spacing** s	$[s-d]^2/s^2$	$[s-\sqrt{2}\,d]^2/s^2$	**From** [13]	**Tag**
1.04 mm	3.68 mm	52%	36%	35%	WML
0.58 mm	1.77 mm	45%	29%	30%	WMM
0.36 mm	1.68 mm	62%	49%	44%	WMS
0.36 mm	1.48 mm	58%	44%		
0.56 mm	1.68 mm	44%	28%		

14.6. Gaps

There are periodic gaps between the wires and the plate, so the mesh–plate combination is not strictly a roughness. With the gaps filled, the RMS height-of-roughness ε would be:

$$\begin{aligned} z(x,y) &= \sqrt{\frac{d^2}{4} - x^2} + d - \frac{d}{2}\cos\frac{\pi\,y}{s} \\ \overline{z} &= \frac{4}{s^2}\int_{d/2}^{s}\int_{0}^{d/2} z(x,y)\,\mathrm{d}x\,\mathrm{d}y \\ \varepsilon &= \frac{4}{s^2}\int_{d/2}^{s}\int_{0}^{d/2} |z(x,y)-\overline{z}|^2\,\mathrm{d}x\,\mathrm{d}y + \frac{[s-d]^2\,\overline{z}^2}{s^2} \end{aligned} \tag{88}$$

The periodic gaps between wires and the plate increase the flow's shearing stress. Scaling ε by the square root of the filled-gap per empty-gap side area ratio is an increase of about 26% for these meshes:

$$\varepsilon' = \varepsilon \sqrt{\frac{12\,s + \pi\,d}{8\,s}} \tag{89}$$

The "unscaled 1.04 mm, 3.68 mm" trace in Figure 21 shows the predicted WML friction without this scaling.

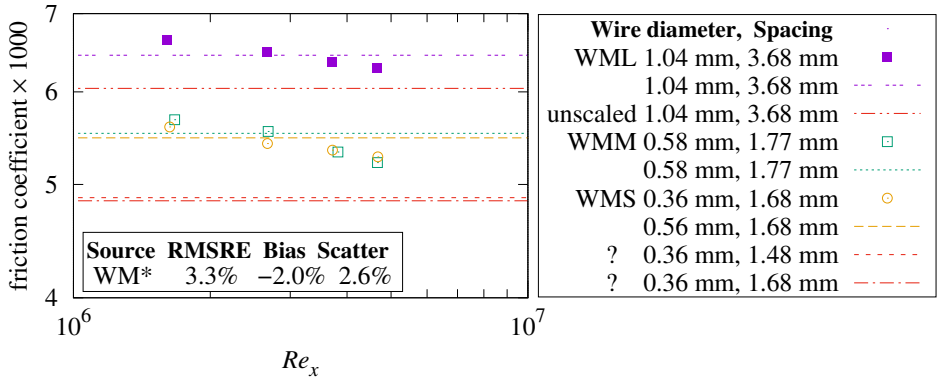

Figure 21. Local f_ρ versus Re_x of woven wire mesh [13].

- Using (scaled) ε', the WML and WMM measurements match the present theory well within the ±9% estimated measurement uncertainty. The WMS measurements do not match unless a hypothesized single digit misprint in [13] is corrected, changing the wire diameter from 0.036 mm to 0.056 mm. Taken together, the (corrected) three wire meshes have 3.3% RMSRE versus the present theory.

14.7. Perforated Sheet

Bergstrom et al. [13] has local skin-friction coefficient measurements of perforated sheets attached to a smooth plate.

14.8. Perforated Sheet Openness

Table 8 checks the openness of the perforated sheets from Bergstrom et al. [13]. It indicates that the holes were hexagonally arrayed. However, the PS sheet's calculated openness is 1/2 of the paper's 22%. There are two single digit changes, either of which results in hexagonal openness near 22%: hole diameter $d = 1.7\,\text{mm}$ or center spacing $s = 2.4\,\text{mm}$.

Table 8. Perforated sheet openness.

Hole Diameter d	Center Spacing s	Square Ω	Hexagonal Ω	[13] Ω	Tag
2.0 mm ≈ 5/64	2.81 mm ≈ 7/64	39.8%	45.9%	45%	PL
1.6 mm ≈ 4/64	2.43 mm ≈ 6/64	34.1%	39.3%	41%	PM
1.2 mm ≈ 3/64	3.40 mm ≈ 8.6/64	09.8%	11.3%	22%	PS
1.7 mm ≈ 4.3/64	3.40 mm ≈ 8.6/64	19.6%	22.7%		
1.2 mm ≈ 3/64	2.40 mm ≈ 6/64	19.6%	22.7%		

North American suppliers of perforated sheet metal generally specify hole diameter and center spacing in terms of 1/64 of an inch. Table 8 provides dimensions both ways. $d = 3/64$ with $s = 6/64$ is a standard size; $d = 4.3/64$ with $s = 8.6/64$ is not. Table 9 uses the parameters from the last row of Table 8.

14.9. Plateau Wells

Table 9 shows the dimensions and metrics of the ς-thick perforated sheets when laid on the flat plate. For PL, $[4\,L^*]^2/L_P^2 = d^2/s^2 \approx 0.507 > 1/2$; its flow will be rough. The "$f_\rho(2898) = 0.0052$" trace in Figure 22 shows the predicted local skin-friction coefficient's close proximity to the PL measurements. The "? 2.00 mm, 2.81 mm, 0.90 mm" trace with transition at "PL?" shows the behavior predicted if $d^2/s^2 < 1/2$ had been the case.

Table 9. Perforated sheet parameters.

$[4\,L^*] = d$	$L_P = s$	Ω	d^2/s^2	ς	ε	Re_W	Tag
2.0 mm	2.81 mm	45.9%	0.507	0.90 mm	0.449 mm	1.96×10^6	PL
1.6 mm	2.43 mm	39.3%	0.434	0.90 mm	0.441 mm	3.84×10^6	PM
1.2 mm	2.40 mm	22.7%	0.250	0.76 mm	0.318 mm	2.71×10^6	PS

PM and PS have $d^2/s^2 < 1/2$. As Re_x grows to exceed Re_W, the local drag coefficient gradually transitions from blend Formula (82) to smooth Formula (83). The Re_W Formula (72) transitions are marked by vertical lines. Figure 19b details the PS and PM abrupt and smooth transitions.

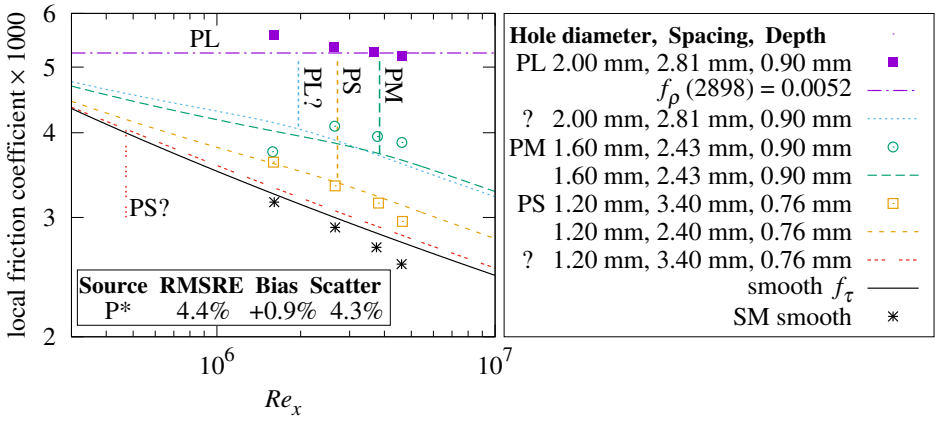

Figure 22. Local f_ρ versus Re_x of perforated sheet [13].

- PL and PM measurements match the present theory within the ±9% measurement uncertainty. The PS measurements do not match unless a hypothesized single digit misprint in [13] is corrected, changing the PS hole spacing from 3.4 mm to 2.4 mm. The "PS?" trace shows the behavior predicted of the original PS. Taken together, the (corrected) three perforated sheets have 4.4% RMSRE versus the present theory.

15. Rough Heat Transfer Measurements

Both the Pimenta et al. [8] and Bergstrom et al. [13] measurements are restricted to velocity ranges of less than 3:1. For a novel theory to be persuasive, confirmations over a wider range of fluid velocities are needed.

The present apparatus combined an open intake wind-tunnel, software phase-locked loop (PLL) fan control, and a heated aluminum plate. It measured average convection in air at $2300 < Re < 93{,}000$, a 40:1 range. Appendix A describes the apparatus and measurement methodology.

15.1. Bi-Level 3 mm Roughness

A square grid of 6 mm deep grooves in a 0.305 m × 0.305 m plate created the $\varepsilon = 3.0$ mm bi-level roughness.

The two peripheral $2\,\varepsilon \times L$ sides of the bi-level plate roughness which are parallel to the fluid flow also contribute to forced convection. Turning to dimensional analysis,

ε and plate width L_W cooperate weakly, leading to an effective width of $\|L_W, \varepsilon\|_{\sqrt{1/2}}$, about a 5.4% increase.

Applying average convection Formula (47) to the bi-level plate geometry, with the 5.4% increase, yields:

$$\overline{Nu_\rho}(Re) = 0.00823\, Re\, Pr^{1/3} \tag{90}$$

Note that this correction applies only to average $\overline{Nu_\rho}$ measurements, not to local Nu_ρ measurements.

Figure 23 shows convection measurements made with the plate averaging 11 K warmer than the ambient air. $\overline{Nu_\rho}$ is Formula (90); $\overline{Nu_\iota}$ is Formula (81). At $Re < 3000$, the natural convection component dominates the mixture; hence, measurements at $Re < 3000$ are excluded from the RMSRE calculations.

- Measurements in the range $4000 < Re < 50{,}000$ match $\overline{Nu_\rho}$ Formula (90) with 1.8% RMSRE.

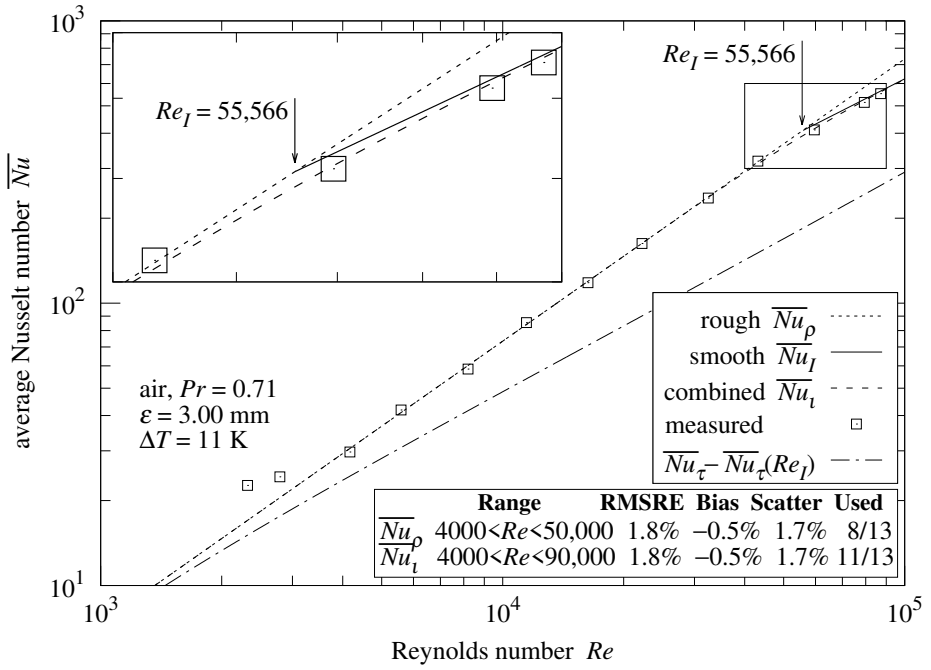

Figure 23. Convection from bi-level plate; $L/\varepsilon = 102$.

At $Re > Re_I = 55{,}566$, $\overline{Nu_I}$ is Formula (79); its 4/5 slope shows that convection is from turbulent flow. Its height above the $\overline{Nu_\tau} - \overline{Nu_\tau}(Re_I)$ trace shows that it is operating with a shorter characteristic length than $\overline{Nu_\tau} - \overline{Nu_\tau}(Re_I)$. The Figure 23 inset shows that $\overline{Nu_\iota}$ Formula (81) is a closer match to measurements at $60{,}000 < Re < 90{,}000$ than an abrupt transition.

- Measurements in the range $4000 < Re < 90{,}000$ match the plateau islands $\overline{Nu_\iota}$ Formula (81) with 1.8% RMSRE.

15.2. Bi-Level 1 mm Roughness

After making a variety of convection measurements, the $\varepsilon = 3$ mm plate was machined to reduce its roughness to $\varepsilon = 1.04$ mm.

In order to preserve the plate's wire suspension, the four corner posts were not shortened. The Re_I transition involves only the leading portion of the plate. $Re_I = 6178$ was calculated by Formula (71) using $\varepsilon = 1.14$ mm, the RMS height-of-roughness of the leading three rows of posts.

The plate's effective width, $\|L_W,\ \varepsilon\|_{\sqrt{1/2}}$, is about 2.6% larger than L_W, but affects only $\overline{Nu_\rho}$ flow at $Re < 6178$. $\overline{Nu_I}$ Formula (81) already accounts for smooth convection from the post sides.

In Figure 24, $\overline{Nu_\iota}$ is Formula (81). At $Re < 5000$, the natural convection component dominates the mixture; hence, measurements at $Re < 5000$ are excluded from the RMSRE calculations.

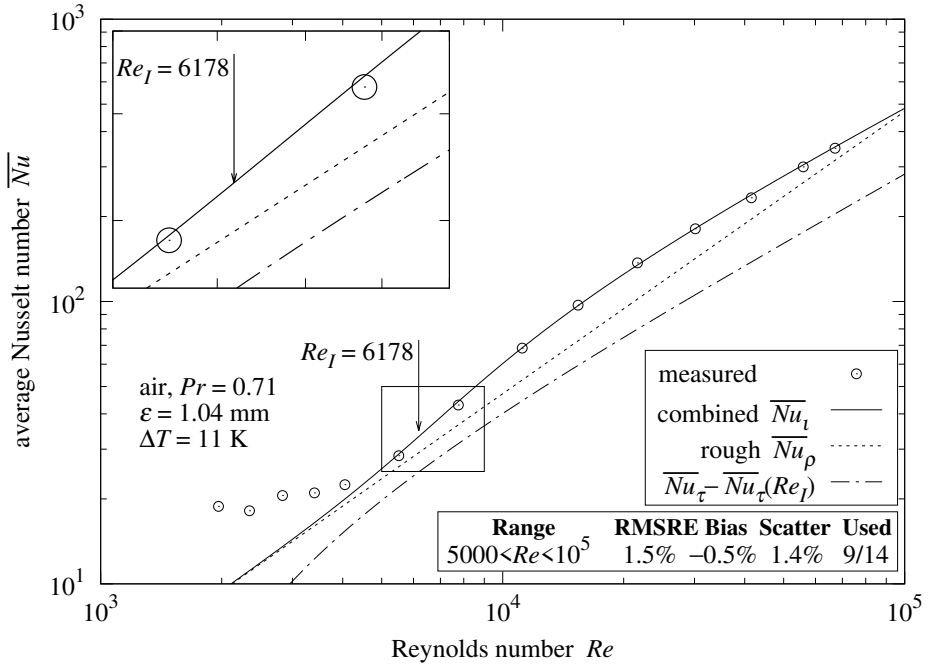

Figure 24. Convection from bi-level plate; $L/\varepsilon = 295$.

The ℓ^{-4}-norm in $\overline{Nu_\iota}$ Formula (81) fits very well with the measurements in Figure 24. Replacing it with the ℓ^{-2}-norm drives some $\overline{Nu}$ values out of the expected uncertainty bounds.

- Convection measurements at $5000 < Re < 10^5$ match plateau-islands Formula (81) with 1.5% RMSRE.

15.3. Onset of Rough Flow

Re_λ Formula (66) predicts that the flow along the leading band of roughness of the 3 mm bi-level plate transitions from laminar to rough flow at $Re_\lambda \approx 175$, which is too slow to test in this apparatus. Formula (66) predicts $Re_\lambda = 1473$ for the 1 mm bi-level plate. The plate was found to have convection consistent with rough flow at $Re \approx 2500$, which is less than $2\,Re_\lambda$.

16. Smoothness

Thus far, this investigation has focused on rough and turbulent flows. Attention now turns to laminar flows.

Schlichting [7] describes the behavior of parallel flow of "low turbulence intensity" along a sharp-edged, smooth surface as a "stable laminar flow following the leading edge", transitioning to a "fully developed turbulent boundary layer" at some $Re_x < 5 \times 10^5$. Lienhard [29] models a gradual Re_x transition between laminar and turbulent flow along the smooth plate.

16.1. Laminar Flow over Roughness

The amount of laminar flow displaced by a periodic roughness grows with both ε and L_P. Dimensional analysis suggests that this displacement is significant when

$Re > L/\sqrt{\varepsilon L_P}$. However, the laminar disturbance will be eclipsed by turbulent flow when $Re > Re_\tau$, leading to a proposed criterion:

- An isotropic, periodic roughness behaves as a "smooth" surface when $L/\sqrt{\varepsilon L_P} > Re_\tau$ and $Re < Re_\lambda$.

A silicon wafer is an isotropic, periodic roughness with $L_P = 543$ nm and $\varepsilon = 31.2$ nm. The "silicon wafer" has $L/\sqrt{\varepsilon L_P} > Re_\tau$ in Table 10; it should behave as a smooth surface when $Re < Re_\lambda$.

Table 10. Dimensionless surface parameters.

Surface	L/ε	$L/\sqrt{\varepsilon L_P}$		Re_τ		Re_λ
Silicon wafer	9.8×10^6	2.3×10^6	$>$	1.2×10^6	$\ll$	7.5×10^7
[8] Pimenta et al.	1.5×10^4	5.0×10^3	$>$	1.3×10^3	$\ll$	5.5×10^4
Duck tape	7.5×10^3	1.0×10^3	$<$	4.0×10^3	$\ll$	1.9×10^5
[13] Bergstrom et al. PS	4.6×10^3	1.5×10^3	$>$	4.3×10^2	$\ll$	2.0×10^4
[13] Bergstrom et al. PM	3.0×10^3	1.3×10^3	$>$	2.3×10^2	$\ll$	7.2×10^3
[13] Bergstrom et al. PL	2.9×10^3	1.2×10^3	$>$	2.3×10^2	$\ll$	8.0×10^3
[13] Bergstrom et al. WMS	3.0×10^3	1.5×10^3	$>$	2.2×10^2	$\ll$	5.1×10^3
[13] Bergstrom et al. WMM	2.9×10^3	1.5×10^3	$>$	2.1×10^2	$\ll$	5.0×10^3
[13] Bergstrom et al. WML	1.6×10^3	7.6×10^2	$>$	1.2×10^2	$\ll$	3.3×10^3
Present work 1 mm bi-level	2.9×10^2	8.8×10^1	$>$	2.9×10^1	$\ll$	1.5×10^3
Present work 3 mm bi-level	1.0×10^2	5.1×10^1	$>$	7.5×10^0	$\ll$	1.8×10^2

16.2. Pierced-Laminar Flow

Consider "duck tape", the only row in Table 10 with $L/\sqrt{\varepsilon L_P} < Re_\tau$.

Tuck and Kouzoubov [34] finds that slow laminar flow over a periodic roughness "...represents a shift of the apparent plane boundary toward the flow domain". At small Re, the flow from the apparent boundary plane outward is the same as smooth laminar flow. Thus, the roughness has little effect on shear stress when $Re < L/\sqrt{\varepsilon L_P}$.

- When $L/\sqrt{\varepsilon L_P} < Re_\tau$, the purely laminar upper-bound (critical Re) $Re_c = L/\sqrt{\varepsilon L_P}$.

Consider the boundary layer where $Re_c < Re_x < Re_\lambda$. Between the surface and its apparent boundary plane, shearing stress periodically (L_P) exceeds that of a smooth surface, spawning vortexes as Re increases, asymptotically approaching turbulent flow. This investigation terms this mixture "pierced-laminar flow"; the laminar flow is pierced by vortexes.

16.3. Smooth Laminar Flow

Reducing free-stream turbulence to unusually low values, Schubauer and Skramstad [19] reported that "oscillations were discovered in the laminar boundary layer along a flat plate". These periodic oscillations suggest that rough and smooth laminar flows both spawn vortexes periodically along the plate, controlled by the purely laminar upper-bound Re_c.

16.4. Laminar-Turbulent Mixing

The hypothesized periodic vortexes pierce the laminar boundary layer. The present theory holds that the laminar component is active through the entire $Re < Re_\lambda$ range in pierced-laminar flow, resulting in friction Formula (91) and convection Formula (92).

$$\overline{f_\sigma} = \left\| \overline{f_\lambda}(Re),\ \overline{f_\tau}(Re) - \frac{Re_\gamma}{Re}\,\overline{f_\tau}(Re_\gamma) \right\|_\gamma \qquad Re_\gamma = \left\| Re,\ \frac{Re_c}{\sqrt{\gamma}} \right\|_{\gamma'} \tag{91}$$

$$\overline{Nu_\sigma} = \left\| \overline{Nu_\lambda}(Re),\ \overline{Nu_\tau}(Re) - \overline{Nu_\tau}\Big(\|Re,\ \sqrt{\gamma}\,Re_c\|_{\gamma'} \Big) \right\|_\gamma \tag{92}$$

Because laminar and turbulent flows mix in pierced-laminar flow, the ℓ^1-norm and ℓ^{-4}-norm of staged-transition Formulas (86) and (87) are replaced by the ℓ^{γ}-norm and $\ell^{\gamma\prime}$-norm in Formulas (91) and (92). The laminar and turbulent flows are in mild competition, so $1 < \gamma < 2$. Figure 25a shows $\overline{f_c}$ Formula (91) curves at $1 \le \gamma \le 2$ and $-8 \le \gamma\prime \le -4$. Smaller γ results in a sharper downward bend, while more negative $\gamma\prime$ results in a sharper upward bend. Letting $\gamma\prime = -8/\gamma$ links the variables to sharpen the bends together within their respective ranges.

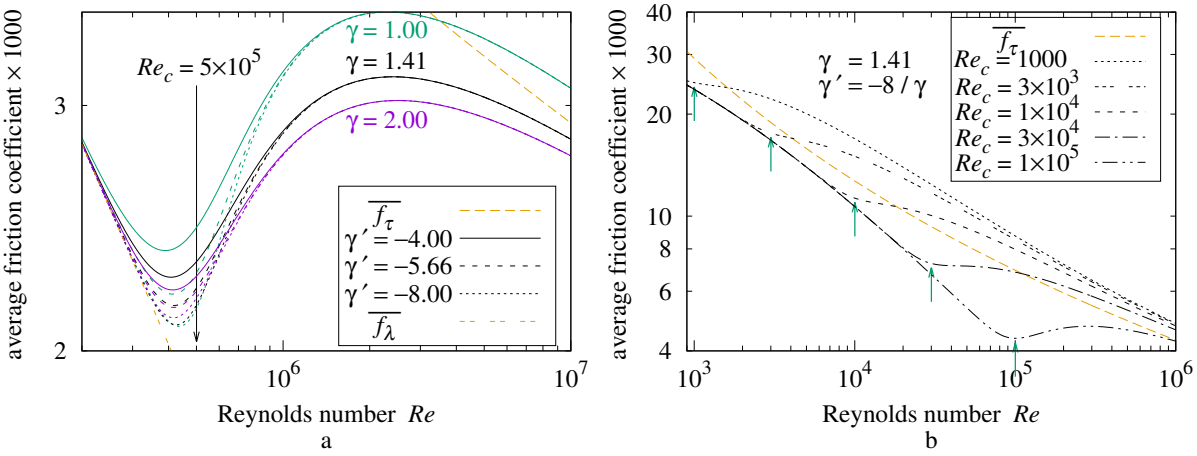

Figure 25. (**a**) Pierced-laminar friction by $\gamma, \gamma\prime$; (**b**) Pierced-laminar friction by Re_c.

The geometric mean of 1 and 2 is $\sqrt{2}$; for the moment, assume $\gamma = \sqrt{2}$ and $\gamma\prime = 8/\gamma = 4\sqrt{2}$.

Figure 25b plots Formula (91) at five Re_c values. Note that traces with smaller Re_c have larger friction coefficients than the turbulent $\overline{f_\tau}$ trace.

Figure 26 compares measurements from Gebers [20,21] with staged-transition Formula (86), pierced-laminar Formula (91), and Formula (93) from Schlichting [7] for an apparatus with $Re_c = 5 \times 10^5$, which is marked with a vertical green arrow.

$$0.455/\log_{10}^{2.58} Re - 1700/Re \tag{93}$$

- The Gebers [20,21] measurements have 2.8% RMSRE from Formula (91) with $Re_c = 5 \times 10^5$.

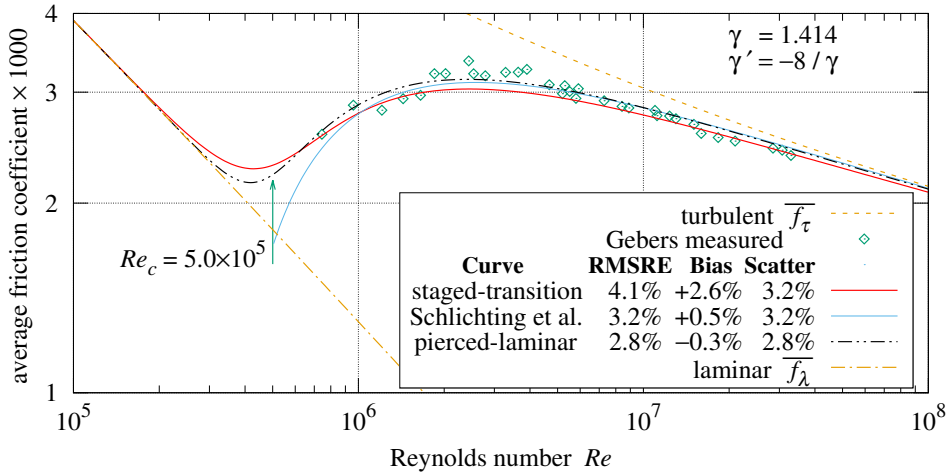

Figure 26. Average friction versus Re of smooth plate [20,21].

16.5. Duck Tape

The bi-level test plate assembly of the present apparatus has four sides perpendicular to the test-surface, each a wedge of extruded polystyrene foam (XPS) insulation filling a 2.7 cm 45° chamfer in the metal slab. In order to isolate the convective heat flow of the test-surface from that of the sides, the estimated side convection, between 50% at $Re = 6000$ and 7% at $Re = 90{,}000$ of the measured heat flow, is deducted from that measured heat flow (see Appendix A for details).

The surface of the XPS foam board in Figure 27a was not smooth and not an isotropic, periodic roughness. Without a theoretical basis for computing its convective heat transfer, the accuracy of measurements of the surface-under-test would have been limited. Hence, the foam was covered with Intertape AC6 duck tape, a 152 µm thick polyester cloth/polyethylene film with a pressure-sensitive adhesive (shown in Figure 27a). The geometric mean of its 3.62 mm × 1.47 mm thread cell is $s \equiv L_P \approx 2.31$ mm; the thread diameter plus the sheet thickness is $d \approx 0.10$ mm. The filled-gap woven wire mesh Formula (88) calculates $\varepsilon \approx 0.0403$ mm. These values with $L = 0.305$ m yielded the "duck tape" row in Table 10.

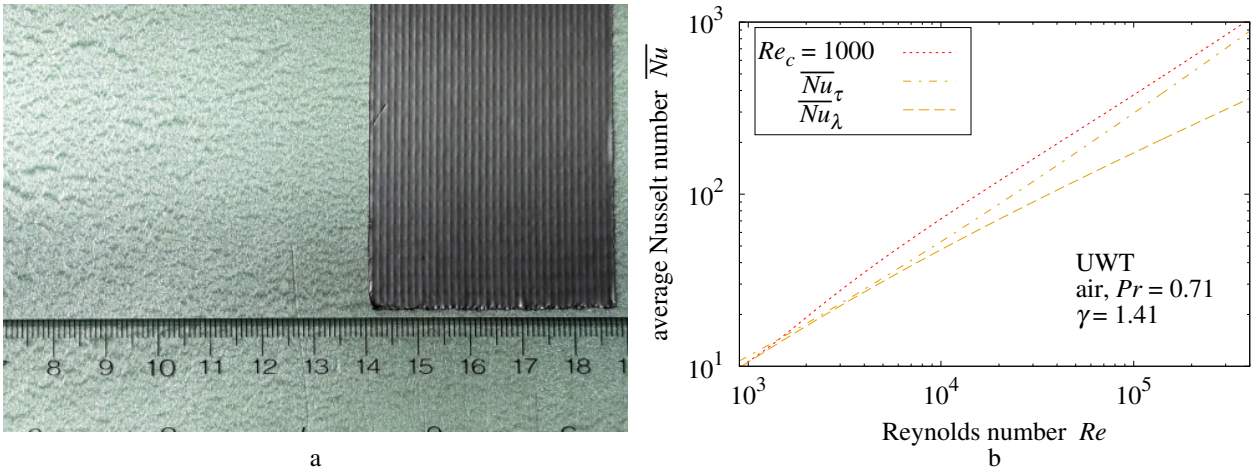

Figure 27. (**a**) XPS foam board and duck tape; (**b**) duck tape convective heat transfer.

16.6. Pierced-Laminar Convection from Roughness

In the present theory, an $L = 0.305$ m strip of duck tape fails to generate rough flow in the present apparatus because the apparatus's largest $Re \approx 93000 < Re_\lambda \approx 1.9 \times 10^5$. Because $Re_\tau > L/\sqrt{\varepsilon L_P}$ in the duck tape row of Table 10, the critical $Re_c = L/\sqrt{\varepsilon L_P} \approx 1.0 \times 10^3$ in $\overline{Nu}_\sigma$ Formula (92) convection.

With duck tape applied to the foam faces, the measurements presented in Section 15 are consistent with the side convection modeled by pierced-laminar Formula (92). The other curves in Figure 27b are substantially less than Formula (92); they do not account for enough heat transfer to keep the surface-under-test measurements within the expected uncertainty bounds presented in Appendix A.

That consistency rules out laminar $\overline{Nu}_\lambda$, turbulent $\overline{Nu}_\tau$, and staged-transition $\overline{Nu}_4$ as explanations of convection from the duck tape covered sides in combination with plateau islands $\overline{Nu}_\iota$ convection from the plate. This evidence is not conclusive, but supports pierced-laminar Formula (92) convection from the duck tape surface.

16.7. Local Skin-Friction and Convection

Average-to-local transform (44) derives Formulas (94) and (96) from Formulas (86) and (91), with Re_c scaled by $\sqrt{2}$. Formulas (95) and (97) compute the local convections from the average convection Formulas (87) and (92), with Re_c scaled by $\sqrt{\gamma}$. These Re_c scale factors are needed to make the local curve transitions align with Re_c.

$$f_4 = \frac{\mathrm{d}[Re_x - Re_0]\,\overline{f_4}(Re_x, \sqrt{2}\,Re_c)}{\mathrm{d}Re_x} \tag{94}$$

$$Nu_4 = Re_x\,\frac{\mathrm{d}\overline{Nu_4}(Re_x, \sqrt{\gamma}\,Re_c)}{\mathrm{d}Re_x} \tag{95}$$

$$f_\sigma = \frac{\mathrm{d}[Re_x - Re_0]\,\overline{f_\sigma}(Re_x, \sqrt{2}\,Re_c)}{\mathrm{d}Re_x} \tag{96}$$

$$Nu_\sigma = Re_x\,\frac{\mathrm{d}\overline{Nu_\sigma}(Re_x, \sqrt{\gamma}\,Re_c)}{\mathrm{d}Re_x} \tag{97}$$

16.8. Convection Transition

The Lienhard [29] comprehensive smooth plate convection formula can be expressed using the ℓ^p-norm:

$$Nu(Re_x) = \left\| Nu_\lambda(Re_x), \left\{ \left\| Nu_\lambda(Re_c)[Re_x/Re_c]^c, Nu_\tau(Re_x) \right\|_{-10} \right\} \right\|_5 \tag{98}$$

$$Nu_\lambda(Re_x) = 0.332\,\sqrt{Re_x}\,Pr^{1/3} \Big/ \sqrt[3]{1 - [Re_u/Re_x]^{3/4}} \tag{99}$$

$$c = 0.9922\,\log_{10} Re_c - 3.013 \tag{100}$$

Re_c is the critical Re_x upper-bound for purely laminar flow. Lienhard [29] states "The value of Re_c should be fit to the dataset, and the value of c may either be fitted or estimated from" Formula (100). The Lienhard curves presented here use the c estimated by Formula (100).

In the graphs which follow, the Re_c and c values fit by Lienhard [29] are marked with a star ($*$). The curves are computed and labeled with the Re_c value which minimizes the data-set RMSRE (relative to the formula) using the "Golden section search" algorithm from Kiefer [35].

Figure 28 plots measurements from two Kestin, Maeder, and Wang [24] data-sets. Figure 29 plots data from Reynolds, Kays, and Kline [25] at $Pr = 0.70$ with unheated $Re_u = 23,479$. Pierced-laminar Formula (97) has the closest match (lowest RMSRE) to the measurements in Figures 28 and 29.

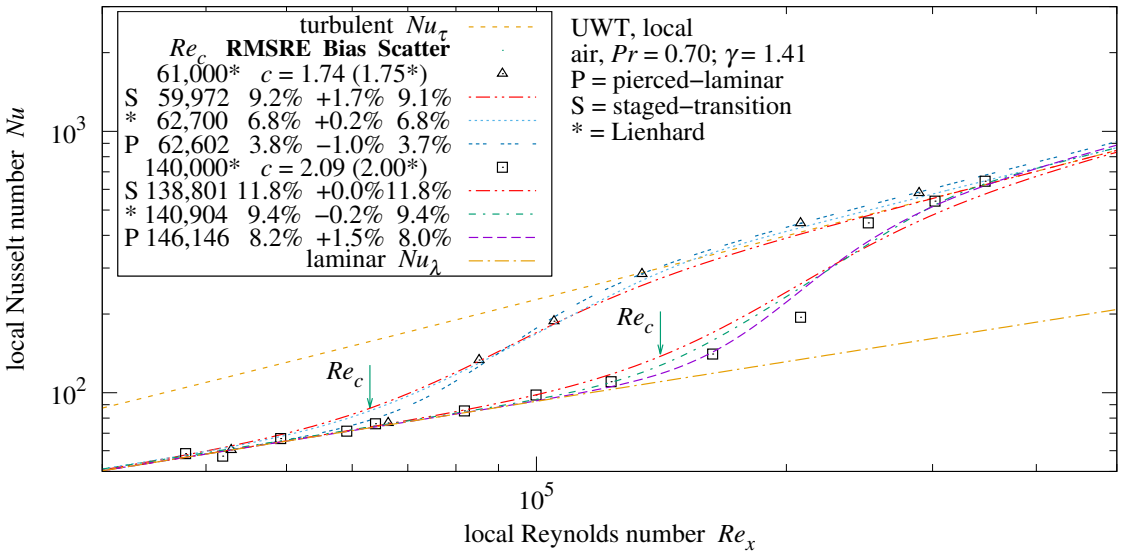

Figure 28. Kestin et al. [24] local convection critical transition.

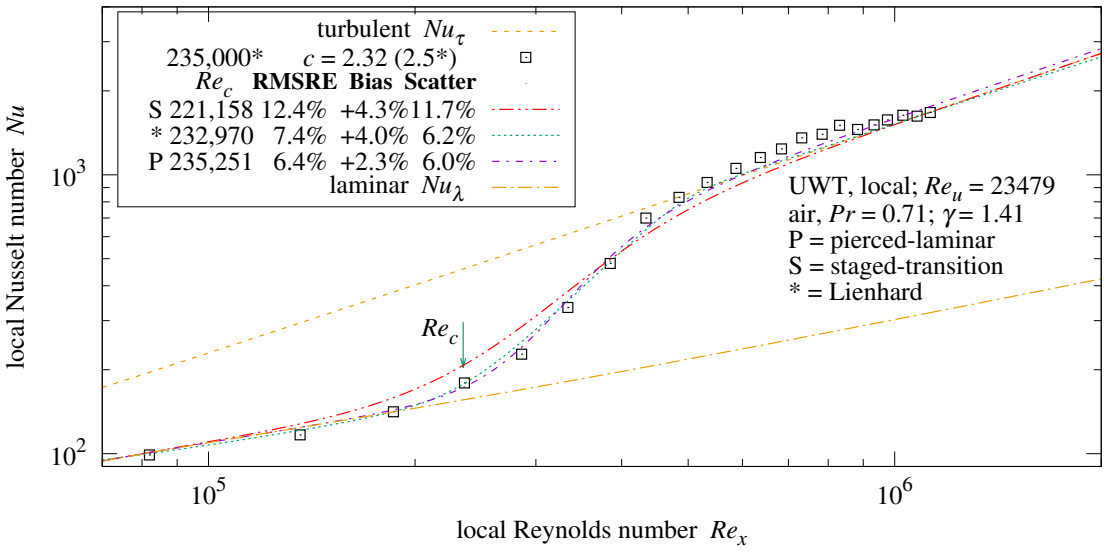

Figure 29. Reynolds et al. [25] local convection critical transition.

16.9. Uniform Heat Flux

Thus far, this investigation concerned uniform-wall-temperature (UWT, also termed "isothermal") plates. Žukauskas and Šlančiauskas [18] measured critical transitions with a uniform-heat-flux (UHF) flowing through a smooth surface. In the present work, each convection graph is labeled UWT or UHF.

Per Lienhard [29], 0.4587 replaces 0.332 in Nu_λ Formula (99) for UHF plates. Similarly, $0.4587/0.332 \approx 1.382$ scales $\overline{Nu}_\lambda$ Formula (59) when modeling UHF plates.

Lienhard [29] uses the Gnielinski turbulent Formula (48) for both UWT and UHF plates. This investigation similarly applies its turbulent Formula (55) to both UWT and UHF plates.

When a vortex transports fluid away from the surface of a UHF plate, the temperature of the fluid which replaces it increases more slowly than it would from a UWT plate. This reduction in local surface temperatures interferes with laminar heat transfer, largely restricting it to the $Re_x < Re_c$ region of the plate. Staged-transition Formula (87) models heat transfer from distinct laminar and turbulent areas, making it appropriate for UHF convection. Note that the fluid flow is the same; only its heat transfer is affected.

Figure 30 compares staged-transition Formula (95), Lienhard Formula (98), and pierced-laminar Formula (97) with measurements by Žukauskas and Šlančiauskas [18] of UHF plates in air.

The two points of each Figure 30 data-set at $Re_x < 5 \times 10^4$ are far from the transition range of interest. Disregarding them reveals that the three data-sets match (S) staged-transition Formula (95) with RMSRE less than 2.6%; the other formulas have more than twice this RMSRE.

- Pierced-laminar Formula (97) matches UWT transitions more closely than Formula (95).
- Staged-transition Formula (95) matches UHF transitions more closely than Formula (97).

Thus far, all the UWT transition data-sets have been in air at $Pr \approx 0.71$. Žukauskas and Šlančiauskas had $Pr > 1$ transition data-sets measured from UHF plates. How are UWT and UHF behaviors related?

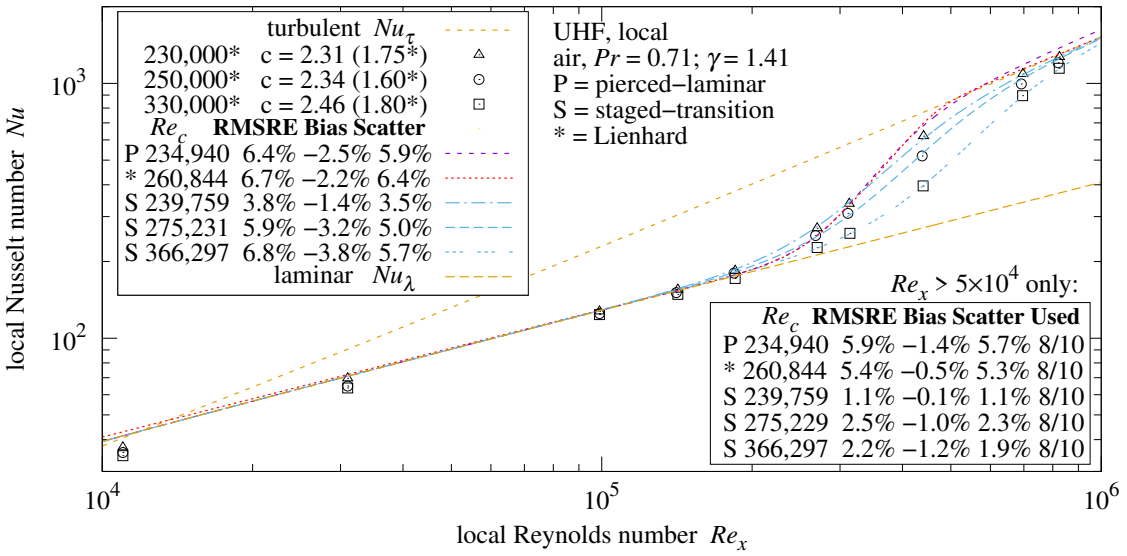

Figure 30. Žukauskas and Šlančiauskas [18] air critical transition.

Staged-transition and pierced-laminar heat transfer will not coincide at $Re_x < Re_c$ because of their different laminar heat transfer coefficients. Fluids with larger Pr will transport more heat away from the UHF plate's warmer regions, reducing the temperature variations across the plate. Thus, UHF and UWT heat transfer formulas should converge at large Pr and $Re > Re_c$.

- At $Re > \sqrt[4]{2}\,Re_c$ the staged-transition curve is nearly identical to the pierced-laminar curve with $\gamma = 2$ and $\gamma\prime = -8/\gamma = -4$ in Figure 31a. Therefore, convection γ varies with Pr, and $\lim_{Pr\to\infty} \gamma(Pr) = 2$.
- Comparison of pierced-laminar curves with convection measurements from Kestin et al. [24] in Figure 28 and Reynolds et al. [25] in Figure 29 establishes that $\gamma(0.71) \approx 1.41$.
- Mild competition between laminar and turbulent flows suggests $\lim_{Pr\to 0} \gamma(Pr) = 1$.

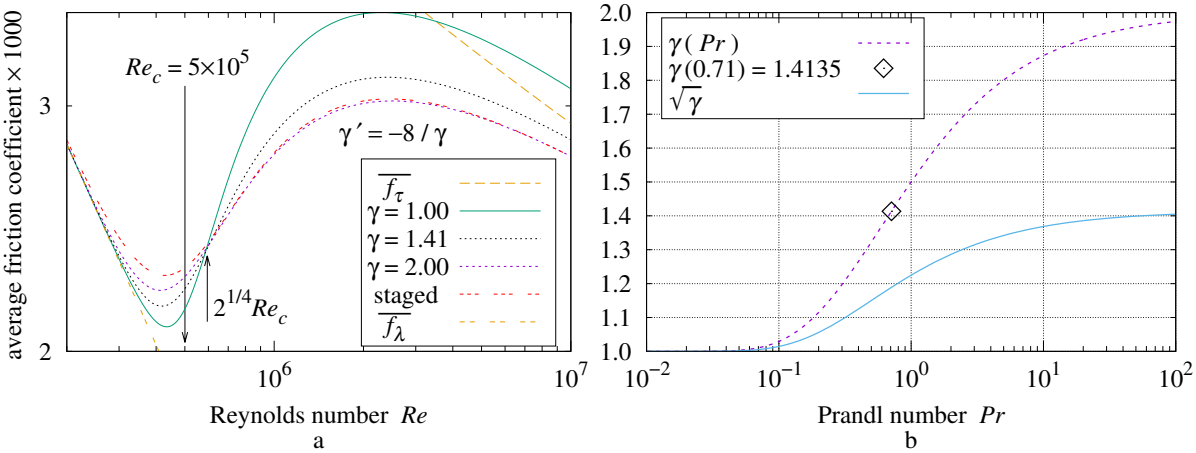

Figure 31. (**a**) Pierced and staged friction; (**b**) $\gamma(Pr)$ and $\sqrt{\gamma}$.

- Figure 31b graphs proposed Formula (101), which satisfies these three constraints.

$$\gamma(Pr) = 1 + \exp_2\left(-Pr^{-\sqrt{1/2}}\right) \qquad \exp_2(\varphi) \equiv 2^\varphi \tag{101}$$

Note that γ and $\gamma\prime$ are Pr dependent only in convection. Graphing friction coefficient instead of heat transfer in Figure 31a isolates the ℓ^p-norms from the effects of Pr on laminar and turbulent heat transfer.

16.10. Viscous Liquids

Žukauskas and Šlančiauskas [18] measured critical transitions in liquid water and transformer oil. The Pr of those fluids is sensitive to temperature. They recommended scaling the bulk fluid Pr_∞ by $\sqrt[4]{Pr_w/Pr_\infty}$ to yield $Pr = Pr_w^{1/4} Pr_\infty^{3/4}$, where Pr_w is at plate temperature. In the presence of vortexes, the surface temperature of a UHF plate is not well-defined; this investigation treats UHF $Pr = Pr_\infty$. Žukauskas and Šlančiauskas [18] also scaled their UHF Nu measurements by $\sqrt[4]{Pr_\infty/Pr_w}$; the UHF data presented here are descaled.

Figures 32 and 33 compare Lienhard Formula (98), pierced-laminar Formula (97), and staged-transition Formula (95) with UHF transition measurements in $Pr > 1$ fluids by Žukauskas and Šlančiauskas [18]. Lienhard Formula (98) has 1.8% RMSRE on the $Pr_\infty = 257$ data-set in Figure 32, but larger RMSRE than staged-transition Formula (95) on the other data-sets.

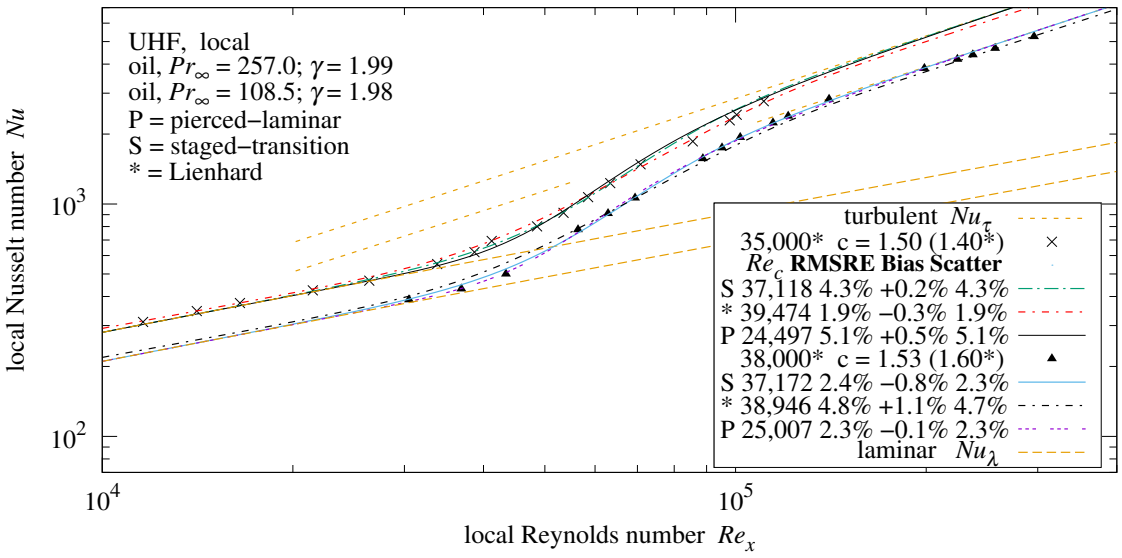

Figure 32. Žukauskas and Šlančiauskas [18] oil-critical transition.

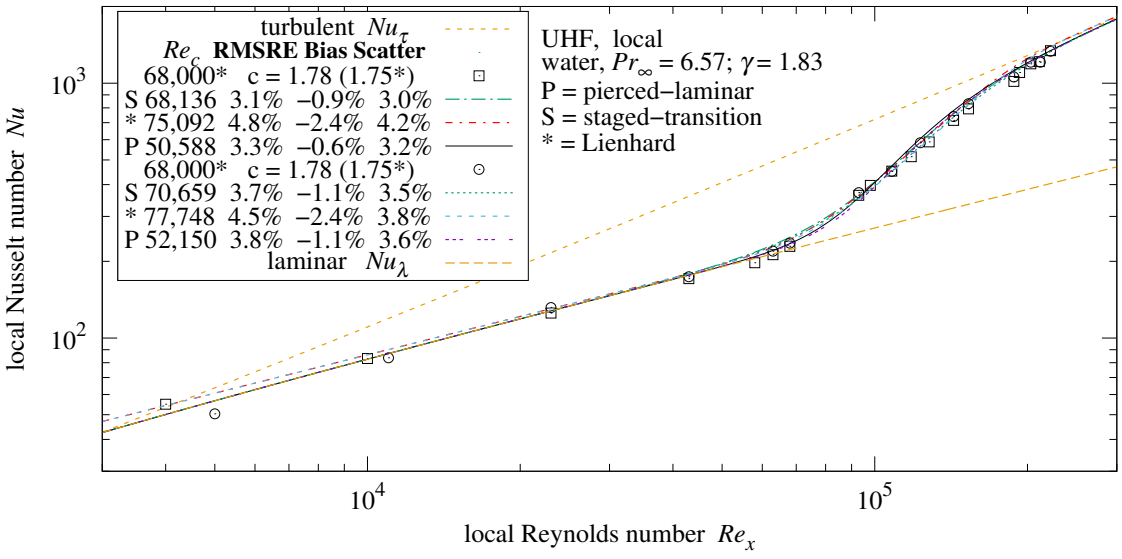

Figure 33. Žukauskas and Šlančiauskas [18] water-critical transition.

- With Re_c optimized to minimize RMSRE (at $Pr = Pr_\infty$), the Žukauskas and Šlančiauskas [18] UHF data-sets align to staged-transition Formula (95) with RMSRE less than 5%.

16.11. UWT at Large Temperature Differences

Thus far, the heat transfer measurements have all been local. Žukauskas and Šlančiauskas [18] also measured average UWT heat transfer in air and liquids at the wide variety of fluid and plate temperatures paired in Figure 34. Testing both cooled and heated plates, this is a rigorous but challenging set of measurements because T_∞, T_w, and Re are independent parameters. Adding to that challenge, $|T_w - T_\infty|/T > 10\%$ for many measurements in the UWT data-sets.

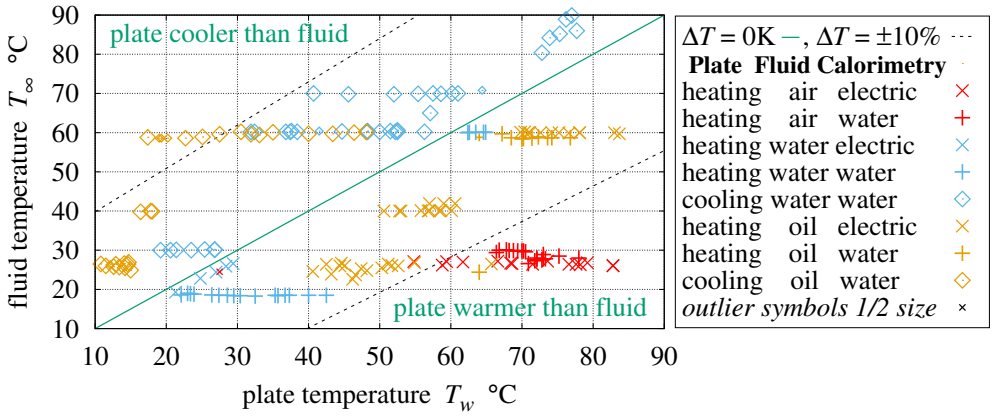

Figure 34. UWT plate-fluid temperature pairs [18].

While this investigation uses $Pr = Pr_\infty$ for UHF plates, for UWT plates it uses $Pr = Pr_w^{1/4} Pr_\infty^{3/4}$ (which Žukauskas and Šlančiauskas [18] recommended for both types).

In the large temperature difference data-sets which follow, the numerically averaged version of Lienhard's comprehensive Formula (98) had RMSRE values exceeding 10%; they are not tabulated here.

16.12. Air

Žukauskas and Šlančiauskas [18] contains a table of fluid properties by temperature. However the air properties were for dry air, as shown in Figure 35a. The monthly average relative humidity (RH) in Kaunas, Lithuania, where the experiments were likely performed, varies between 70% and 90%. Appendix B details the humid-air model assembled from formulas in Kadoya, Matsunaga, and Nagashima [36], Wexler [37], Tsilingiris [38], and Morvay and Gvozdenac [39]. The large relative errors in Figure 35b shows that the Žukauskas and Šlančiauskas [18] fluid table is inconsistent with 80% RH at air pressure $P = 100.725$ kPa.

Using the humid air model at 80% relative humidity, Figure 36 shows the air data-sets versus turbulent $\overline{Nu_\tau}$ and pierced-laminar $\overline{Nu_\sigma}$. A single measurement excluded as an outlier is represented as a half-sized symbol. Figure 34 also represents outliers with half-sized symbols.

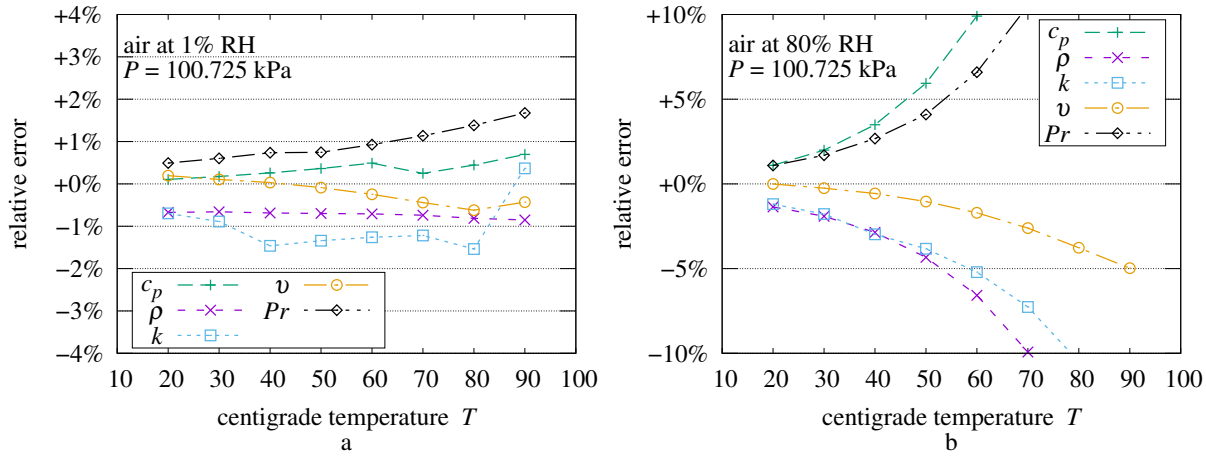

Figure 35. (**a**) Air property fits at 1% RH [18]; (**b**) Air property fits at 80% RH [18].

These measurements were obtained from plates incorporating either an electric heater or a water-based calorimeter in a separate apparatus for each type of fluid. Žukauskas and Šlančiauskas [18] intended to measure turbulent convection, not critical transitions in these UWT convection data-sets; most of the $Re > Re_c$. Hence, Re_c is the data-set fitted value or 600, whichever is greater.

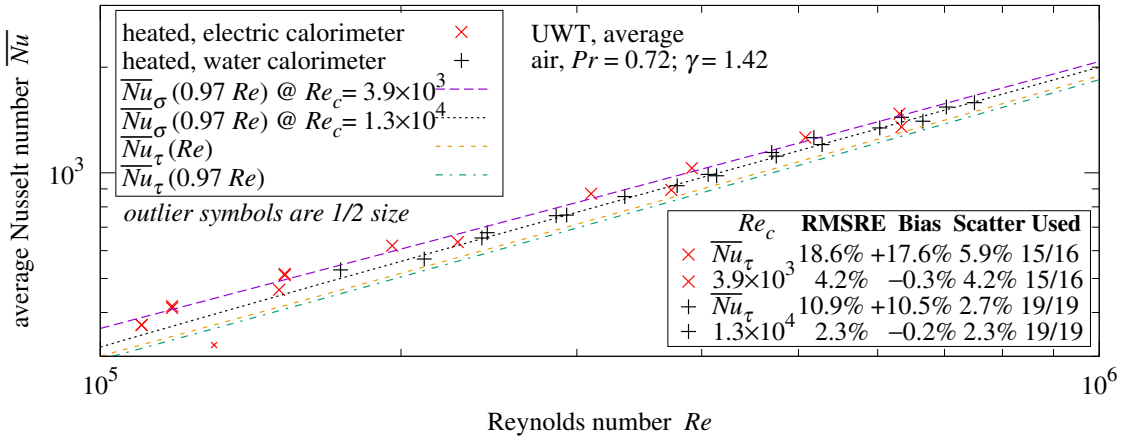

Figure 36. UWT average convection in air [18].

16.13. Triggered Turbulence

In these tests, Žukauskas and Šlančiauskas [18] placed a roughness strip across the leading plate edge, asserting that the downstream flow was all turbulent. But Figure 36 shows that $\overline{Nu_\tau}$ is significantly less than $\overline{Nu_\sigma}$. At $Re > Re_c$, (staged-transition) $\overline{Nu_4} < \overline{Nu_\tau}$. This rules out $\overline{Nu_\tau}$ and $\overline{Nu_4}$ as explanations of Figure 36. While these measurements exceed both laminar and turbulent convective heat transfer, pierced-laminar $\overline{Nu_\sigma}$ has RMSRE less than 4.3%.

16.14. Water

Unlike air, water's viscosity and thermal properties vary significantly with temperature. Grouping by Pr is insufficient to characterize these data sets having three independent variables (T_∞, T_w, and Re). Most are between the $\overline{Nu_\tau}$ traces for heated and cooled plates in Figure 37. The measurements below the "$\overline{Nu_\tau}(0.98\,Re)$ @ $Pr = 2.05$" trace correspond to the group of measurements near the top of Figure 34.

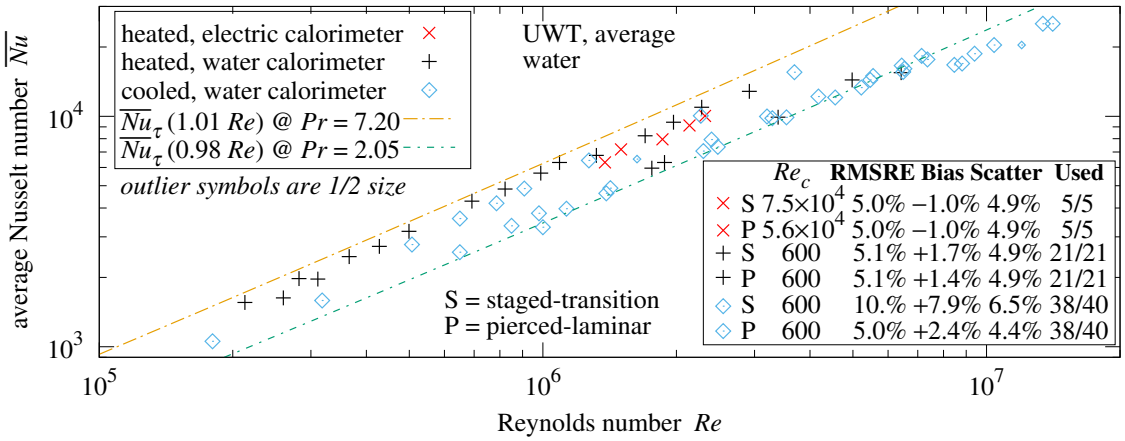

Figure 37. UWT average convection in water [18].

The initial RMSRE calculations exceeded 10%. Figure 38 compares the Žukauskas and Šlančiauskas water property values with formulas from Pramuditya [40] based on Wagner and Pruß [41]. Correcting per these formulas did not significantly reduce the RMSRE values.

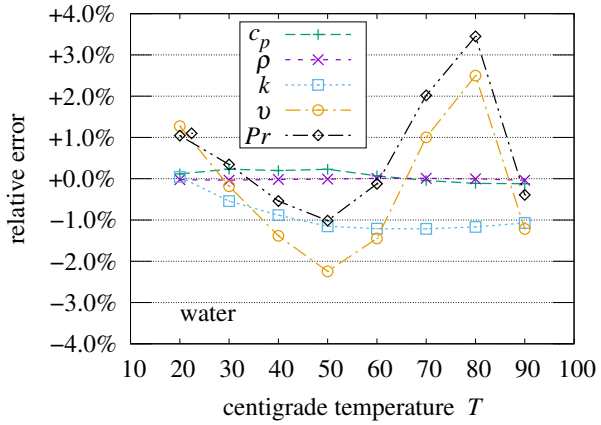

Figure 38. Water property fits [18].

This investigation hypothesizes that the $\overline{Nu}$ measurements had been calculated with a constant $k = 0.54\ \mathrm{W/(m \cdot K)}$ instead of temperature dependent values. Correcting per this hypotheses and water properties, the RMSRE values for pierced-laminar $\overline{Nu_\sigma}$ are 5.1% or less.

- UHF convection is staged-transition $\overline{Nu_4}$ with $Pr = Pr_\infty$.
- UWT convection is pierced-laminar $\overline{Nu_\sigma}$ with $Pr = Pr_w^{1/4} Pr_\infty^{3/4}$.
- Triggered turbulence leading a smooth plate can be modeled as a smooth plate with a small Re_c.

16.15. Transformer Oil

There are multiple sources for the viscosity and thermal properties of air and water; the only source for the transformer oil used in these experiments is a 10-row table (30 °C–120 °C) in the appendix of Žukauskas and Šlančiauskas [18]. The data-set temperatures span 18°C − 90°C. Thus, there is no information about the oil's behavior between 18°C and 30°C, where the slopes of the ν and Pr curves are changing most rapidly. Dynamic viscosity was fit by $\mu = 91.877 \times 10^{-6} \exp(587/[T + 86.45])$. Having less variation, ρ, k, and specific heat (at constant pressure) c_p were modeled by linear ramps. Figure 39 shows the curves hewing to Žukauskas and Šlančiauskas [18] within ±0.7%. Figure 40a,b plot the table values and this investigation's hypothesized $Pr(T)$ and $\nu(T)$ curves at 10 °C–120 °C.

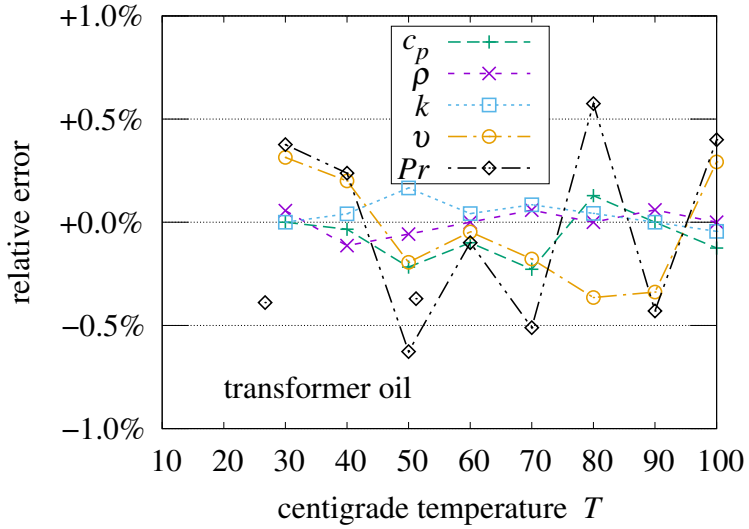

Figure 39. Transformer oil property fits [18].

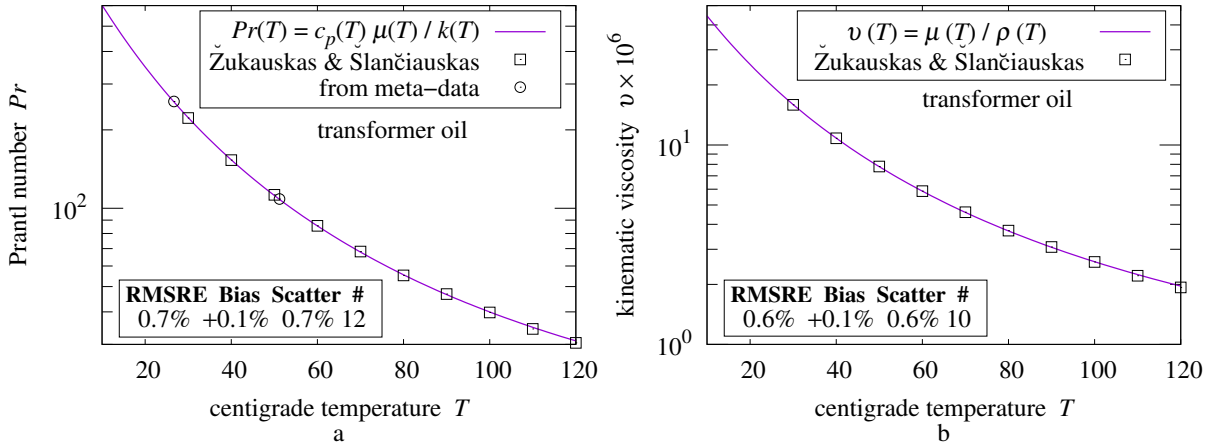

Figure 40. (**a**) Transformer oil Pr [18]; (**b**) Transformer oil ν [18].

Žukauskas and Šlančiauskas [18] apparently calculated transformer oil $\overline{Nu}$ with a constant $k(10\ ^\circ\mathrm{C}) = 0.126\ \mathrm{W/(m \cdot K)}$ instead of temperature dependent values. As with the water measurements, this is corrected in this investigation's plots and RMSRE calculations. Figure 41 plots the transformer oil measurements, which are nearly bounded by pierced-laminar $\overline{Nu_\sigma}$ traces for heated and cooled plates.

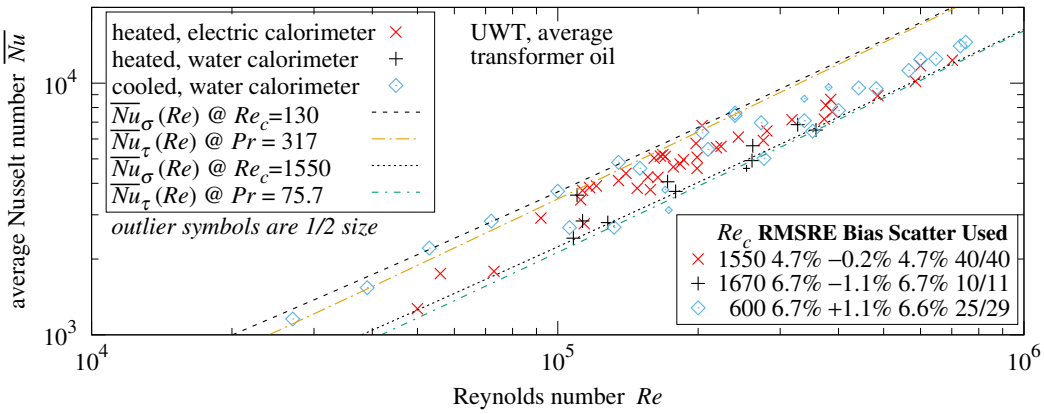

Figure 41. UWT average convection in oil [18].

Relative to pierced-laminar $\overline{Nu_\sigma}$ Formula (92), the heating electric calorimeter data-set of 40 measurements had 4.7% RMSRE. Excluding 1 negative outlier from 11 points, the heating water calorimeter set had 6.7% RMSRE. Excluding 2 positive and 2 negative outliers from 29 points, the cooling water calorimeter set also had 6.7% RMSRE.

Having only an incomplete source of transformer oil properties creates additional uncertainty for the transformer oil convection measurements.

- Relative to pierced-laminar $\overline{Nu_\sigma}$ Formula (92), the Žukauskas and Šlančiauskas [18] UWT data sets for air, water, and transformer oil have RMSRE values between 2.3% and 6.7%.

17. Results

All of the present work formulas which were tested are listed here with their prerequisites. Table 11 lists the top-level formulas tested by one or more data-sets.

Table 11. Top-level formula coverage.

Measured	Plate	Rough $Pr < 1$	Smooth $Pr < 1$	Smooth $Pr > 1$
Average friction		(30) $\overline{f_\tau}$, (91) $\overline{f_\sigma}$		
Local friction		(43) f_ρ , (84) f_ω	(46) f_τ	(46) f_τ
Average convection	UWT	(47) $\overline{Nu_\rho}$, (81) $\overline{Nu_\iota}$	(92) $\overline{Nu_\sigma}$	(92) $\overline{Nu_\sigma}$
Local convection	UWT	(97) Nu_σ		
Local convection	UHF	(95) Nu_4	(95) Nu_4	

The average skin-friction coefficient of steady flow along a smooth, flat surface is:

$$f_\sigma = \frac{\mathrm{d}[Re_x - Re_0]\,\overline{f_\sigma}(Re_x, \sqrt{2}\,Re_c)}{\mathrm{d}Re_x}$$

$$\overline{f_\sigma} = \left\| \overline{f_\lambda}(Re),\ \overline{f_\tau}(Re) - \frac{Re_\gamma}{Re}\,\overline{f_\tau}(Re_\gamma) \right\|_{\sqrt{2}} \qquad Re_\gamma = \left\| Re,\ \frac{Re_c}{\sqrt[4]{2}} \right\|_{-4\sqrt{2}}$$

$$\overline{f_\lambda}(Re) = \frac{1.328}{\sqrt{Re} + \sqrt{Re_0}} \qquad \overline{f_\tau}(Re) = \frac{\sqrt[3]{2}/3}{\left[\mathrm{W}_0\left(Re/\sqrt{3}\right) - 1\right]^2}$$

The local and average Nusselt numbers from a smooth, flat, isothermal plate are:

$$Nu_\sigma = Re_x\,\frac{\mathrm{d}\overline{Nu_\sigma}(Re_x, \sqrt{\gamma}\,Re_c)}{\mathrm{d}Re_x}$$

$$\overline{Nu_\sigma} = \left\| \overline{Nu_\lambda}(Re), \overline{Nu_\tau}(Re) - \overline{Nu_\tau}\left(\|Re, \sqrt{\gamma}\,Re_c\|_{-8/\gamma}\right) \right\|_\gamma$$

$$\gamma = 1 + \exp_2\left(-Pr^{-\sqrt{1/2}}\right) \qquad \exp_2(\varphi) \equiv 2^\varphi$$

$$\overline{Nu_\tau}(Re) = \frac{Nu_0\,Re\,\overline{f_\tau}(Re)}{\sqrt{3}}\,\sqrt{\frac{Pr/\sqrt{162}+1}{\sqrt{162}\,Pr\,\overline{f_\tau}(Re)+1}}\,\sqrt[3]{\frac{Pr/\Xi}{\|1, 1/Pr\|_3}}$$

$$\overline{Nu_\lambda}(Re) = \frac{0.664\,Re\,Pr^{1/3}}{\sqrt{Re} + \sqrt{Re_0}} \qquad Nu_0 = \frac{2^4}{\pi^2\,\sqrt[4]{2}} \qquad \Xi = \left\| 1,\ \frac{0.5}{Pr} \right\|_{\sqrt{1/3}}$$

$Pr = Pr_w^{1/4} Pr_\infty^{3/4}$; Pr_w is at plate temperature; Pr_∞ is at free stream temperature. For smooth, flat, uniform-heat-flux plates, $Pr = Pr_\infty$ and:

$$Nu_4 = Re_x\,\frac{\mathrm{d}\overline{Nu_4}(Re_x, \sqrt{\gamma}\,Re_c)}{\mathrm{d}Re_x}$$

$$\overline{Nu_4} = \left\| \overline{Nu_\lambda}(Re_4),\ \overline{Nu_\tau}(Re) - \overline{Nu_\tau}(Re_4) \right\|_1 \qquad Re_4 = \|Re, \sqrt{2}\,Re_c\|_{-4}$$

Algorithms were presented to find ε, L_P, and Ω from an elevation grid of a square portion of the rough surface. A plate surface is isotropic, periodic roughness when its $L/L_P \gg 1$.

Turbulent momentum thickness $\delta_{2\tau} = \varepsilon$ at Re_τ; laminar momentum thickness $\delta_{2\lambda} = \varepsilon$ at Re_λ.

$$Re_\tau = \frac{\sqrt{3}\,L}{3^3\,\varepsilon}\,\exp\frac{L_P}{3^3\,\varepsilon} \qquad Re_\lambda = \left[\frac{0.664}{\varepsilon}\right]^2 L_P\,L$$

- An isotropic, periodic roughness with $Re_\tau > L/\sqrt{\varepsilon\,L_P}$ behaves as a smooth surface with $Re_c = L/\sqrt{\varepsilon\,L_P}$ when $Re < Re_\lambda$.
- When $Re > Re_\lambda$ and $\Omega > 1/2$, flow along the entire surface will be rough.

The average skin-friction coefficient $\overline{f_\rho}$ and average Nusselt number $\overline{Nu_\rho}$ of rough flow are:

$$\overline{f_\rho} = \frac{1}{3\,\ln^2(L/\varepsilon)} \qquad \overline{Nu_\rho} = \frac{Re\,Pr_\infty^{1/3}}{6\,\ln^2(L/\varepsilon)} \qquad \frac{L}{\varepsilon} \gg 1$$

Plateau islands roughness:

$$\overline{Nu_\iota} = \overline{Nu_I}(Re) + \overline{Nu_\rho}(\|Re, Re_I\|_{-4}) - \overline{Nu_I}(\|Re, Re_I\|_{-4})$$
$$\overline{Nu_I} = \left\{1 - \Omega + \left\|\frac{\Omega}{2}, \frac{2\,\varepsilon\,[4\,L^*]}{L_P^2}\right\|_2\right\}\frac{L}{L_P}\,\overline{Nu_\tau}\left(\frac{Re\,L_P}{L}\right)$$
$$Re_I = \frac{3^3\,\varepsilon^2\,L^2}{L^*\,L_P^3}\,\ln\frac{3^3\,\varepsilon^2\,L^2}{\sqrt{3}\,L^*\,L_P^3} \qquad \frac{[4\,L^*]^2}{L_P^2} > \frac{1}{2}$$

Plateau wells roughness:

$$f_\omega = f_W(Re) + \left[Re_\omega/Re\right]\left\{f_\beta(Re_\omega) - f_W(Re_\omega)\right\} \qquad Re_\omega = \|Re, Re_W\|_{-4}$$
$$f_W = \left\|1, 2\,\pi\,\varepsilon\,[4\,L^*]/L_P^2\right\|_{\sqrt[4]{8}} f_\tau(Re)$$
$$f_\beta = \Omega\,\overline{f_\rho}(L/\varepsilon) + [1-\Omega]\,f_\tau(Re)$$
$$Re_W = \frac{3^3\,\varepsilon^2\,L^2}{2^3\,L^*\,L_P^3}\,\ln\frac{3^3\,\varepsilon^2\,L^2}{2^3\,\sqrt{3}\,L^*\,L_P^3} \qquad \frac{[4\,L^*]^2}{L_P^2} < \frac{1}{2}$$

Conformance

Tables 12 and 13 summarize the present theory's conformance with 456 measurements in 32 data-sets from one book, six peer-reviewed studies, and the present apparatuses.

$L/\varepsilon = \infty$ signifies a smooth plate. The "Heat" column in Table 13 contains "UHF", "UWT" or "UWT−" indicating a heated UHF plate, a heated UWT plate, or a cooled UWT plate, respectively.

- Relative to the present work formulas, the 32 data-set RMSRE values span 0.75% through 8.2%.
- Only 4 of the 32 data-sets have an RMSRE exceeding 6%.
- Prior work formulas have a smaller RMSRE on only four of the data-sets.

Table 12. Friction measurements versus present theory.

Source	L/ε	Formula	Pr_∞	RMSRE	Bias	Scatter	Used
[11,22,23] Churchill [1]	∞	(30) $\overline{f_\tau}$	0.71	0.75%	+0.13%	0.74%	9/9
[11,22,23] Churchill [1]	∞	(46) f_τ	0.71	1.9%	+1.2%	1.4%	11/11
[18] Žukauskas and Šlančiauskas	∞	(46) f_τ	55.2	2.5%	+0.6%	2.4%	5/5
[18] Žukauskas and Šlančiauskas	∞	(46) f_τ	5.42	5.2%	+4.9%	1.8%	8/8
[18] Žukauskas and Šlančiauskas	∞	(46) f_τ	2.78	3.3%	+1.0%	3.1%	8/8
[18] Žukauskas and Šlančiauskas	∞	(46) f_τ	0.71	4.4%	−1.4%	4.2%	9/9
[20,21] Gebers	∞	(91) $\overline{f_\sigma}$		2.8%	−0.2%	2.8%	33/33
[8] Pimenta et al.	1.5×10^3	(43) f_ρ	0.71	4.5%	−3.0%	3.3%	19/19
[13] Bergstrom et al.	∞	(46) f_τ	0.71	4.8%	−4.4%	1.7%	4/4
[13] Bergstrom et al. —mesh	1600–3000	(43) f_ρ	0.71	3.3%	−2.0%	2.6%	12/12
[13] Bergstrom et al. —wells	1200–1500	(84) f_ω	0.71	4.4%	+0.9%	4.3%	12/12

[1] Churchill [11] extracted its measurements from Smith and Walker [22] and Spalding and Chi [23].

Table 13. Convection measurements versus present theory.

Source	L/ε	Heat	Formula	Pr_∞	RMSRE	Bias	Scatter	Used
[24] Kestin et al.	∞	UWT	(97) Nu_σ	0.7	3.8%	−1.0%	3.7%	7/7
[24] Kestin et al.	∞	UWT	(97) Nu_σ	0.7	8.2%	+1.5%	8.0%	13/13
[25] Reynolds et al.	∞	UWT	(97) Nu_σ	0.71	6.4%	+2.3%	6.0%	22/22
[18] Žukauskas and Šlančiauskas	∞	UHF	(95) Nu_4	0.71	1.1%	−0.2%	1.1%	8/10
[18] Žukauskas and Šlančiauskas	∞	UHF	(95) Nu_4	0.71	2.5%	−1.0%	2.3%	8/10
[18] Žukauskas and Šlančiauskas	∞	UHF	(95) Nu_4	0.71	2.2%	−1.2%	1.9%	8/10
[18] Žukauskas and Šlančiauskas	∞	UHF	(95) Nu_4	6.57	3.7%	−1.1%	3.5%	19/19
[18] Žukauskas and Šlančiauskas	∞	UHF	(95) Nu_4	6.57	3.1%	−0.9%	3.0%	15/15
[18] Žukauskas and Šlančiauskas	∞	UHF	(95) Nu_4	108	2.4%	−0.8%	2.3%	17/17
[18] Žukauskas and Šlančiauskas	∞	UHF	(95) Nu_4	257	4.3%	+0.2%	4.3%	17/17
[18] Žukauskas and Šlančiauskas	∞	UWT	(92) $\overline{Nu_\sigma}$	0.71	4.2%	−0.3%	2.3%	15/16
[18] Žukauskas and Šlančiauskas	∞	UWT	(92) $\overline{Nu_\sigma}$	0.71	2.3%	−0.2%	2.3%	19/19
[18] Žukauskas and Šlančiauskas	∞	UWT	(92) $\overline{Nu_\sigma}$	5.8–7.1	5.0%	−1.0%	4.9%	5/5
[18] Žukauskas and Šlančiauskas	∞	UWT	(92) $\overline{Nu_\sigma}$	2.9–7.2	5.1%	+1.4%	4.9%	21/21
[18] Žukauskas and Šlančiauskas	∞	UWT−	(92) $\overline{Nu_\sigma}$	2.0–5.8	5.0%	+2.4%	4.4%	38/40
[18] Žukauskas and Šlančiauskas	∞	UWT	(92) $\overline{Nu_\sigma}$	75–246	4.7%	−0.2%	4.7%	40/40
[18] Žukauskas and Šlančiauskas	∞	UWT	(92) $\overline{Nu_\sigma}$	80–205	6.7%	−1.1%	6.7%	10/11
[18] Žukauskas and Šlančiauskas	∞	UWT−	(92) $\overline{Nu_\sigma}$	92–317	6.7%	+1.1%	6.6%	25/29
Present apparatus—3 mm bi-level	102	UWT	(47) $\overline{Nu_\rho}$	0.71	1.8%	−0.5%	1.7%	8/13
Present apparatus—3 mm bi-level	102	UWT	(81) $\overline{Nu_\iota}$	0.71	1.8%	−0.5%	1.7%	11/13
Present apparatus—1 mm bi-level	295	UWT	(79) $\overline{Nu_I}$	0.71	1.5%	−0.5%	1.4%	9/14

18. Discussion

Rather than trying to tease rough flow from a nearly smooth surface, this investigation started with an analysis of roughness deep enough to disrupt boundary layer flow.

18.1. Skin-Friction

With boundary layers disrupted by self-similar roughness, the flow's roughness velocity u_ρ was used to derive the average skin-friction coefficient $\overline{f_\rho}$. Deriving the roughness Reynolds number Re_ε led to a formula for average turbulent skin-friction $\overline{f_\tau}$ with unprecedented 0.75% RMSRE fidelity to the Smith and Walker [22], and Spalding and Chi [23] measurements (via Churchill [11]).

Section 9 and subsequent comparisons with measurements established that transforms between local and average friction differ for continuous versus disrupted boundary layers.

Thus, these transforms are not valid for combined flows over plateau roughnesses which shed rough and turbulent flow simultaneously.

18.2. Laminar Friction

$\overline{f_\lambda}$ Formula (39) differs from the traditional $1.328/\sqrt{Re}$ formula because Formula (39) is valid for all $Re \geq 0$, with $\overline{f_\lambda}(0) = 1.328/\sqrt{Re_0} \approx 0.0542$. This removes the need to treat the leading edge differently from the rest of the plate in many cases.

Measuring smooth plate $\overline{f_\lambda}$ at $Re = 1000$ in a viscous liquid, then solving Formula (39) for Re_0 would refine the Re_0 value.

18.3. Forced Convection

Combining Formula (58) with rough friction $\overline{f_\rho}$ Formula (27) results in the formula $\overline{Nu_\rho} = Re\, Pr^{1/3}/[6 \ln^2(L/\varepsilon)]$, which is identical to rough convection Formula (47).

Formula (58) is the original (1933) form of the Reynolds–Colburn analogy. Lienhard [29] demonstrates that the analogy can fail for turbulent flows. In particular, the Pr exponent should be 0.6 in gasses.

Formula (47) using $Pr^{1/3}$ matches rough convection from the $\varepsilon = 3$ mm apparatus spanning $4000 < Re < 50,000$ within its estimated measurement uncertainties (plotted in Appendix A). With $Pr = 0.71$ (air), $Pr^{0.6} \approx 0.814$ is 9% smaller than $Pr^{1/3} \approx 0.892$; this mismatch exceeds some of those estimated measurement uncertainties.

Thus, the Pr dependence of rough and turbulent convection differ.

None of the present or cited experiments measured fluids with $0 < Pr < 0.7$. Forced convection heat transfer measurements in this range are needed.

18.4. Onset of Rough Flow

The present theory predicts that an isotropic, periodic rough plate with $\Omega > 1/2$ switches from all laminar to all rough flow as $Re > Re_\lambda$. The prior and present work measurements from rough plates were taken at $Re > Re_\lambda$; most were at $Re \gg Re_\lambda$. Measurements at Re values closely bracketing Re_λ are needed to test Re_λ Formula (66).

18.5. Pierced-Laminar

Section 15 presented indirect evidence of duck tape generating pierced-laminar convection exceeding both laminar and turbulent convection.

To definitively test pierced-laminar flow from roughness, convection or skin-friction measurements at Re values near Re_c are needed from a surface having $Re_c = L/\sqrt{\varepsilon L_P} < Re_\tau < Re_\lambda$.

18.6. Expected Measurement Uncertainty

The present work made several claims based on measurements being within the present apparatus's expected measurement uncertainties. Attributing discrepancies to parameters was robust because each parameter affected different Re ranges:

- The pierced-laminar convection of duck tape-covered sides affected both plates at $Re > 1000$.
- Blending plateau islands convection using the ℓ^{-4}-norm affected plates only near their Re_I values of 6178 and 55,566, respectively.
- The $Pr^{1/3}$ factor in rough convection affected the $\varepsilon = 3$ mm plate at $Re_\lambda < Re < Re_I$.

18.7. Chung, Hutchins, Schultz, and Flack

Of the studies cited by Chung et al. [15], some plates would qualify as having isotropic, periodic roughness; testing them against the present theory requires isobaric flow, roughness height maps (or enough dimensional information to create them), free-stream Re, and skin-friction coefficient or convection heat transfer measurements. Although some of the studies are likely to have this information, few, if any, report all of these details in the published articles.

19. Conclusions

- The pipe-plate analogy fails for roughness because rough skin-friction coefficients can be less than smooth regime coefficients for external plates, but not inside pipes.
- While understanding the nature of the flow shed by roughness is of theoretical interest, it is not needed for determining the skin-friction coefficient from a rough surface in an isobaric flow. The present theory is independent of turbulence theory.
- Modeling the flow along a rough plate as repeated boundary layer disruptions leads to exact formulas calculating the skin-friction coefficient and Nusselt number of a flat plate given its characteristic length, RMS height-of-roughness, isotropic spatial period, openness, Reynolds number, and the fluid's Prandtl numbers at free-stream and plate temperatures.
- These new equations offer improved accuracy or improved range relative to prior works. They were tested with 456 heat transfer and friction measurements in 32 data-sets from one book, six peer-reviewed studies, and the present apparatus.
  - Relative to the present work formulas, the 32 data-set's RMSRE values span 0.75% through 8.2%.
  - Only 4 of the 32 data-sets have an RMSRE exceeding 6%.
  - Prior work formulas have a smaller RMSRE on only four of the data-sets.

Supplementary Materials: The following supporting information can be downloaded at: https://www.mdpi.com/article/10.3390/thermo3040040/s1: a zip archive of the measurements from this investigation and prior works which were compared with the present theory.

Funding: This research received no external funding.

Informed Consent Statement: Not applicable.

Data Availability Statement: Data are contained within the supplementary materials.

Acknowledgments: Thanks to John Cox (1957–2022) and Doug Ruuska for machining the bi-level plate. Thanks to Martin Jaffer for his critiques and insights. Thanks to the anonymous reviewers for their useful suggestions.

Conflicts of Interest: The author declares no conflicts of interest.

Abbreviations

The following abbreviations are used in this manuscript:

ARM	computer processor architecture
LM35C	temperature sensor integrated circuit
MIC-6 Al	an aluminum alloy
MPXH6115A6U	air pressure sensor integrated circuit
PIR	polyisocyanurate foam
PLL	phase-locked loop, synchronization control method
PL	Bergstrom et al. [13] perforated sheet large
PM	Bergstrom et al. [13] perforated sheet medium
PS	Bergstrom et al. [13] perforated sheet small
RAM	random access memory
RH	relative humidity (%)
RMS	root-mean-squared
RMSRE	root-mean-squared relative error (%)
RSS	root-sum-squared
SGL	Bergstrom et al. [13] sandpaper grit large
SGML	Bergstrom et al. [13] sandpaper grit medium-large
SGM	Bergstrom et al. [13] sandpaper grit medium
SGS	Bergstrom et al. [13] sandpaper grit small

SM	Bergstrom et al. [13] smooth plate
STM	STMicroelectronics, integrated circuit manufacturer
UHF	uniform heat flux (W/m^2)
USB	Universal Serial Bus
UWT	uniform wall temperature, isothermal (K)
WML	Bergstrom et al. [13] wire mesh large
WMM	Bergstrom et al. [13] wire mesh medium
WMS	Bergstrom et al. [13] wire mesh small
XPS	extruded polystyrene foam

Nomenclature

Latin Letters

A	surface area (m^2)
$C_f/2, \overline{C_f}/2$	local, average skin-friction coefficient Mills-Hang [9] and Pimenta et al. [8]
$C_m/2$	average skin-friction coefficient Churchill [11]
c_p	fluid specific heat at constant pressure ($J/(kg \cdot K)$)
$c_f, \overline{c_f}$	local, average skin-friction coefficient Prandtl-Schlichting [3]
$f_c, \overline{f_c}$	local, average skin-friction coefficient present work
$G(t, w)$	Gray-code self-similar ramp-permutation
$h, \overline{h}$	local, average convective surface conductance ($W/(m^2 \cdot K)$)
j_P	period index, the index of largest X_j or $X_{j,k}$
k	fluid thermal conductivity ($W/(m \cdot K)$)a
k_S	sand-roughness (m)
L	plate characteristic length (m)
L_P	roughness spatial period (m)
L^*	ratio of plateau convex region area to its perimeter (m)
$Nu, \overline{Nu}$	local, average Nusselt number (convection)
Pr	Prandtl number of fluid
q	positive integer $= \log_2 w$
Re	Reynolds number of flow parallel to the plate
Re_c	purely laminar upper-bound
Re_I, Re_W	Re_x rough-to-turbulent flow threshold
Re_λ, Re_τ	laminar, turbulent Re upper-bound
Re_ε, Re_k	roughness, sand-roughness Reynolds number
Re_x	local Reynolds number $= x\,Re/L$
Re_0	Re_x integration lower bound
Re_u	Re_x of leading unheated band
$S_{j,k}$	matrix of elevations
t	integer
u, u_ρ	bulk fluid, friction velocity (m/s)
$W(t, w)$	wiggliest integer self-similar ramp-permutation
W_0	principal branch of the Lambert W function
w	integer power of two $= 2^q$
$X_j, X_{j,k}$	discrete Fourier transform coefficient
x, x_u	distance, unheated distance from leading edge of plate (m)
$Y(t, w)$	integer self-similar ramp-permutation
Z	roughness random variable (m)
$z(x), z(x, y)$	roughness elevation function (m)
$\bar{z}$	mean elevation of roughness function (m)

Greek Symbols

δ_2	momentum thickness of boundary layer flow (m)
$\delta_{2\lambda}, \delta_{2\tau}$	laminar, turbulent flow momentum thickness (m)
ϵ, ε	profile, surface RMS height-of-roughness (m)
γ, γ'	exponent p of the ℓ^p-norm
ν	fluid kinematic viscosity (m^2/s)
Ω	ratio of non-plateau area to cell area (m^2/m^2)
ρ	fluid density (kg/m^3)
τ, τ_2	fluid shearing stress (N/m^2)
ς	peak elevation of roughness (m)
φ, ϑ	mathematical scalar variables

Subscripts

λ	Laminar flow
τ	Turbulent flow
ρ	Rough flow
σ	Pierced-laminar flow (smooth UWT plate)
4	Staged-transition (smooth UHF plate)
I	Platform islands
ι	Platform islands
β	Platform wells
W	Platform wells
ω	Platform wells

Appendix A. Apparatus and Measurement Methodology

This goal of the present apparatus was to measure forced convection heat transfer from a precisely rough plate over the widest practical span of airflow velocities.

Although more complicated to analyze, the plate was suspended, not embedded, in the wind-tunnel. The measurements from prior investigations that embedded the plate in a wind-tunnel wall were largely incompatible with the present theory because their flows were not isobaric.

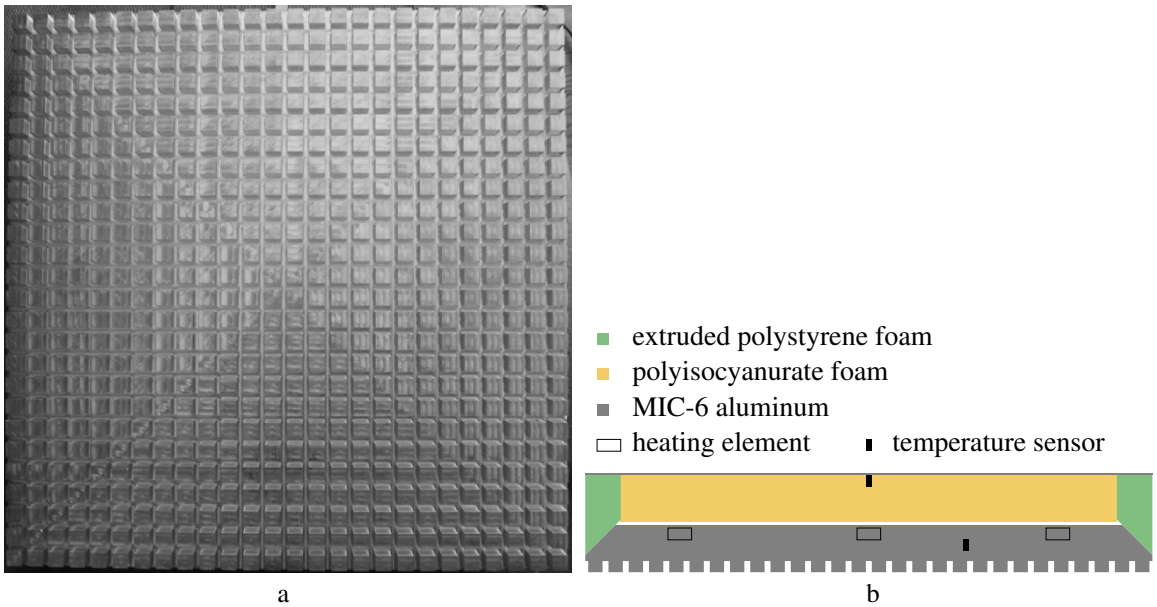

Figure A1. (**a**) Rough surface of plate; (**b**) plate assembly cross-section.

Appendix A.1. The Plate

Figure A1a shows the rough surface of the test plate; it was milled from a slab of MIC-6 aluminum (Al) to have (676 of) square 8.33 mm × 8.33 mm × 6 mm posts spaced on 11.7 mm centers over the 30.5 cm × 30.5 cm plate. The area of the top of each post was 0.694 cm^2,

which was 50.4% of its 1.38 cm^2 cell. The RMS height-of-roughness $\varepsilon = 3.00$ mm. Openness $\Omega \approx 49.6\%$. Embedded in the plate are 9 electronic resistors as heating elements and a Texas Instruments LM35 Precision Centigrade Temperature Sensor. 2.54 cm of thermal insulating foam separates the back of the plate from a 0.32 mm thick sheet of aluminum with an LM35 temperature sensor at its center. Figure A1b is a cross-section illustration of the plate assembly.

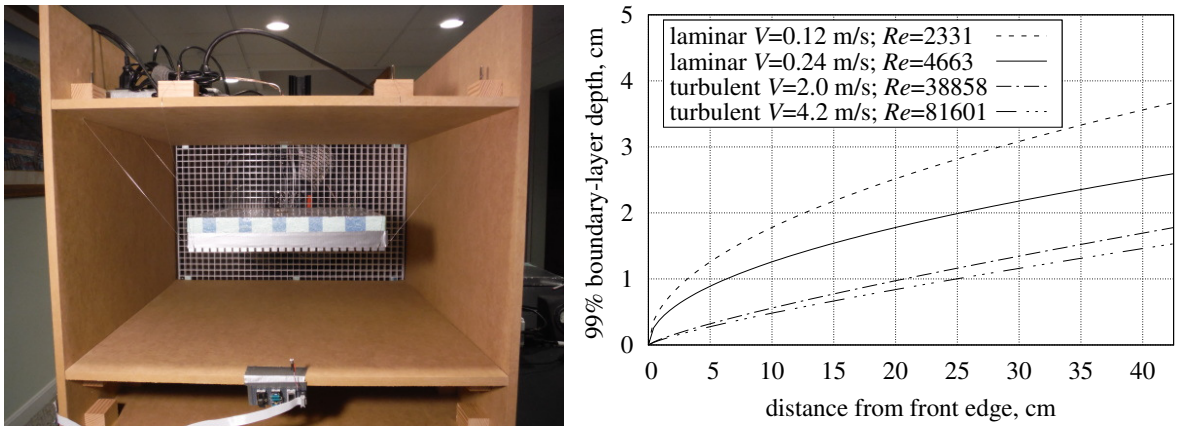

a b

Figure A2. (**a**) $\varepsilon = 3$ mm plate in wind-tunnel; (**b**) wind-tunnel boundary layers.

Appendix A.2. Wind Tunnel

The fan pulls air from the test chamber's open intake through the test chamber. The fan blows directly into a diffuser made of folded plastic mesh to disrupt vortexes generated by the fan. In a sufficiently large room, the disrupted vortexes dissipate before being drawn into the open intake.

To guarantee isobaric (no pressure drop) flow, the wind-tunnel must be sufficiently large that its test chamber and plate assembly boundary layers do not interact at fan-capable airspeeds.

The wind-tunnel test chamber in Figure A2a has a 61 cm × 35.6 cm cross-section and a 61 cm depth. This allows the plate assembly to be centered in the wind-tunnel with 15 cm of space on all sides. The fan pulling air through the test chamber produces a maximum airspeed of 4.65 m/s ($Re \approx 9.2 \times 10^4$ along the 30.5 cm square plate). Its minimum nonzero airspeed is 0.12 m/s ($Re \approx 2300$).

Test chamber laminar and turbulent 99% boundary layer thicknesses (Schlichting [7]) are:

$$\delta_\lambda = 4.92\sqrt{\frac{x\nu}{u}} \qquad \delta_\tau = 0.37\,x^{4/5}\left[\frac{\nu}{u}\right]^{1/5} \tag{A1}$$

Figure A2b shows that the 15 cm clearance between the plate and the test chamber walls is sufficient to prevent their boundary layers from interacting at airspeeds within the fan's capabilities.

The plate assembly is suspended from six lengths of 0.38 mm-diameter steel piano wire terminated at twelve zither tuning pins in wooden blocks fastened to the exterior of the test chamber. The plate is suspended face-down to minimize the natural convection from the test-surface. With the plate assembly in the test chamber, the airspeed increases in proportion to the reduction of test chamber aperture A_e by the plate's cross-sectional area $A_\times$:

$$\frac{u_\times}{u} = \frac{A_e}{A_e - A_\times} \approx 107.6\% \tag{A2}$$

Appendix A.3. Automation

Data capture and control of convection experiments are performed by an "STM32F3 Discovery 32-Bit ARM M4 72MHz" development board. The program written for the STM32F3 captures readings and writes them to the microprocessor's non-volatile RAM, controls the plate heating, servos the fan speed, and later uploads its data to a computer through a USB cable.

Once per second during an experiment, the program calibrates and reads each on-chip 12 bit analog-to-digital converter 16 times, summing the sixteen 12 bit readings to create a 16 bit reading per converter.

Rotations of the fan are sensed when a fan blade interrupts an infrared beam. The microprocessor controls a solid-state relay (supplying power to the fan) to maintain a fan rotation rate, ω, which is dialed into switches. At $\omega \leq 210$ r/min, the microprocessor pulses power to the fan to phase-lock the beam interruption signal to an internal clock. At $\omega > 210$ r/min, the microprocessor servos the duty cycle of a 7.5 Hz square-wave gating power to the fan. This system operates at 32 r/min $< \omega <$ 1400 r/min.

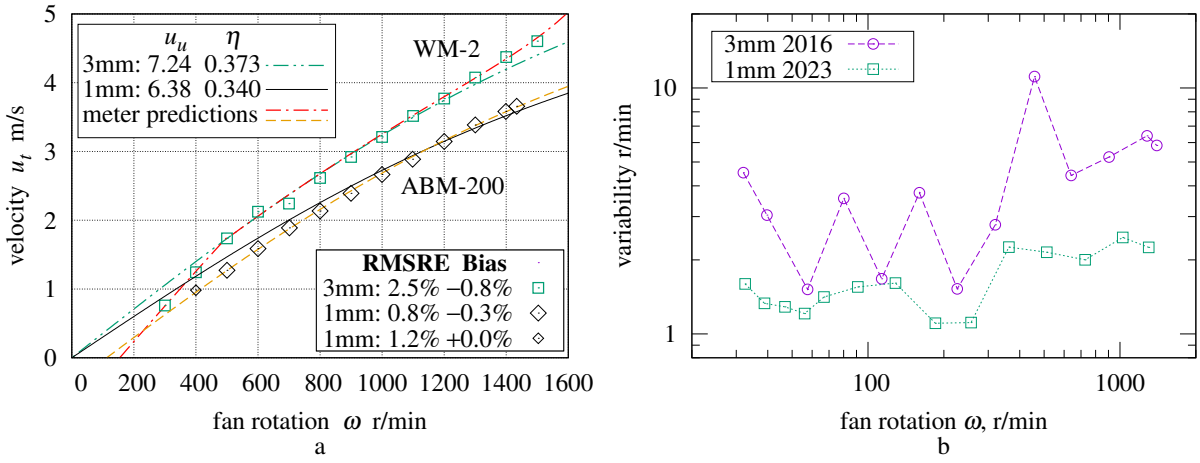

Figure A3. (**a**) Airspeed versus fan speed; (**b**) Fan PLL variability.

Appendix A.4. Calibration

The correspondence between fan rotation rate ω and test chamber airspeed u was determined using an "Ambient Weather WM-2", which specifies an accuracy of $\pm 3\%$ of reading. After 2017 an "ABM-200 Airflow & Environmental Meter" specifying an accuracy of $\pm 0.5\%$ of reading between 2.2 m/s and 62.5 m/s, was used.

The "UtiliTech 20 inch 3-Speed High Velocity Floor Fan" has three blades with maximum radius $r = 0.254$ m. Its characteristic length is its hydraulic-diameter, $D_H = 0.550$ m. The velocity of the blade tips is $2\,\pi\,r\,\omega/60$, where ω is the number of rotations per minute. The Reynolds number of the fan is:

$$Re_f = \frac{2\,\pi\,r\,D_H\,\omega/60}{3\,\nu} \tag{A3}$$

The 3 blade tips trace the whole circumference in only 1/3 of a rotation, hence the 3 in the denominator.

Faster fan rotation ω yields diminishing increases of test-chamber airspeed u_t, suggesting Formula (A4), where u_u is the limiting velocity for arbitrarily fast rotation, and coefficient η converts fan Re_f to test-chamber Re_t. Figure A3a gives the parameters and measurements at 300 r/min $\leq \omega \leq$ 1500 r/min. The "3 mm" points are the WM-2 measurements of the 3 mm plate in the original wind-tunnel; The "1 mm" points are the ABM-200 measurements of the 1 mm plate in the tunnel with a new diffuser and fan cowling.

$$Re_t = \|\eta\,Re_f,\ D_H\,u_u/\nu\|_{-2} \qquad u_t = \|\pi\,\eta\,r\,\omega/90,\ u_u\|_{-2} \tag{A4}$$

Airspeeds slower than 2 m/s should be nearly proportional to ω. Both anemometers show evidence of dry (bearing) friction in Figure A3a. The ABM-200 "meter predictions" trace plots $1.125\,u_t - 0.381$; the WM-2 "meter predictions" trace plots $1.477\,u_t - 0.81$ when $u_t < 1.725$ and u_t otherwise. A mistake in the 2016 measurement software under-counted fan rotations at $\omega > 1200$ r/min. This is compensated by replacing ω in Formulas (A3) and (A4) with $[\omega^{-6} - 1750^{-6}]^{-1/6}$ in the WM-2 "meter predictions". The RMSRE and Bias are relative to the "meter predictions". The second "1 mm" row includes the point at 400 r/min.

Figure A3b shows the fan speed variability for each downward-facing experiment; these are used by the measurement uncertainty calculations. The differences reflect improvements in the fan-control software written by the author (28 September 2023).

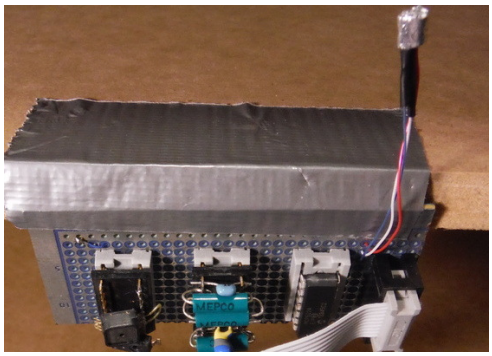

Figure A4. Ambient sensors.

Appendix A.5. Ambient Sensing

Figure A4 shows the ambient sensor board which was at the lower edge of the test chamber in Figure A2a. It measures the pressure, relative humidity (RH), and air temperature at the wind-tunnel intake. Wrapped in aluminum tape to minimize radiative heat transfer, the LM35 temperature sensor projects into the tunnel. To minimize self-heating, the LM35 is powered only while being sampled.

Table A1. Physical parameters.

Symbol	Value			Description
L	0.305 m			length of flow along test-surface
A	0.093 m^2			area of test-surface
ε	3.00 mm	*or*	1.04 mm	RMS height-of-roughness
C_{pt}	4691 J/K	*or*	4274 J/K	plate thermal capacity
D_{Al}	19.4 mm			metal slab thickness
D_{PIR}	25.4 mm			polyisocyanurate (PIR) foam thickness
D_w	19.05 mm			XPS foam wedge height
k_{PIR}	0.0222 W/(m · K)			PIR foam thermal conductivity
k_{XPS}	0.0285 W/(m · K)			XPS foam thermal conductivity
U_I	0.075 W/K			front-to-back insulation thermal conductance
ϵ_{Al}	0.04			test-surface (MIC-6 Al) emissivity
ϵ_{XPS}	0.515			XPS foam emissivity (see text)
ϵ_{dt}	0.89			duck tape emissivity
ϵ_{wt}	0.90			test chamber interior emissivity

Appendix A.6. Physical Parameters

Table A1 lists the static parameters from measurements and specifications.

The effective ϵ_{wt} may differ from the medium-density-fiberboard emissivity given by Rice [42] because the temperatures of the test chamber surfaces may not be uniform.

Through the open intake, the plate also exchanges thermal radiation with objects in the room having different temperatures.

Appendix A.7. Modeling of Parasitic Heat Flows

At low airflow velocities, the sides of the insulation behind the test plate can leak more heat than the test-surface transfers, shrinking to 6% at 1300 r/min. To compensate, expected side heat transfers will be subtracted from the (combined) measured heat flow.

Figure A2a shows duck tape applied to the lower 54% of the plate's side, which corresponds to 50% coverage of the XPS foam wedge. For this partial tape coverage, ϵ_W Formula (A5) is the area proportional mean of the duck tape emissivity and XPS emissivity. Barreira, Almeida, and Simões [43] measured ϵ_{dt} emissivities of 0.86 and 0.89 from two brands of "duck tape"; the larger value is used for the aged tape on the plate sides. As of this writing, published emissivity measurements of XPS foam have not been located.

$$\epsilon_W = 50\%\,\epsilon_{dt} + 50\%\,\epsilon_{\mathrm{XPS}} \tag{A5}$$

Relative to the theory in Jaffer [28], natural convection measurements ($u = 0$) from the plate assembly over the span of inclinations have less than 2.8% RMSRE when calculated with $\epsilon_{\mathrm{XPS}} = 0.515$; the RMSRE increases to either side of 0.515. This value is consistent with natural convection measurements of the plate assembly without tape.

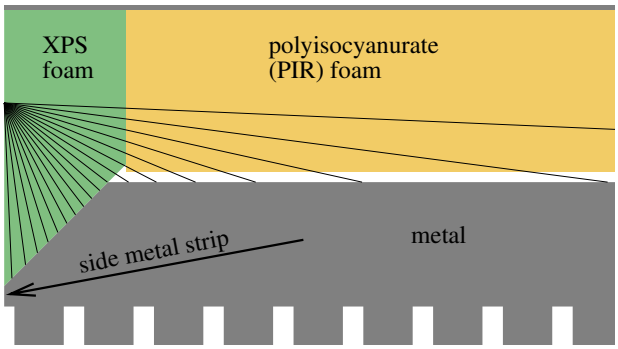

Figure A5. XPS wedge conduction.

The four sides are not isothermal; a 3.5 mm metal strip (see cross-section Figure A5) runs the length of the side; and a D_w-tall wedge of extruded polystyrene foam (XPS) insulation fills the metal slab's 27 mm ($= \sqrt{2}\,D_{\mathrm{Al}}$) 45° chamfer. The local surface conductance $h_W(z)$ at elevation z (from the wedge point) is found by averaging the reciprocal distance to slab metal with respect to angle θ:

$$\begin{aligned} h_W(z) &= \int_0^{\theta_c} \frac{k_{\mathrm{XPS}}}{\sqrt{2}\,z\,\theta_c} \cos\!\left(\theta + \frac{\pi}{4}\right) \mathrm{d}\theta + \int_{\theta_w}^{\theta_W} \frac{k_{\mathrm{PIR}}}{z - D_w} \frac{\cos\theta}{\theta_W - \theta_w}\,\mathrm{d}\theta \\ &= \frac{k_{\mathrm{XPS}}}{\sqrt{2}\,z\,\theta_c}\left[\sin\!\left(\theta_c + \frac{\pi}{4}\right) - \sin\frac{\pi}{4}\right] + \frac{k_{\mathrm{PIR}}}{z - D_w}\left[\frac{\sin\theta_W - \sin\theta_w}{\theta_W - \theta_w}\right] \end{aligned} \tag{A6}$$

$$\theta_c = \arctan\frac{D_w - z}{D_w} \quad \theta_w = \arctan\frac{D_w}{z - D_w} \quad \theta_W = \max\!\left(\theta_w,\, \arctan\frac{L - D_w}{z - D_w}\right)$$

Forced air flows parallel to the long dimension on two sides, but flows into the windward side and away from the leeward side. Air heated by the windward side reduces heat transfer from the test-surface; air heated by the test-surface suppresses heat transfer from the leeward side. Hence, the model excludes windward and leeward forced convection. The total forced convective conductance of the flow-parallel foam wedges is calculated by integrating $h_W(z)$ in series (reciprocal of the sum of reciprocals, which is also the ℓ^{-1}-norm) with the local surface conductance $k\,Nu_\sigma(Re_x)/L$, where $Nu_\sigma(Re_x)$ is the pierced-laminar

convection calculated by applying the $\overline{Nu_\tau} \to Nu_\tau$ transform (57) to the pierced-laminar convection Formula (92):

$$U_W = \int_0^{D_w} \int_0^{L} \left\| h_W(z), \frac{k\, Nu_\sigma(Re_x)}{L} \right\|_{-1} \mathrm{d}x\, \mathrm{d}z \tag{A7}$$

The natural convection flow from the vertical faces is upward, perpendicular to the horizontal forced flow; hence, the forced convection U_W and the natural convective conductance $k\,L\,L'\,\overline{Nu'}/L' = k\,L\,\overline{Nu'}$ combine as the ℓ^2-norm (introduced in Section 13). The resulting mixed convective conductance is in mild competition with the side radiative conductance, $U_R = \epsilon_W\,\epsilon_{wt}\,h_R\,L\,D_w$; they combine as the $\ell^{\sqrt{2}}$-norm:

$$U_S(u) = 2\left\| U_R,\ \|U_W, k\,L\,\overline{Nu'}\|_2 \right\|_{\sqrt{2}} + 2\,\|U_R,\ k\,L\,\overline{Nu'}\|_{\sqrt{2}} \tag{A8}$$

Each of the four side's natural convective conductance is $\overline{Nu'}$ vertical plate Formula (A9) from Jaffer [28], with characteristic length $L' = D_{\mathrm{Al}} + \sqrt{2}\,\varepsilon$, where the metal slab thickness $D_{\mathrm{Al}} \approx 19.4$ mm.

$$\overline{Nu'} = \left\| \frac{Nu'_0}{2},\ \frac{Nu_0'^{4/3}}{8\sqrt[3]{2}} \left[\frac{Ra}{\Xi(Pr)}\right]^{1/3} \right\|_{1/2} \tag{A9}$$

$$\Xi(Pr) = \left\| 1,\ \frac{0.5}{Pr} \right\|_{\sqrt{1/3}} \qquad Nu'_0 = \frac{8^{5/4}}{\pi^2}$$

Appendix A.8. Measurement Methodology

The measurement methodology employed is unusual. Instead of waiting until the plate reaches thermal equilibrium, the plate is heated to 15 K above ambient, heating stops, the fan runs at the designated speed, and convection cools the plate. All of the sensor readings are captured each second during the 102 minute process, Table A2 lists the dynamic physical quantities measured each second. Table A3 lists computed quantities. Both $U_S(u)$ and $\{\epsilon_{\mathrm{Al}}\,\epsilon_{wt}\,h_R\,A\}$ are subtracted from the combined heat flow. The mean of $\overline{h}(u,t)$ over the time interval in which ΔT drops by half (or exceeds 6142 s total time) is the result from that experiment.

Table A2. Dynamic quantities.

Symbol	Units	Description
ω	r/min	fan rotation rate
T_F	K	ambient air temperature
T_P	K	plate temperature
T_B	K	back surface temperature
P	Pa	atmospheric pressure
Φ	Pa/Pa	air relative humidity

Table A3. Computed quantities.

Symbol	Units	Description
h_R	W/(m^{2}K)	radiative surface conductance
$U_S(u)$	W/K	side radiative and convective conductance
$\overline{h}(u,t)$	W/(m^{2}K)	convective surface conductance

Appendix A.9. Heat Balance

Collecting into $U_T(u)$ Formula (A10) those terms which have a factor of temperature difference $\overline{T_P} - \overline{T_F}$, Formula (A11) is the heat balance equation of the plate during convective cooling:

$$U_T(u) = U_S(u) + \{\overline{h}(u)\, A\} + \{\epsilon_{\mathrm{Al}}\, \epsilon_{wt}\, h_R\, A\} \tag{A10}$$

$$0 = U_T(u)\, \left[\overline{T_P} - \overline{T_F}\right] + U_I \left[\overline{T_P} - \overline{T_B}\right] + C_{pt}\, \frac{\mathrm{d}\overline{T_P}}{\mathrm{d}t} \tag{A11}$$

The plate and ambient temperatures are functions of time t. Determined experimentally during heating, the temperature group-delay through the 2.54 cm block of insulation between the slab and back sheet is 110 s:

$$\overline{T_P}(t) = \frac{U_T(u)\, \overline{T_F}(t) + U_I\, \overline{T_B}(t - 110\ \mathrm{s}) - C_{pt}\, [\mathrm{d}\overline{T_P}(t)/\mathrm{d}t]}{U_T(u) + U_I} \tag{A12}$$

To compute Nusselt number $\overline{Nu} = \overline{h}\, L/k$, Equation (A12) is solved for the $\{\overline{h}(u,t)\, A\}$ term from Equation (A10).

$$\zeta(u,t) = -U_I\, \left[\overline{T_P}(t) - \overline{T_B}(t - 110\ \mathrm{s})\right] \tag{A13}$$

$$\{\overline{h}(u,t)\, A\} = \frac{\zeta(u,t) - C_{pt}\, \left[\overline{T_P}(t) - \overline{T_P}(t')\right]/[t - t']}{\overline{T_P}(t) - \overline{T_F}(t)} - \{\epsilon_{\mathrm{Al}}\, \epsilon_{wt}\, h_R\, A\} - U_S(u) \tag{A14}$$

where t' is the previous value of t. In Equations (A13) and (A14), $\overline{T_P}(t)$, $\overline{T_F}(t)$, and $\overline{T_B}(t)$ are the 15-element cosine averages of plate and fluid temperatures (centered at time t).

Appendix A.10. Measurement Uncertainty

Following Abernethy, Benedict, and Dowdell [44], the final steps in processing an experiment's data are:

1. Using Equation (A14), calculate the sensitivities of convected power $\overline{h}\, A\, \Delta T$ per each parameter's average over the measurement time-interval;
2. Multiply the absolute value of each sensitivity by its estimated parameter bias to yield component uncertainties;
3. Calculate combined bias uncertainty as the root-sum-squared (RSS) of the component uncertainties;
4. Calculate the RSS combined measurement uncertainty as the RSS of the combined bias uncertainty and twice the product of the rotation rate sensitivity and variability.

Tables A4 and A5 list the sensitivity, bias, and uncertainty for each component contributing more than 0.20% uncertainty for the 3 mm and 1 mm roughness plates, respectively. Figure A6a and Figure A6b show the measurements relative to the present theory for rough flow and turbulent flow, respectively.

Table A4. Estimated measurement uncertainties, bi-level 3 mm roughness at $Re = 59{,}593$.

Symbol	Nominal	Sensitivity	Bias	Uncertainty	Component
ΔT	9.47 K	+12.2%/K	0.10 K	1.22%	LM35C differential
P	101 kPa	+0.0009%/Pa	1.5 kPa	1.28%	MPXH6115A6U air pressure
C_{pt}	4.69 kJ/K	+0.024%/(J/K)	47 J/K	1.14%	plate thermal capacity
η	0.401	+180%	0.014	2.52%	anemometer calibration
ς	6.00 mm	+11,299%/m	100 um	1.13%	post height
				3.50%	combined bias uncertainty
Symbol	**Nominal**	**Sensitivity**	**Variability**	**Uncertainty**	**Component**
ω	905 r/min	+0.081%/(r/min)	5.2 r/min	0.43%	fan rotation rate
				3.60%	RSS combined uncertainty

Table A5. Estimated measurement uncertainties, bi-level 1 mm roughness at $Re = 55,935$.

Symbol	Nominal	Sensitivity	Bias	Uncertainty	Component
ΔT	10.2 K	+11.8%/K	0.10 K	1.18%	LM35C differential
P	100.0 kPa	+0.0008%/Pa	1.5 kPa	1.26%	MPXH6115A6U air pressure
C_{pt}	4.24 kJ/K	+0.028%/(J/K)	42 J/K	1.18%	plate thermal capacity
η	0.340	+195%	0.003	0.66%	anemometer calibration
u_u	6.381	+2.44%	0.100	0.24%	diffuser airflow upper bound
L_T	8.34 mm	+9361%/m	100 um	0.94%	post length
L_m	3.57 mm	+473%/m	500 um	0.24%	side metal strip width
ϵ_{rs}	0.040	+21.3%	0.010	0.21%	test-surface emissivity
ϵ_{wt}	0.900	+9.46%	0.025	0.24%	wind-tunnel emissivity
				2.46%	combined bias uncertainty
Symbol	**Nominal**	**Sensitivity**	**Variability**	**Uncertainty**	**Component**
ω	1.03 kr/min	+0.065%/(r/min)	2.5 r/min	0.16%	fan rotation rate
				2.48%	RSS combined uncertainty

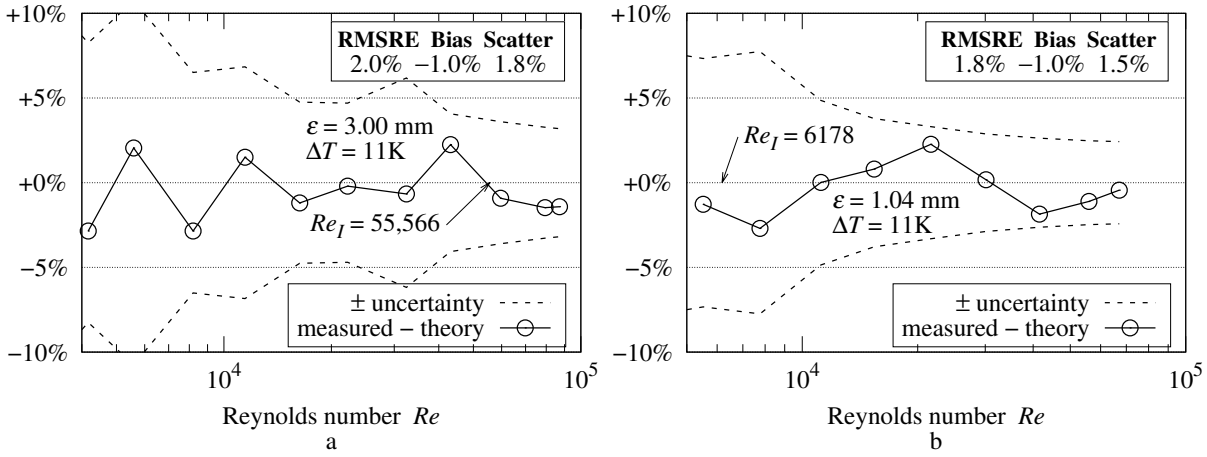

Figure A6. (**a**) Measured versus theory $\varepsilon = 3$ mm; (**b**) Measured versus theory $\varepsilon = 1$ mm.

Appendix A.11. Details

Documentation, photographs, electrical schematics, and software source-code for the apparatus, as well as calibration and measurement data, are available from [accessed on 6 December 2023]: http://people.csail.mit.edu/jaffer/convect.

Appendix B. Thermal and Transport Properties of Humid Air

Wexler [37] approximates the (partial) pressure of saturated water vapor as:

$$P_v = \exp(-0.63536311 \times 10^4/T + 0.3404926034 \times 10^2 - 0.19509874 \times 10^{-1}\, T + 0.12811805 \times 10^{-4}\, T^2) \quad \text{(A15)}$$

where T is absolute temperature in Kelvins.

An ideal gas has density $\rho = P\,M/[\overline{R}\,T]$, where the gas constant $\overline{R} = 8.314\,\mathrm{J}/(\mathrm{kg}\cdot\mathrm{mol})$. Air with relative humidity $0 < \phi < 1$, modeled as a mixture of dry air and water vapor, has density:

$$\rho = \frac{M_a\,[P - \phi\,P_v] + M_v\,\phi\,P_v}{\overline{R}\,T} \quad \text{(A16)}$$

where the molar masses of air and water are $M_a = 28.97 \times 10^{-3}$ kg/mol and $M_v = 18.0153 \times 10^{-3}$ kg/mol.

Tsilingiris [38] approximates the specific heats of dry air and water vapor:

$$\begin{aligned} c_{pa} &= +1034 - 0.2849\,T + 0.7817\times10^{-3}\,T^2 \\ &\quad - 0.4971\times10^{-6}\,T^3 + 0.1077\times10^{-9}\,T^4 \\ c_{pv} &= +1869 - 0.2578\,[T-273.15] + 1.941\times10^{-2}\,[T-273.15]^2 \\ c_p &= \frac{c_{pa}\,[1-\chi_p]\,M_a + c_{pv}\,\chi_p\,M_v}{[1-\chi_p]\,M_a + \chi_p\,M_v} \qquad \chi_p = \phi\,P_v/P \end{aligned} \tag{A17}$$

Morvay and Gvozdenac [39] approximate the viscosity of air and water vapor as:

$$\begin{aligned} \mu_a &= +0.40401\times10^{-6} + 0.074582\times10^{-6}\,T - 5.7171\times10^{-11}\,T^2 \\ &\quad + 2.9928\times10^{-14}\,T^3 - 6.2524\times10^{-18}\,T^4 \end{aligned} \tag{A18}$$

$$\mu_v = \frac{10^{-6}\,\gamma^{-1/2}}{0.0181583 + \gamma\,[0.0177624 + \gamma\,[0.0105287 - \gamma\,0.0036744]]} \tag{A19}$$

where $\gamma = 647.27/T$. They combine these into dynamic viscosity μ using absolute humidity χ, the mass ratio of water vapor to air.

$$\chi = \frac{M_v\,\phi\,P_v}{M_a\,[P - \phi\,P_v]} \qquad r_m = M_a/M_v \qquad \chi_m = \chi\,r_m$$

$$\Phi(r_m, r_\mu) = \left[1 + \frac{\sqrt{r_\mu}}{\sqrt[4]{r_m}}\right]^2 \sqrt{\frac{1}{8\,[1+r_m]}}$$

$$\mu = \frac{\mu_a}{1 + \Phi(r_m, \mu_a/\mu_v)\,\chi_m} + \frac{\mu_v}{1 + \Phi(1/r_m, \mu_v/\mu_a)/\chi_m} \tag{A20}$$

Morvay and Gvozdenac [39] approximate the thermal conductivity of water vapor at $t = T - 273.15$:

$$\begin{aligned} k_v &= +1.74822\times10^{-2} + 7.69127\times10^{-5}\,t - 3.23464\times10^{-7}\,t^2 \\ &\quad + 2.59524\times10^{-9}\,t^3 - 3.17650\times10^{-12}\,t^4 \end{aligned} \tag{A21}$$

Kadoya, Matsunaga, and Nagashima [36] approximate the thermal conductivity of dry air as:

$$\begin{aligned} k_a = 0.0259778\,(&+0.239503\,T_r + 0.00649768\,\sqrt{T_r} + 1.0 - 1.92615/T_r \\ &+ 2.00383/T_r^2 - 1.07553/T_r^3 + 0.229414/T_r^4 \\ &+ 0.402287\,\rho_r + 0.356603\,\rho_r^2 - 0.163159\,\rho_r^3 \\ &+ 0.138059\,\rho_r^4 - 0.0201725\,\rho_r^5) \end{aligned} \tag{A22}$$

where

$$\rho_r = \frac{P/314.3}{287.058\,T} \qquad T_r = \frac{T}{132.5} \tag{A23}$$

Both Morvay and Gvozdenac [39] and Tsilingiris [38] develop the combined thermal conductivity k as:

$$k = \frac{k_a}{1 + \Phi(r_m, r_\mu)\,\chi_m} + \frac{k_v}{1 + \Phi(1/r_m, 1/r_\mu)/\chi_m} \qquad r_\mu = \mu_a/\mu_v \tag{A24}$$

References

1. Prandtl, L. Zur turbulenten Stromüng in Rohren und längs Platten. *Ergebnisse Der Aerodynamische Versuchsanst Zu Göttingen* **1932**, *4*, 18–29.
2. von Kármán, T. Theorie des Reibungswiderstandes [Theory of the frictional resistance]. In Proceedings of the Hydromechanische Probleme des Schiffsantriebs, Hamburg, Germany, 18–19 May 1932; pp. 50–73. [CrossRef]
3. Prandtl, L.; Schlichting, H. *The Resistance Law for Rough Plates*; Translation; Navy Department, the David W. Taylor Model Basin: Bethesda, MD, USA, 1934.
4. Nikuradse, J. *Laws of Flow in Rough Pipes*; VDI-Verl: Berlin, Germany, 1933; p. 361.
5. Schlichting, H. *Experimental Investigation of the Problem of Surface Roughness*; Technical Report TM 823; NACA: Washington, DC, USA, 1937.
6. Hama, F.R. Boundary layer characteristics for smooth and rough surfaces. *Trans. Soc. Nav. Arch. Marine Engrs.* **1954**, *62*, 333–358.
7. Schlichting, H. *Boundary Layer Theory*, 7th ed.; Kestin, J., Translator; McGraw Hill: New Delhi, India, 2014.
8. Pimenta, M.M.; Moffat, R.J.; Kays, W.M. *The Turbulent Boundary Layer: An Experimental Study of the Transport of Momentum and Heat with the Effect of Roughness*; Department of Mechanical Engineering, Stanford University: Stanford, CA, USA, 1975.
9. Mills, A.F.; Hang, X. On the Skin Friction Coefficient for a Fully Rough Flat Plate. *J. Fluids Eng.* **1983**, *105*, 364–365. [CrossRef]
10. White, F. *Viscous Fluid Flow*, 3rd ed.; McGraw-Hill: New York, NY, USA, 2006.
11. Churchill, S.W. Theoretically based expressions in closed form for the local and mean coefficients of skin friction in fully turbulent flow along smooth and rough plates. *Int. J. Heat Fluid Flow* **1993**, *14*, 231–239. [CrossRef]
12. Colebrook, C.F. Turbulent Flow in Pipes, with Particular Reference to the Transition Region Between the Smooth and Rough Pipe Laws. *J. Inst. Civ. Eng.* **1939**, *11*, 133–156. [CrossRef]
13. Bergstrom, D.J.; Akinlade, O.G.; Tachie, M.F. Skin Friction Correlation for Smooth and Rough Wall Turbulent Boundary Layers. *J. Fluids Eng.* **2005**, *127*, 1146–1153. [CrossRef]
14. Jiménez, J. Turbulent Flows Over Rough Walls. *Annu. Rev. Fluid Mech.* **2004**, *36*, 173–196. [CrossRef]
15. Chung, D.; Hutchins, N.; Schultz, M.P.; Flack, K.A. Predicting the Drag of Rough Surfaces. *Annu. Rev. Fluid Mech.* **2021**, *53*, 439–471. [CrossRef]
16. Lienhard, J.H., IV; Lienhard, V, J.H. *A Heat Transfer Textbook*, 5th ed.; Version 5.10; Phlogiston Press: Cambridge, MA, USA, 2020.
17. Incropera, F.; DeWitt, D.; Bergman, T.; Lavine, A. *Fundamentals of Heat and Mass Transfer*; Wiley: Hoboken, NJ, USA, 2007.
18. Žukauskas, A.; Šlančiauskas, A. *Heat Transfer in Turbulent Fluid Flows*; Hemisphere Publishing Corp: Washington, DC, USA, 1987.
19. Schubauer, G.B.; Skramstad, H.K. *Laminar-Boundary-Layer Oscillations and Transition on a Flat Plate*; Technical Report NACA-TR-909; NASA: Washington, DC, USA, 1948.
20. Gebers, F. Ein Beitrag zur experimentellen Ermittlung des Wasserwiderstandes gegen bewegte Köper. *Schiffbau* **1908**, *9*, 435–452, 475–485.
21. Gebers, F. Das Ähnlichkeitsgesetz für den Flächenwiderstand in Wasser geradling fortbewegter polierter Platten. *Schiffbau* **1920**, *22*, 687–930.
22. Smith, D.W.; Walker, J.D. *Skin Friction Measurements in Incompressible Flow*; Technical Report R-26; NASA: Washington, DC, USA, 1959.
23. Spalding, D.B.; Chi, S.W. The drag of a compressible turbulent boundary layer on a smooth flat plate with and without heat transfer. *J. Fluid Mech.* **1964**, *18*, 117–143. [CrossRef]
24. Kestin, J.; Maeder, P.; Wang, H. Influence of turbulence on the transfer of heat from plates with and without a pressure gradient. *Int. J. Heat Mass Transf.* **1961**, *3*, 133–154. [CrossRef]
25. Reynolds, W.C.; Kays, W.M.; Kline, S.J. *Heat Transfer in the Turbulent Incompressible Boundary Layer, Part 4—Effect of Location of Transition and Prediction of Heat Transfer in a Known Transition Region*; Technical Report NASA-MEMO-12-4-58W; NASA: Washington, DC, USA, 1958.
26. Afzal, N.; Seena, A.; Bushra, A. Turbulent flow in a machine honed rough pipe for large Reynolds numbers: General roughness scaling laws. *J. Hydro-Environ. Res.* **2013**, *7*, 81–90. [CrossRef]
27. Flack, K.A.; Schultz, M.P.; Barros, J.M.; Kim, Y.C. Skin-friction behavior in the transitionally-rough regime. *Int. J. Heat Fluid Flow* **2016**, *61*, 21–30. [CrossRef]
28. Jaffer, A. Natural Convection Heat Transfer from an Isothermal Plate. *Thermo* **2023**, *3*, 148–175. [CrossRef]
29. Lienhard, J.H.V. Heat Transfer in Flat-Plate Boundary Layers: A Correlation for Laminar, Transitional, and Turbulent Flow. *J. Heat Transf.* **2020**, *142*, 061805. [CrossRef]
30. Colburn, A.P. A method of correlating forced convection heat-transfer data and a comparison with fluid friction. *Int. J. Heat Mass Transf.* **1964**, *7*, 1359–1384. [CrossRef]
31. Goldstein, R.; Sparrow, E.; Jones, D. Natural convection mass transfer adjacent to horizontal plates. *Int. J. Heat Mass Transf.* **1973**, *16*, 1025–1035. [CrossRef]
32. Lloyd, J.; Moran, W. Natural convection adjacent to horizontal surface of various planforms. *J. Heat Transf.* **1974**, *96*, 443–447. [CrossRef]
33. Churchill, S.W.; Usagi, R. A general expression for the correlation of rates of transfer and other phenomena. *AIChE J.* **1972**, *18*, 1121–1128. [CrossRef]
34. Tuck, E.O.; Kouzoubov, A. A laminar roughness boundary condition. *J. Fluid Mech.* **1995**, *300*, 59–70. [CrossRef]

35. Kiefer, J. Sequential Minimax Search for a Maximum. *Proc. Am. Math. Soc.* **1953**, *4*, 502–506. [CrossRef]
36. Kadoya, K.; Matsunaga, N.; Nagashima, A. Viscosity and Thermal Conductivity of Dry Air in the Gaseous Phase. *J. Phys. Chem. Ref. Data* **1985**, *14*, 947–970. [CrossRef]
37. Wexler, A. Vapor Pressure Formulation for Water in Range 0 to 100 °C. A Revision. *J. Res. Natl. Bur. Stand.* **1976**, *80A*, 775–785. [CrossRef] [PubMed]
38. Tsilingiris, P. Thermophysical and transport properties of humid air at temperature range between 0 and 100 °C. *Energy Convers. Manag.* **2008**, *49*, 1098–1110. [CrossRef]
39. Morvay, Z.K.; Gvozdenac, D.D. Toolbox 6: Thermodynamic and Transport Properties of Moist Air. In *Applied Industrial Energy and Environmental Management Part III: Fundamentals for Analysis and Calculation of Energy and Environmental Performance*; John Wiley & Sons, Ltd.: Hoboken, NJ, USA, 2016.
40. Pramuditya, S. *Water Thermodynamic Properties*; Technical report; Bandung Institute of Technology: Bandung, Indonesia, 2011.
41. Wagner, W.; Pruß, A. The IAPWS Formulation 1995 for the Thermodynamic Properties of Ordinary Water Substance for General and Scientific Use. *J. Phys. Chem. Ref. Data* **2002**, *31*, 387–535. [CrossRef]
42. Rice, R. Emittance factors for infrared thermometers used for wood products. *Wood Fiber Sci.* **2004**, *36*, 520–526.
43. Barreira, E.; Almeida, R.M.S.F.; Simões, M.L. Emissivity of Building Materials for Infrared Measurements. *Sensors* **2021**, *21*, 1961. [CrossRef]
44. Abernethy, R.; Benedict, R.; Dowdell, R. ASME Measurement Uncertainty. *ASME J. Fluids Eng.* **1985**, *107*, 161–164. [CrossRef]